Dissertation

submitted to the

Combined Faculty of Natural Sciences and Mathematics

of Heidelberg University, Germany

for the degree of

Doctor of Natural Sciences

Put forward by

Florian Sebastian Franz

born in: Munich, Germany

Oral examination: 10 November 2021

MOLECULAR DYNAMICS OF THE MEMBRANE-TALIN-VINCULIN AXIS UNDER FORCE

Referees: Prof. Dr. Ulrich Schwarz

Prof. Dr. Frauke Gräter

Zusammenfassung

Die meisten multizellulären Organismen sind auf Adhäsionsmechanismen angewiesen, um Stabilität zu gewährleisten und einen Weg für die Informationsübertragung zwischen Zellen und der extrazellulären Matrix (ECM) zu schaffen. Gewebezellen können die mechanischen Eigenschaften ihrer lokalen Umgebung wahrnehmen und darauf reagieren, was zelluläre Prozesse wie Proliferation, Migration sowie die Differenzierung von Stammzellen steuern kann. Fokale Adhäsionen (FA) sind Zusammenschlüsse mehrerer Proteine, die das mechanosensitive Bindeglied zwischen der ECM und dem Aktinzytoskelett darstellen. Zwei wichtige FA-Proteine, Talin und Vinculin, weisen im Zytoplasma eine autoinhibierte Konformation auf, doch der molekulare Prozess, der ihre Aktivierung steuert und es ihnen ermöglicht, ihr volles Signalpotenzial zu entfalten, ist noch weitgehend unbekannt.

Mithilfe umfangreicher Molekulardynamiksimulationen (MD) decken wir einen Mechanismus auf, in dem eine flexible Schleife an der Talin-FERM-Domäne als erster Kontaktpunkt mit PIP2-Lipiden in der Zellmembran dient und anschließend Membraninteraktionen fördert, die mit der autoinhibitorischen Verbindung zur Talin-Stabdomäne konkurrieren können. Wir zeigen, dass eine Vielzahl von Vinculin-Bindungsstellen (VBS) in der Talin-Stabdomäne in einer stark kraftregulierten Weise an Vinculin binden. Auf atomistischer Ebene beschreiben wir einen Mechanismus, bei dem die VBS-Bindung mit der autoinhibitorischen Verbindung zum Vinculin-Schwanz konkurriert, was von einem Experimentator mit der magnetischen Pinzette bestätigt wurde. Schließlich halfen MD-Kraftsonden-Simulationen bei der Identifizierung derer Aminosäuren, die an der VBS-induzierten Schwächung der Vinculin-Kopf-Schwanz-Grenzfläche beteiligt sind und so die Aktivierung des Proteins erleichtern. Auf dieser Grundlage schlagen wir zwei neue Vinculin-Mutanten vor, die den Effekt der Talin-Assoziation nachahmen und in Experimenten von Kollaborationpartnern signifikant erhöhte Interaktionen mit Aktin zeigen - vergleichbar mit VBS-aktiviertem Wildtyp-Vinculin.

Zusammengefasst bieten unsere Ergebnisse neue Einblicke in die molekularen Grundlagen der Talin- und Vinculin-Aktivierung, die dazu beitragen, unser Verständnis der hierarchischen FA-Reifung und Mechanotransduktion zu verbessern.

Abstract

Most multi-cellular organisms depend on adhesion mechanisms to provide stability and a pathway for the transduction of information between cells and the extra cellular matrix. Tissue cells can sense and react to the mechanical properties of their local environment which can steer cellular proliferation, migration, as well as differentiation in stem cells. Focal Adhesions are multi-protein assemblies that constitute the mechanosensitive link between ECM and the actin cytoskeleton. Two major FA proteins, talin and vinculin, exhibit an auto-inhibited conformation in the cytoplasm, yet the molecular process that regulates their activation and allows them to unfold their full signalling potential remains widely unknown.

Using extensive molecular dynamics (MD) simulations we reveal a mechanism by which a flexible loop on the talin FERM domain serves as a first contact point with PIP2 lipids in the cellular membrane and subsequently promotes membrane interactions that can compete with the autoinhibitory link to the talin rod domain. We demonstrate that a variety of vinculin binding sites in the talin rod bind to vinculin in a highly force-regulated manner. We describe on an atomistic level a mechanism in which VBS-binding competes with the autoinhibitory link to the vinculin tail, which was corroborated by a collaborator in magnetic tweezers experiments. Lastly, force-probe MD simulations helped to identify the residues involved in the VBS-induced weakening of the vinculin head-tail interface, facilitating protein activation. With this, we propose two novel vinculin mutants that mimic the effect of talin association and show significantly increased interactions with actin – comparable to VBS-activated wild-type vinculin – in experiments carried out by collaboration partners.

Summarized, our findings provide novel insights into the molecular underlying of talin and vinculin activation which help to improve our understanding of hierarchical FA maturation and mechanotransduction.

Acknowledgement

There are many people who deserve thanks for their assistance and support over the last four years. I can't name everyone, but there are a few people in particular who I'd like to mention. First and foremost, I'd like to express my gratitude to the HGS Math Comp and the Klaus Tschira Foundation for funding this study. My sincere gratitude goes to Prof. Frauke Gräter, my supervisor. Her advice, suggestions, reviews, and encouragement have all been immensely valuable for the progress of this PhD. I'd also like to thank Prof. Ulrich Schwarz for his role as first supervisor and referee.

Past and present members of the MBM Group deserve special recognition for their suggestions and contributions. Particularly, Nicolas Michelarakis for all the Greek delicacies and guidance that can only be provided by a *wise post-doc*. Special thanks go to Jannik Buhr, a former master and now PhD student, we collaborated on a couple of projects and encouraged each other to become better programmers and scientists. I would also like to thank Camilo Aponte-Santamaría for his valuable insights and suggestions.

Further, I would like to thank the Heidelberg Institute for Theoretical Studies as a whole. The exceptional environment created by the fellow scientists, administration, as well as kitchen staff spurs creativity and have made for a pleasant journey throughout this PhD. Further, I would like to express my deepest gratitude to Prof. Benny Geiger and Prof. Michal Sharon for the opportunity to learn experimental methods at the Weizmann Institute of Science and the unforgettable experience that were the six months in Rehovot, Israel.

On a more personal note, I want to thank my family and friends outside of the lab. Their support has started long before this PhD and have helped to shape me as a scientist and person.

Contents

List of Figures

List of Tables

1

Introduction

With the transition from unicellular life to multicellular organisms with a defined body plan over 750 million years ago, cells developed different mechanisms of adhesion. These mechanisms are essential for all multicellular animals, from sponges to humans, as they enable cells to organize into a single organism by adhering to each other or to a scaffolding structure such as the extracellular matrix (ECM). [1, 2] Along with the capabilities of adhesion, cells also developed means to propel themselves. Certain cells can leverage their adhesive structures to generate the motility necessary in processes like embryogenesis, wound healing, and immune function. [3] Not only do adhesive interactions enable the organization of cells into functional tissues, but they also provide the cell with precise information about their local environment. This information can then have an impact on all aspects of the life of a cell, including its differentiation, proliferation, and fate. [4]

1.1. Mechanotransduction

While cells gather chemical and physical information alike, the emphasis of this work lies on the mechanical information the ECM has to offer. ECM composition and structure are precisely tuned according to the surrounding tissue in order to support the functions of cells and organs. [3] The cells in the body can sense, decode and respond to mechanical signals that depend on the physical and mechanical properties of the underlying tissue and the ECM, such as density, topography, and, most importantly, stiffness. [5] Tissue stiffness varies dramatically throughout the human body. Cortical bone, the most rigid structure in the body, reaches a Young's modulus of ~20 GPa, while brain tissue, our softest organ, has an elastic modulus of only ~2 kPa. [6, 7] With a Young's modulus of ~1 MPa, cartilage lies roughly in the middle of the seven orders of magnitude of rigidity the human body encompasses. While stiffness-sensing requires cells to exert forces to measure the response of a given material, the cell also experiences transient forces of external origin, for example from muscle contraction or blood circulation. The reactions to these forces depends on so-called 'cellular mechanosensors' and, until now, a variety of molecules have been identified, mostly proteins that alter their state in response to mechanical cues. [5] These mechanical stimuli can have a wide range of effects, both in terms of nature and magnitude of the caused change. Processes such as protein unfolding, [8] post-translation modifications, [9, 10], intracellular shuttling, [11] and the formation of novel interactions [12] are common mechanosensitive responses of 'cellular mechanosensors'. During the transfer of mechanical information from the ECM to the nucleus, these responses often interplay and are collectively referred to as mechanotransduction. [5]

The cellular membrane makes direct contact with the ECM and, consequently, mechanotransduction pathways usually start with membrane proteins such as tension-activated ion channels, G protein-coupled receptors, growth factor receptors, or integrins. [13, 14] In this thesis, we place the major emphasis on integrin-based cell-matrix adhesions, which form the connection between the ECM, integrins, the cytoskeleton, and the nucleus. [1]

1.2. Cell-matrix adhesion

Composition of integrin-based cell-matrix adhesions

The term 'integrin adhesome' was defined by Zaidel-Bar et al. [15] as the group of proteins and genes that are involved in integrin-mediated adhesion. The authors initially identified 156 proteins and 690 interactions compiling experimental data and, by now, their database (adhesome.org) contains over 220 proteins and over 6000 interactions. Later

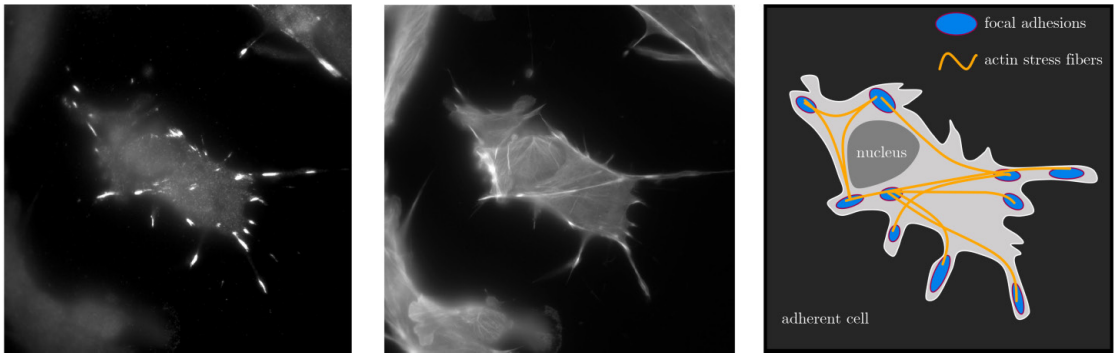

Figure 1.1.: Adherent cells. A mouse embryonic fibroblast cell was stained for vinculin (left) as focal adhesion marker and for actin (centre). On the right, a schematic representation of the cell is shown. The microscopy images (left and centre) were provided by the Geiger lab (Weizmann Institute of Science, Israel).

on, Horton et al. [16] combined seven mass-spectrometry data sets with the composition of the adhesome for a variety of cell types in different culture conditions. The resulting 'meta-adhesome' database with over 2000 components reflects the complexity of integrin adhesion structures. Correlating the data sets, the authors defined a 'consensus adhesome' with the 60 most commonly identified proteins. The resulting integrin-adhesion network between the 60 consensus components was visualized compellingly by Horton et al. [17].

Force-dependent maturation of cell-matrix adhesions

Regular tissue cells are dependent on an anchorage to a stiff surface in order to function properly and survive. [18] Where contact to a stiff surface is given, cells develop distinct multi-protein complexes beneath the membrane which link the cell to the matrix. The development of these cell-matrix adhesions is hierarchical and commences with small dot-shaped nascent adhesions which form at the protruding edge of adherent cells (see figure 1.1). [19] Only a few hundred protein molecules compose the ~100 nm wide nascent adhesions. [20, 21] The protruding edge of motile cells is characterized by the lamellae whose principal structures are actin networks that contain myosin-II. From the lamellae, cells exhibit finger-like protrusion called filopodia and sheet-like membrane protrusions called lamellipodia (see figure 1.1). Within the lamellipodia, the 'actin retrograde flow', that is polymerizing actin which flows centripetally towards the centre of the cell, brushes against the nascent adhesions. This mechanical stimulus promotes the growth of emerging adhesions; particularly, the accumulation of vinculin that binds to talin has been linked to an increase in clustering of activated integrins. [22] In turn, the vinculin tail binds to actin which strengthens the interface of the focal adhesion to the actin network. [23–26]

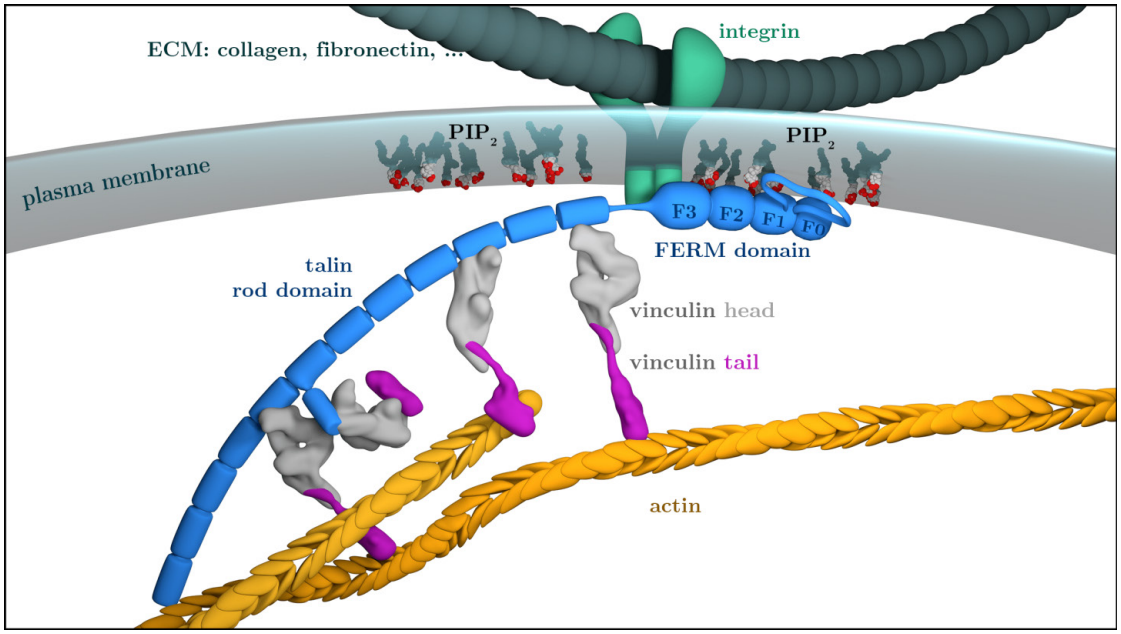

Figure 1.2.: The focal adhesion. Schematic illustrating the organization of integrin receptors, talin, vinculin, the actin network, and the increased PIP_2 concentration.

The maturation of the nascent adhesion into larger focal adhesions (FA) depends on myosin-II-generated forces that contract the actin cytoskeleton and further tense and grow the adhesion site.

Inhibition of myosin-II, for example with blebbistatin, causes the detachment of vinculin and disassembly of the FAs, while nascent adhesions remain intact. [27] Consequently, focal adhesions are force-dependent constructs that are located at the interface between intracellular tension originating from the actin-myosin machinery and extracellular forces (see figure 1.1). This clever positioning primes them for the transmission of mechanical cues from the outside to the inside of the cell and vice versa.

Focal adhesion structure

FAs constitute the main signalling hub for ECM-cell mechanotransduction. Their structure can be separated into two layers: a transmembrane and an intracellular layer. The transmembrane layer consists of proteins called integrins which connect the ECM to the intracellular layer. The family of integrins offers a large variety of α and β chains which, paired up, form the integrin receptors as heterodimers. The receptors bind ECM components like collagen, laminin, fibronectin, vitronectin, and fibrin with a specificity regulated by the respective subunits (α and β chains). [3] The intracellular

layer accommodates a multitude of docking, scaffolding, and signalling proteins. The composition of the former not only depends on the cell type and culture condition, but also exhibits an intricate layered nanostructure, as revealed by super-resolution microscopy images of the ~200 nm-thick intracellular segment of FAs. [28] Three general layered domains of the intracellular FA have been identified. Within 10-20 nm from the plasma membrane, the integrin cytoplasmic tails and focal adhesion kinase and paxilin dominate. At a higher vertical distances of 50-60 nm, α-actinin, vasodilator-stimulated phosphoprotein, and zyxsin dominate alongside the actin filaments. In between, a 'force-transduction layer' was identified with high concentrations of vinculin and of the talin rod domain. Furthermore, the authors found talin to be oriented in a highly polarized manner with at least 30 nm of vertical distance between the the N- and C-termini. With a total size of 60 nm, talin diagonally bridges the 'force-transduction layer' and extends to the integrin-proximity layer with its FERM domain, and to the 'actin-proximity layer' with its rod domain. Vinculin localization was found to be dependent on the proteins activation state; inactive vinculin concentrates closer to the membrane and paxilin, while activated vinculin targets higher FA layers and binds to talin and actin. [29] While the functional implications of this layered architecture remain elusive, this thesis aims to better understand the dynamics of the interaction between talin, vinculin, and the cellular membrane.

Adhesion dynamics

As elaborated above, various mechanisms govern the molecular composition of cellular adhesions. The cell type, state of development, as well as the location within the adhesion all influence the protein fingerprint. Furthermore, the molecular composition of FAs is highly dynamic in time as physio-chemical properties of the extracellular environment change during, for example, cell migration. The morphology of some cell types, such as fibroblasts, is greatly influenced by the stiffness of the substrate. [3, 30] Figure 1.1 shows microscopy images of an adherent fibroblast cell. The reactions to the mechanical cues by FA proteins govern the turnover of FA components and, in turn, the modified adhesion dynamics convey signals that modify the structure of the cytoskeleton and the shape of the cell. [31]

Studies applying Fluorescence Recovery After Photobleaching (FRAP) found that turnover rates vary for different types of FA proteins and, moreover, the dependency on substrate stiffness is more pronounced in some types of proteins than in others. [31] Focal adhesion kinase and paxillin, for example, were found to be very dynamic with high turnover rates which is mostly unaffected by the stiffness of the substrate. Contrastingly, talin and vinculin turnover rates are generally lower and strongly correlated to the physical

properties of the ECM. The authors attribute the lower turnover rates to their structural relevance as both proteins bind directly to actin. The stiffness dependency of their mobility indicates that talin and vinculin primarily fulfil mechanosensitive roles within the FAs. [32]

The role of the membrane in cellular adhesion

The cellular membrane is more than a simple boundary that separates the interior of the cell from the rest of the organism; it is also a compartment that houses several vital cellular functions, such as molecular transport, metabolic operations, and the receptors responsible for communication with the outside world. Membranes consist of carbohydrates, proteins, and, most importantly, lipids. Lipid molecules are amphipathic, which means they are characterized by a hydrophobic tail and hydrophilic head. When diluted in water, they adopt a conformation that maximizes thermodynamically favourable interactions, which under biological conditions, is some shape of a lipid bilayer. [33] The local membrane composition of the over 600 known distinct lipid molecules (in humans alone) is variable and of functional importance. [34] Particularly important, in the context of focal adhesions, is Phosphatidylinositol-4,5-bisphosphate (PIP_2) which as been shown to bind to many actin-binding scaffolding proteins as well as to signalling proteins. [35] The PIP_2 molecules, which bear a double negative charge, are only found within the interior leaflet of the cell membrane. In close proximity to focal adhesions, the local abundance of PIP_2 within the inner membrane leaflet is with 10% significantly higher than the cellular average of 1%, as is illustrated in figure 1.2. This is caused by the GTP-binding protein Rho that elevates the activity of phosphatidylinositol-4-phosphate-5-OH kinase. [36] The local increase in PIP_2 was found to promote actin polymerization. [37] In the case of the scaffolding protein talin, the PIP_2 concentration has been demonstrated to influence the affinity of integrin binding. [38] In chapter 3, we identify a possible path for PIP_2-mitigated talin activation and show that the increased concentration of charged lipids localizes talin to the FA site by increasing the lateral friction between protein and membrane.

Figure 1.2 depicts a highly simplified model of FA, which features the major scaffolding protein talin as the direct link between integrins and actin fibres and vinculin attached to talin as it reinforces the connection to the cytoskeleton. With an *in vivo* density of 1000 integrins per μm^2 at growing focal adhesions, FAs reaching up to 10 µm in length [39], and many other signalling protein involved, the true complexity of focal adhesions exceeds the illustrated one vastly. As the focus of this thesis resides on the force-dependent reaction of talin and vinculin and the talin-membrane interaction, the figure is restricted to the FA components most relevant to their understanding.

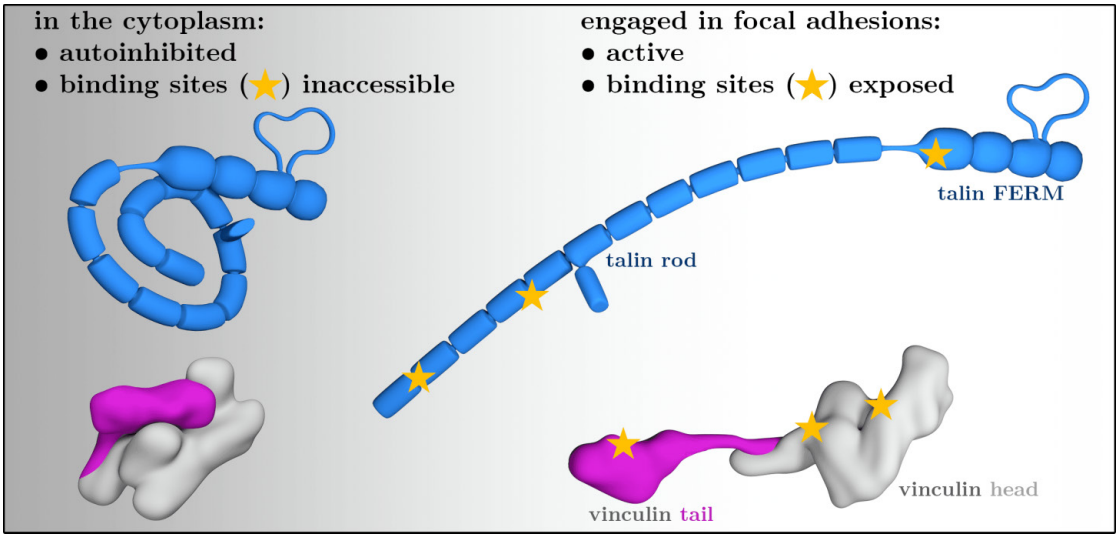

Figure 1.3.: Activation of talin and vinculin. The schematic illustrates the conformational changes caused by the activation of talin and vinculin. The latter is a precursor to all further signalling mediated by the two proteins.

1.3. Mechanosensitive pathways in talin and vinculin

The mechanosensitivity of talin and vinculin has a two-folded characteristic. First, the autoinhibited conformation the proteins take up when freely diffusing in the the cytoplasm must be relieved – a process that requires cellular forces. Second, tensile forces across the proteins [40, 41] expose further binding sites and start signalling cascades. [12] The relieve of the autoinhibition of talin is closely linked to and dependent on the increased PIP_2 concentration in the membrane close to focal adhesions. [42] For vinculin to activate, it needs to bind talin and the respective binding sites only become available if talin is under tensile stress. [43–47] Figure 1.3 illustrates the conformational changes these proteins have to undergo to partake in mechanotransductive pathways. The introductions to chapter 3 and chapter 5 provide a more in-depth review of the intricate details of the two proteins.

1.4. ECM-rigidity dependent cellular processes

Cell migration

When nascent adhesions mature, the resulting FAs are able to withstand large amounts of force. Motile cells, such as fibroblasts or epithelial cells use these stable anchors to propel themselves forward. [48] Hereby, the polymerizing actin (Rac1 GTPase activity-regulated) pushes against the membrane protruding one edge of the cell forward. A lamellae forms in

which more nascent adhesions develop [19, 49]. As described above, the nascent adhesions develop into force bearing FAs. Myosin-generated tension acts on actin stress fibers which contracts the cell. Through the disassembly of FA at the rear end of the cell, the latter is retracted and the cell moves forward. The direction of this motion is influenced to a great extent by the properties of the ECM. One notable example is 'durotaxis', which describes the ability of cells to sense a gradient in ECM rigidity and preferentially migrate towards areas of higher stiffness. [50] For this, individual FAs seem to exert forces that are highly variable in time. These so-called 'tugging' forces are pivotal for the mechanosensitivity of the process. Interestingly, 'durotaxis' relies on a pathway which strongly depends on vinculin which further underlines the mechanosensitive capabilities of the protein. [51]

Stem-cell differentiation

The broad role of mechanotransduction in biology expands to early development. [52] Substrate stiffness has been demonstrated to direct stem-cell differentiation. In their pivotal study Engler et al. [53] discovered that soft substrates steer mesenchymal stem cells towards neurogenesis. In contrast, stiffer substrates prime stem cells for a development into osteoids and myoblasts. The observed dependence on substrate stiffness was relieved if myosin-II was inhibited with blebbistatin which suggests that the force-sensing mechanism responsible for differentiation is FA-mediated and similar to the above-described one involved in durotaxis. Accordingly, vinculin knock-out stem cells display impaired differentiation and durotaxis. [54]

These examples demonstrate the crucial role of FA-mediated mechanotransduction in many essential cellular processes. Nonetheless, how the force-response of FA proteins governs their interplay on a molecular level remains widely elusive.

1.5. Aims

The overall aim of this thesis is to shed light onto the interaction and activation of talin and vinculin, arguably two of the most prominent mechanosensing FA proteins. Thereby, the focus resides on the force-dependence of the interaction between the proteins, as well as the involvement of the cellular membrane in the activation process. To this end, we employ force-probe molecular dynamics simulations, a method that provides the means to better understand the tension-influenced interplay of the proteins on a molecular level. The presented findings are corroborated by single-molecule magnetic tweezers experiments and total internal reflection fluorescence microscopy (TIRFM) carried out by collaborators at King's College London and at the University of Zürich, respectively.

Membrane-dependent talin activation

The topic of chapter 3 evolves around the function of the FERM domain of talin. The protein adapts an autoinhibited conformation in the cytoplasm [55] which masks the major PIP_2 binding sites. [56, 57]. Nonetheless, PIP_2-containing membranes seem sufficient to achieve an activation of the protein. [42] Using MD simulations we aim to uncover the molecular mechanism by which PIP_2 can bind and activate talin as well as the possibility that the charged lipid helps localizing talin to the focal adhesion site.

Dynamics of the talin-vinculin interaction

The talin rod contains eleven known binding sites for vinculin (VBS). [58] The talin VBS are only exposed if the protein is under force [43, 59] and the molecular mechanism by which the VBS bind to vinculin remains elusive. Combining our MD simulations with magnetic tweezers experiments by Dr. Rafael Tapia-Rojo of King's College London, we aim to further the understanding of this process in chapter 4. Additionally, we seek to elucidate how the stability of the VBS-vinculin interaction is fine-tuned across the different VBS to provide a highly force-sensitive machinery.

Talin-dependent vinculin activation

Once talin is bound to vinculin, allosteric effects alter the head-tail interface of the auto-inhibited vinculin. [44–47] In the last research chapter, we aim to quantify the repercussions of this alteration on the activation process of vinculin using force-probe MD simulation. We further aim to design novel vinculin mutants that mimic the effect of talin binding and probe their interaction with branched actin networks in TIRFM experiments carried out by the Medalia lab at the University of Zürich.

Overall, the mechanistic and atomic-level insights into the interactions across the membrane-talin-vinculin axis shall advance our understanding of cellular mechanosensing.

2

Methods

This chapter explains the simulation and analysis methods that were used throughout the projects presented in chapters 3-5. Subsequent to an inaugural overview of the most important aspects of molecular dynamics (MD) simulations, the chapter proceeds with a brief review of how MD simulations and experiments are increasingly working together to solve biological mysteries. It concludes with an exposition of the statistical methods that were used to evaluate and interpret the findings throughout this thesis.

2.1. Molecular dynamics simulations

As the name implies, molecular dynamics simulations are a technique that aims to describe the time-dependent dynamics of molecules. More specifically, it propagates a system containing one or more molecules, each of which can contain one or more atoms, through time. To that end, atoms are described as points that communicate with one another through spring-like potentials, creating a traditional N-body problem. The atomic coordinates in three-dimensional space and their instantaneous velocities define the state

of the molecular system. To advance the system in time from one state to the next, Newton's equation of motion is integrated numerically – which today usually happens on high performance computing infrastructures.

For historical context, we briefly mention the IBM 704 computer of 1957, which was used for the very first MD simulation of perfectly elastic collisions between hard spheres. [60] In 1964, Rahman presented simulations of liquid argon using a Lennard-Jones potential constituting perhaps the first accurate physical simulation of matter. Estimates of system properties, such as the coefficient of self-diffusion, matched experimental results well. [61] Over the years, continuous advancements in computing capacity, force field development, and methodology, have made MD simulations an effective and indispensable tool for studying all kinds of biological systems, including proteins, lipid membranes, nucleic acids, and sugars. Section 2.2, later in this chapter, provides a brief review of how MD simulations and experiments are used today to research the force response of proteins.

2.1.1. Interaction potentials

MD simulations aim to provide trajectories of individual atoms as a function of time. Due to this atomic-level resolution, they can often be used to define the system-wide properties of a molecular model much more effectively than real-world experiments. In order to do so efficiently and with high precision, a framework is needed to describe the energy of the system as a function of its atomic positions. This framework is termed 'force field' and represents a set of empirically determined functions and their parameters that assigns a potential energy function $V(r_1, r_2, ..., r_N)$ to the atomic coordinates $r_1, r_2, ..., r_N$ of a simulated system of N atoms. Typically, force fields differentiate between bonded and non-bonded interactions. Bonded potentials, as indicated by the nomenclature, define interactions between covalently bonded atoms. These intra-molecular potentials between chemically bound atoms are approximated by a range of 2 (bonds), 3 (angles), and 4-body (dihedral angles and improper dihedral angles) interactions. Non-bonded terms describe intra- and inter-molecular interaction energies arising from electrostatics and the Van der Waals force. The AMBER [62] and CHARMM [63] force fields, which were used in this work, use the following functional terms to calculate the interaction energies.

The two-body potential that emerges form the covalent bonds between any two bonded atoms i and j is denoted by V_{distance}, where

$$V_{\text{distance}} = \sum_{ij}^{\text{bonds}} \frac{1}{2} k_{ij}^{r} \left(r_{ij} - r_{ij}^{0}\right)^2, \tag{2.1}$$

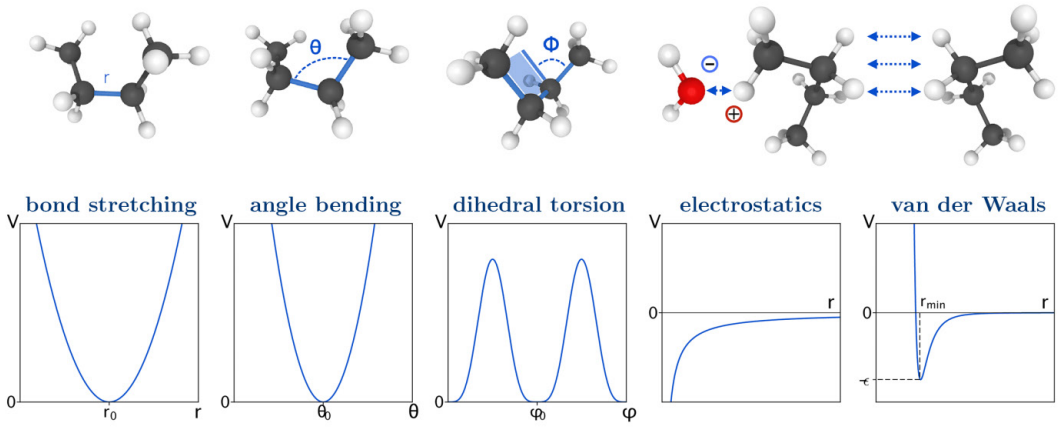

Figure 2.1.: Potential types in force fields. A graphical representation of the total potential's constituents. The energy contributions from bonded interactions; bond stretching, angle bending, and dihedral torsion, as well as non-bonded interactions; electrostatics, and van der Waals interactions, are combined in a classical forcefield. Figure adapted from ref. [64]

with $r_{ij} = |\mathbf{r}_j - \mathbf{r}_i|$ being the distance between atoms i and j, r_{ij}^0 the equilibrium bond-length, and k_{ij}^r elastic constant.

V_{angle} denotes the sum of interaction energies resulting form the deformation of angles θ_{ijk} encompassed by the atoms i, j, and k,

$$V_{\text{angle}} = \sum_{ijk}^{\text{angles}} \frac{1}{2} k_{ijk}^{\theta} \left(\theta_{ijk} - \theta_{ijk}^0\right)^2, \tag{2.2}$$

where k_{ijk}^{θ} and θ_{ijk}^0 are the harmonic force constant and and equilibrium angle, respectively.

$$V_{\text{dihedral}} = \sum_{ijkl}^{\text{dihedrals}} \frac{1}{2} k_{ijkl}^{\phi} \left(1 + \cos\left(n\phi_{ijkl} - \phi_{ijkl}^0\right)\right) \tag{2.3}$$

is the potential energy originating from deviation from the equilibrium dihedral angles ϕ_{ijkl}^0. The dihedral angle ϕ_{ijkl} is the angle between the two planes defined by the atoms i, j, k, and j, k, l, and the multiplicity of the dihedral n. This potential effectively represents the torsion of a four-atom group, or, for a more descriptive explanation, out-of-plane angle bending. Aromatic rings are a good example for the importance of dihedral potentials: Two- and three-body potentials alone are insufficient to hold these ring-shaped molecules in planar conformations.

Non-bonded interactions are represented by a Lennard-Jones term V_{LJ} and an electrostatic term V_{Coulomb}. Short-range Pauli repulsion (power 12 term) and long-range van der Waals attraction (power 6 term) are combined in the Lennard-Jones potential:

$$V_{\mathrm{LJ}} = \sum_{ij} 4\epsilon_{ij} \left[\left(\frac{\sigma_{ij}}{r_{ij}} \right)^{12} - \left(\frac{\sigma_{ij}}{r_{ij}} \right)^{6} \right], \tag{2.4}$$

where ϵ_{ij} and σ_{ij} characterize the depth and the width of the respective potential. Finally, the electric potential V_{Coulomb} between a pair of atoms with charges q_i and q_j, which are for example ions or partial charges along larger molecules, must be taken into consideration:

$$V_{\mathrm{Coulomb}} = \sum_{ij} \frac{1}{4\pi\epsilon_0\epsilon} \frac{q_i q_j}{r_{ij}^2}, \tag{2.5}$$

with ϵ_0 denoting the dielectrical constant and ϵ the relative dielectric constant.

The individual contributions of potential energies simply add up, as shown by the summations in the above formulas. Consequently, the total energy of the system emerges as:

$$V = V_{\mathrm{distance}} + V_{\mathrm{angle}} + V_{\mathrm{dihedral}} + V_{\mathrm{LJ}} + V_{\mathrm{Coulomb}}. \tag{2.6}$$

Partial differentiation of the potential with respect to the atomic coordinates allows us to compute the force acting on each atom. As differentiation is a linear operation, forces are calculated from the analytic derivatives of the above listed potential energy functions. The total force acting on one atom emerges as the sum of all individual forces acting on that atom, analogously to equation (2.6).

$$\mathbf{F}_i\left(\mathbf{r}_i\right) = -\frac{\partial V_{\mathrm{distance}}}{\partial \mathbf{r}_i} + \ldots. \tag{2.7}$$

Once all the forces acting on the atoms in their local potentials are calculated, Newton's equation of motion is numerically integrated over a finite time-step to obtain the atomic coordinates for the next state.

2.1.2. Integration

Newton's equation of motion can be written as a second-order differential equation for an N-body system:

$$\mathbf{F}_i = m_i \frac{\mathrm{d}^2 \mathbf{r}_i}{\mathrm{d}t^2}. \tag{2.8}$$

As ordinary linear differential equations can be reduced to a system of first order equations, we can write:

$$\frac{\mathrm{d}\mathbf{r}_i}{\mathrm{d}t} = \mathbf{v}_i \tag{2.9}$$

$$m_i \cdot \frac{\mathrm{d}\mathbf{v}_i}{\mathrm{d}t} = \mathbf{F}_i, \tag{2.10}$$

where $i = 1, \ldots, N$ is the particle index, and $\mathbf{v}_i$ and $\mathbf{r}_i$ are the velocity and position of the atom, respectively. Through numerically solving the $6N$ first order differential equations, the positions and velocities of the atoms in the simulated system are updated. A symplectic numerical integrator guarantees energy conservation, since it conserves the phase space volume while advancing in time. A commonly used symplectic integration scheme is the 'leap-frog' algorithm, which is algebraically equivalent to the 'Verlet' algorithm. [65] They are based on the velocity and location Taylor series:

$$\mathbf{r}_i\left(t + \Delta t\right) = \mathbf{r}_i\left(t\right) + v_i\left(t + \frac{\Delta t}{2}\right)\Delta t \tag{2.11}$$

$$\mathbf{v}_i\left(t + \frac{\Delta t}{2}\right) = \mathbf{v}_i\left(t - \frac{\Delta t}{2}\right) + \frac{F\left(t\right)}{m}\Delta t. \tag{2.12}$$

Integration propagates the system to the next state, where the updated positions are used to calculate the new forces as defined previously (Equation (2.8)). Every few thousand steps of integration, the positions and velocities are written out in a trajectory file which can be later used for analysis.

The time increment Δt defines how fast and/or precisely the simulation runs. For an accurate representation of the high-frequency vibrations of covalent bonds involving light hydrogen atoms, a very short integration time step would be required. However, these vibrations only have a negligible influence on the macromolecular evolution on longer time scales. Hence, constraining bond lengths or bond angles – especially between heavy atoms and hydrogen atoms – eliminates the highest frequency vibrations and is a commonly used technique for speeding up MD simulations. In practice, this is realized with algorithms like LINCS [66] or SHAKE [67] permitting integration time steps of $\Delta t \geq 2$ fs.

In a system that only interacts through non-bonded interactions, e.g. a system containing N monoatomic gas molecules, the computation of all interactions results in $N(N-1)/2$ terms. One example of a typical biomolecular simulation system is a single protein in water. Here, most of the atoms form chemical bonds. While this reduces the number of non-bonded interactions, the number of terms still scales with N^2. This would imply a parabolic increase in computational cost as the system size increases only linearly, which is, of course, highly unfavourable. Nonetheless, modern MD algorithms manage to scale with $N \cdot \log N$. To understand how such a performance increase is achieved, we need to first understand a few computational tricks that are commonly used to treat the short and long range interaction in state-of-the-art MD software.

Both non-bonded potentials decrease with $1/r^x$ with $x = 2$ for the Coulomb potential and $x = 6$ for the Lennard-Jones potential. The resulting forces become very small as the distance increases, which makes the use of approximations for the long-range part of these potentials computationally rewarding as the entailed errors remain small. In the case of the quickly decaying Lennard-Jones potential, this is leveraged by setting forces beyond a cut-off distance of 1.0 - 1.2 nm to zero.

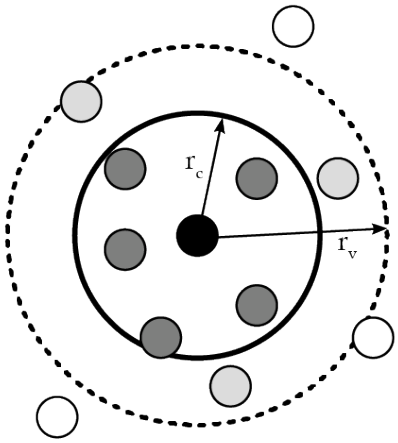

Figure 2.2: Verlet neighbor list. Forces from non-bonded interactions are only calculated for atoms within the cut-off distance r_c (dark gray) form the particle in consideration (black). The Verlet list also includes atoms (light gray) that do not contribute to the potential but were within the Verlet skin with radius r_v at the time the neighbor list was last updated. In subsequent time steps, distance calculations are only executed for particles in the neighbor list. This reduces the number of computations drastically for time steps in which the Verlet list is not updated. Figure adapted from ref. [64]

Even though the use of a cut-off distance for short range interactions is a very effective method to cut down computational cost, it still requires the calculations of all the distances between all atoms to figure out which ones fall within the cut-off and which ones do not. Verlet lists [65] are a broadly used method to greatly reduce the number of distance calculations. Here, a second cut-off distance r_v is introduced, with is slightly larger than the previous cut-off distance r_c. r_v is called the Verlet skin and all atoms within a radial distance of r_v from the particle in consideration are stored in the so called Verlet list. In

each time step, only the respective Verlet lists are checked for potential force calculations with $r < r_c$. The Verlet lists themselves are updated less frequently. A commonly used criteria to trigger an update is the displacement of a particle larger than $|r_v - r_c|$.

Cut-off based approaches are a good solution for the Lennard Jones potential, which decreases rapidly with distance. The electrostatic potential, on the other hand, decreases much more slowly, implying that long-range interactions are overlooked and result in simulation artifacts. To account for the contribution of long-range electrostatics to the total potential energy in a computationally feasible manner, a method based on Ewald summation has been implemented. Particle Mesh Ewald (PME) is an improved version of this approach that evaluates the charge density on a discrete mesh. Each grid point is given a charge based on the atoms in its immediate vicinity. The lattice points interact with each other via a Coulomb potential and the resulting forces are redistributed to the atoms in proximity of the respective grid point. The main benefit of the PME approach is that forces are computed for the entire system in one go, rather than in a pair-wise fashion. It is worth noting that this approach presupposes infinite periodicity of the system in question. The following section explains how periodic boundary conditions are used in simulations to satisfy this requirement.

2.1.4. Periodic boundary conditions

The most common application of MD simulations is the study of a protein in water, where the focus is set on the dynamics of the protein rather than the movement of the water molecules. This inevitably raises the question of how the boundaries of the simulated box are handled. In an open system, particles are free to move around and there is no way to maintain a constant atom density. If closed boundaries are used, the interaction of water molecules with the boundary may cause simulation artifacts if there is not a substantial amount of water between the protein and the boundary. To solve these problems, MD simulations often use periodic boundary conditions (PBC). A periodic boundary management effectively generates an infinite system by continuing the simulation box in every spatial direction with translated images of itself. If a particle leaves the unit box on one side, one of its images will emerge on the opposite side maintaining the the same velocity vector. As a consequence, it suffices to only track the coordinates of atoms within the unit box.

Atoms close to a boundary will inevitably interact with image atoms on the other side of the boundary, that is, with atoms on the opposite side of the unit box. For this, the unit cell cannot be arbitrarily small; interaction of a molecule with its own periodic image

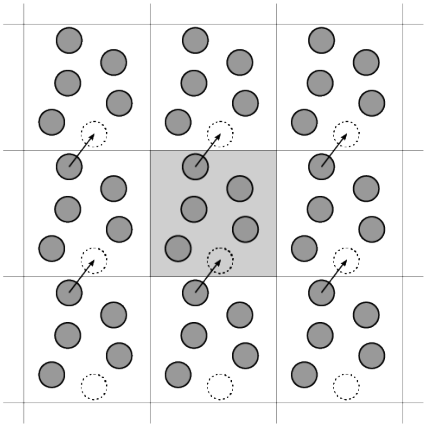

Figure 2.3: Periodic boundary conditions. This illustration aims to explain the principle behind periodic boundary conditions. In this two dimensional example, we see how the simulated system (shaded box) is expanded with images of itself in every direction. When an atom crosses a system boundary on one side, it simultaneously reenters the system on the opposite side. The dotted circles represents the particles after they have crossed the boundary, as shown by the arrow. Figure adapted from ref. [64]

can cause unwanted artifacts. To avoid this, the molecule of interest should be separated from its periodic images by a sufficiently thick layer of solvent. This must be taken into account when specifying box sizes.

It is important to note that PBC needs a space-filling simulation box geometry in order for the replicated boxes to form a space-filling lattice.

2.1.5. Pressure and temperature control

The integration of Newton's equations of motion in the context of periodic boundaries yields a microcanonical ensemble, that is, particle number, volume, and energy of the system are preserved. Since real world experiments oftentimes control for pressure and/or temperature, a method to regulate these quantities in simulations is needed.

The equipartition theorem shows how the temperature T relates to the velocities v_i in a molecular system of N atoms,

$$\frac{3}{2}Nk_BT = E_{\text{kin}} = \left\langle \sum_{i=1}^{N} \frac{1}{2} m_i v_i^2 \right\rangle \tag{2.13}$$

where m_i is the mass of atom i and k_B is the Boltzmann constant. This means that we can take influence on the temperature of the system by changing the atom velocities.

In order to control pressure, we first need means to calculate the pressure in a simulated system. The virial theorem [68] allows us to derive an expression for the pressure p:

$$pV = 2\left(E_{\text{kin}} - \langle W \rangle\right) \tag{2.14}$$

where V is the volume of the unit cell, the angled brackets represent a time average, and W is the internal virial:

$$W = -\frac{1}{2}\sum_{i=1}^{N} \mathbf{F}_i \cdot \mathbf{r}_i \tag{2.15}$$

where $\mathbf{F}_i$ is the force acting on atom i with position vector $\mathbf{r}_i$. The right hand side of equation (2.14) can be easily calculated, which provides us with means to control the pressure by adjusting the volume of the unit cell.

A simple algorithm that can be used for pressure as well as temperature control is the Berendsen algorithm. [69] The instantaneous system temperature $\chi_d = T$ or pressure $\chi_d = p$ is coupled to a target value χ_d and is adjusted by

$$\frac{\mathrm{d}\chi}{\mathrm{d}t} = \frac{\chi_d - \chi}{\tau_\chi}. \tag{2.16}$$

The deviation from the target value decays exponentially with a time constant τ_χ. As previously discussed, the volume of the unit cell must be tuned to achieve pressure control. The Berendsen barostat, to provide an accessible example, achieves this by calculating a scaling factor λ for the volume:

$$\lambda = 1 - \beta_T \frac{\Delta t}{\tau_P}\left(P_d - P\right) \tag{2.17}$$

with β_T being the isothermal compressibility and Δt the simulation time step. Pressure is kept constant by scaling all coordinates by $\lambda^{1/3}$. Since the Berendsen barostat is susceptible to oscillations due to the rescaling at each time stage, it is only used for short equilibration runs in this work, whereas the Parinello-Rahman barostat is used for longer production runs. [70]

Similarly, by rescaling velocities every time step by λ, the temperature can be regulated:

$$\lambda = \left[1 + \frac{\Delta t}{\tau_T}\left(\frac{T_d}{T} - 1\right)\right]^{1/2} \tag{2.18}$$

This thermostat, however, does not generate a canonical ensemble because it violates the equipartition theorem. Vibrational, internal kinetic energy is suppressed while translational, external kinetic energy is amplified as the velocities are rescaled. Since the

error grows with each sampling interval, it can cause the 'flying ice cube' complication, in which the damping of internal movements causes the system to freeze. [71] Eventually, we would wind up with an ice cube flying through space due to the acquisition of external momentum. With the inclusion of a stochastic term that preserves the canonical distribution, Bussi et al. [72] solved this problem. This is the Parrinello-Bussi thermostat, also known as a stochastic velocity-rescaling thermostat, is one of the most well-known in MD and still offers a first-order temperature decay.

We have learned before that integration with a symplectic integrator preserves energy and in a periodic box of fixed size volume and particle number are conserved as well, which yields an NVE ensemble. An NVT ensemble is created by coupling the system to a heat bath via a thermostat. For initial equilibration simulations, NVE and NVT ensembles are frequently used because they are more stable and enable the system to reach an equilibrium state faster. An equilibrium state is reached when a set of observables remains relatively stable as time progresses. This serves as a starting point for longer NpT production simulations which produce data for later analysis.

2.1.6. Biasing MD simulation with an external force

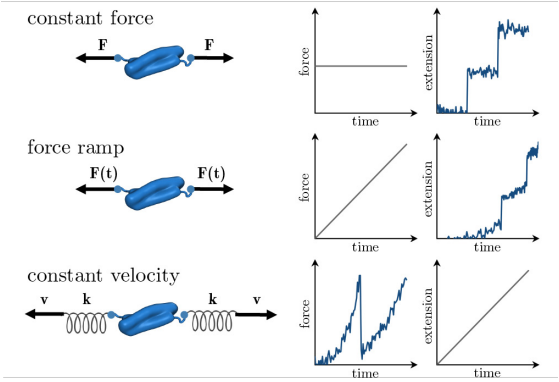

Figure 2.4: External force in MD simulations. A simulation can be biased by a constant force, a constantly increasing force (force-ramp protocoll) and by moving virtual springs with stiffness k away from each other at constant velocity v. The quantity of interest (denoted by the blue lines in the plots on the right) in force-clamp and ramp protocols is the shift in extension over time, while for constant-velocity pulling it is forces over time or extension. Figure adapted from Franz et al. [73]

Biological process are often influenced or guided by mechanical force. The focal adhesion proteins studied in this work are strongly subjected to forces, for example, during cell migration. A protein in the cell might unfold or partly unfold upon some mechanical cue, which can reveal binding sites for other proteins which then bind and start signalling cascades. To study such processes modern MD software offers the possibility of biasing a simulation with a well-defined, external force. These, so-called force-probe MD simulations do not only allow for the investigation of force-dependent processes but are also widely used to study binding and unbinding events in protein complexes which happen without any biasing force *in vivo*, but on timescales not accessible to classical MD. Such events

can take seconds to occur, but the accessible time frame with MD simulations ranges only up to a few hundred microseconds. By biasing the simulation with an external force that pulls the two proteins apart, the likelihood of witnessing a dissociation event is greatly increased. This is not limited to protein complexes; it can also be applied to individual proteins that go through dynamic structural changes, such as the separation of two domains in a single protein. Furthermore, the same approach can be used to artificially unfold an entire protein, which can yield useful biological insights. [74] In MD simulations, the external force can be added directly to the atomic force determined in equation (2.7). This force may be applied to an individual atom or to the center of mass (COM) of a group of atoms. In the latter case, the total force is distributed in a mass-weighted manner among the group members.

The magnitude of the added force can be regulated in three ways, all of which are conceptually distinct. Firstly, the magnitude of added force can be constant over time, which is referred to as *constant force* pulling. Secondly, the force can ramped up over time, in so called force-ramp simulations. Thirdly, the magnitude of the force can be controlled by a harmonic potential defined by the distance between the pull group and a reference point. In *constant velocity* pulling, the reference point travels at a constant speed in a specific direction. In umbrella sampling, for example, the harmonic potential is used to tether an atom the COM of a group of atoms to its initial position, to eventually determine the potential of mean force along a reaction coordinate. This is why the harmonic potential used in constant velocity pulling is also known as umbrella potential. Figure 2.4 shows how these concepts can be applied to unfold a protein. The force can be set to move an atom or atom group in a specific direction, or it can be set to act along a vector connecting two atoms or atom groups, in which case the force acts on each of these pull groups, pulling them closer together or apart.

2.1.7. Free energy calculations by umbrella sampling

The calculation of free-energy differences is crucial for the understanding of any molecular or macro-molecular behaviour as it constitutes the driving force behind chemical and biological processes alike. Combined with transition-state theory [75, 76] the knowledge of the height of free-energy barriers allows for the calculation of rates, which can be applied to chemical reactions, as well as protein unfolding, or protein-ligand binding and unbinding. In theory, the Helmholtz free energy F in an NVE ensemble can be calculated from the canonical partition function $\mathcal{Z}$ as $F = -k_{\mathrm{B}}T \ln \mathcal{Z}$. If we change the ensemble to NPT, we instead need to obtain the Gibbs free energy $G = F + pV$. In MD simulations,

the free energy differences ΔG and ΔF are often similar as the comprehensibility of condensed matter is small. [77]

To calculate $\mathcal{Z}$, an integral over the entire phase space has to be evaluated, which is not possible with computer simulations. However, in an ergodic system, if every point in phase space is visited, the ensemble average becomes equal to the time average for infinite sampling. This means, that with sufficient sampling along a reaction coordinate ϵ, we can, in principle, calculate the free energy difference. There is a variety of methods available to achieve the required sampling and Kästner [77] provides a nice overview. Here, we use umbrella sampling [78, 79] which will be briefly explained in the following.

The central idea behind umbrella sampling is to apply a bias ω to the simulation to attain sampling in all regions of ϵ, which then allows the calculation of the free energy profile $A(\epsilon)$ along the reaction coordinate. Evidently, the ideal bias potential would be $\omega_{\text{ideal}} = -A(\epsilon)$, but $A(\epsilon)$ is the quantity we want to calculate. Commonly, ϵ is split into a number of windows and a harmonic potential is applied to keep the system close to $\epsilon_{\text{ref},i}$. The choice of the number of windows and the strength of the harmonic potential are critical as they define how well the windows are sampled. The the spring constant of the harmonic potential must be strong enough to drive the system over the barrier, but if it is too high the resulting distributions are very narrow which would require a high number of windows for the distributions to sufficiently overlap. This overlap is indispensable for the weighted histogram analysis method (WHAM). [80, 81] For the WHAM, one first corrects the distributions generated with a bias potential $P_{\text{b},i}$ to obtain the unbiased distribution $P_{\text{u},i}$ as follows:

$$P_{\text{u},i}(\epsilon) = P_{\text{b},i} \exp \beta\omega_i(\epsilon) \cdot \langle \exp -\beta\omega_i(\epsilon) \rangle, \tag{2.19}$$

where $\beta = (k_{\text{B}}T)^{-1}$. In the next step, an iterative process minimizes the statistical error of

$$P_{\text{u}}(\epsilon) = \sum_{i}^{\text{windows}} p_i \cdot P_{\text{u},i}(\epsilon) \tag{2.20}$$

by tuning the weights p_i under the condition $\sum p_i = 1$ until convergence.

2.2. Recent progress in molecular simulations of protein mechanical properties and function and interplay with experiments

This section[1] is intended to highlight how recent scientific progress has propelled the synergy of simulations and experiments.

When it comes to researching the reaction of molecules to mechanical force, single-molecule force spectroscopy (SMFS) and classical MD simulations are natural allies. Recent developments in both experiments and simulations have made it easier to compare SMFS and MD data directly, most notably by closing the time scale gap, which previously encompassed at least 5 orders of magnitudes. On the one hand, recent methodological developments in molecular simulations, especially molecular dynamics (MD) simulations, have expanded the timescales that simulations can cover. Emerging high-speed AFM techniques, on the other hand, allow for higher pulling speeds in experiments. As a result, the first and favorable direct quantitative comparisons of expected and experimentally tested rupture forces are of recent nature and briefly highlighted in the following.

2.2.1. External forces in all-atom MD simulations

Although the fundamental concepts of force simulations have remained unchanged, substantial improvement has been made in three areas.

First, due to rapidly advancing semiconductor technology and MD code efficiencies, explicit solvent pulling velocities of less than 1 m/s are now possible and in recent years, speeds as low as 0.001 m/s have been recorded. [82, 83]

Second, studies provide several or even hundreds of trajectories for a given set of parameters, rather than presenting single trajectories. Recent studies' vast number of trajectories make for ample statistics on unfolding forces (with *constant velocity pulling*) or unfolding times (with *constant force pulling*). This allows for a much better understanding of the mechanisms that underlie the mechanical reaction of the studied protein. Recent examples of detailed statistics include 10-100 unfolding trajectories of spectrin domains for a given pulling velocity [84] or the extensive study of the loading-rate-dependent transition from catch to slip bonds in fibrin. [85]

Third, rather than focusing on the mechanical stability of individual protein domains, researchers have recently turned their attention to broader multi-domain structures and

[1] based on our publication *'Advances in molecular simulations of protein mechanical properties and function'* [73]

their mechanosensing and mechanotransduction capabilities. Focal adhesion proteins are particularly intriguing as potential candidates and two of them, namely talin in vinculin are the center of this work and extensively discussed in remainder of this thesis. The following gives two notable other examples in the context of focal adhesions. Using cell experiments and MD simulations, a set of distinct salt bridges in alpha-catenin was found to be essential for the protein's mechanosensing function, [86] and simulations of an integrin-kindlin dimer by Jahed et al. [87] indicated a shift in interactions at the dimerazation interface under integrin-mediated stress, which – similar to a catch bond – strengthens focal adhesions under force.

The study of cell-cell junctions saw a similar change in focus, shifting from single domain proteins to larger multi-domain proteins and protein-protein interactions. Protocadherin-15, for example, is involved in the mechano-transduction of sound signals and, consequently, loss of hearing and balance disorders. De-la-Torre et al. [88] compared unfolding forces to dissociation forces for various pulling velocities and thereby identified a newly resolved MAD12 domain of protocadherin-15 to render this and potentially other cadherins highly extensible. MD simulations combined with small-angle x-ray scattering showed that an interdomain bent feature gives protocadherin-15 even more elasticity. [89] More recently, Choudhary et al. [90] combined structural, biochemical, and simulation data to provide an integrated atomistic view of the protocadherin-15 ectodomain, which can act as a stiff or soft gating spring.

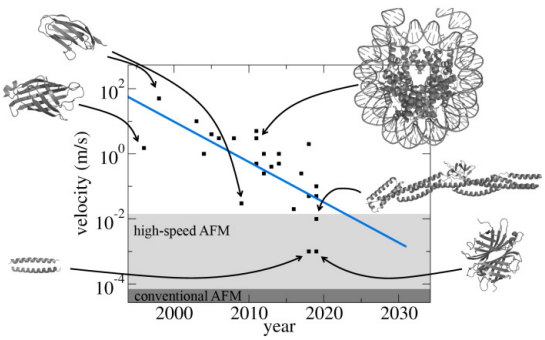

Figure 2.5: Historical development of pulling velocities. Pulling speeds have been on a steady decline over the last two decades, roughly following Moore's law with a halving every two years. To highlight the variety of featured system sizes, the structures for some of the studied proteins are given; starting from the top right in clockwise direction: nucleosome [91], desmoplakin [92], streptavidin-biotin complex [82], coiled-coil [83], streptavidin-biotin [93], immunoglobulin [94, 95]. Figure adapted from Franz et al. [73]

As indicated by the examples featured in figure 2.5 – which are by no means extensive – pulling speeds have declined steadily. Moore's law suggests a doubling in the number of transistors per square inch every other year and is therefore in very good agreement with the development of pulling velocities. Nonetheless, they have lagged behind the protein MD simulation times which have undergone a cumulative doubling every 1.3

years approximately. [96] This is most certainly attributed to the above-mentioned recent emphasis on expanded statistics and more expansive biological systems.

2.2.2. Experiments and simulations of protein mechanics

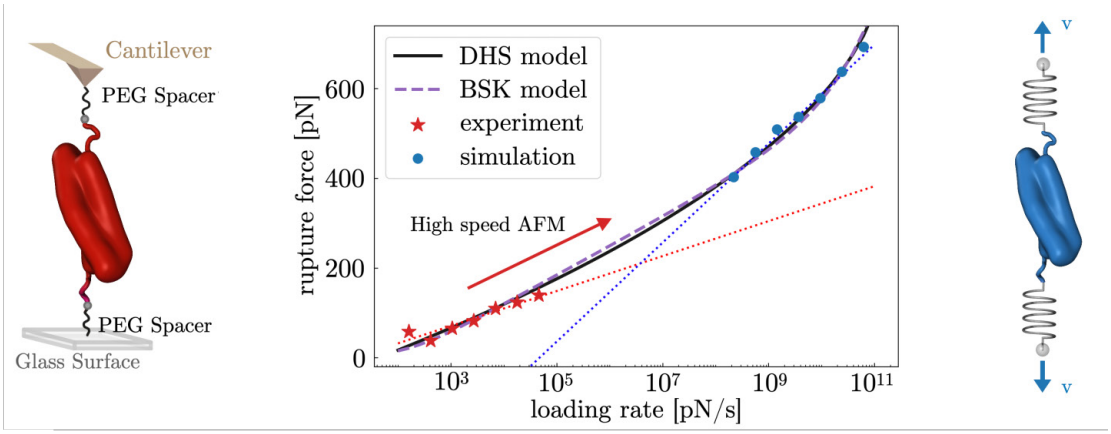

Figure 2.6.: Rupture-force-over-loading-rate relation. The centre panel shows exemplary data from MD simulations (illustrated in the right panel) and AFM experiments (illustrated in the left panel). Interpolation between the two regimes works reasonably well with the DHS and the BSK model, whereas the Bell model only gives acceptable accuracy if either the experimental or computational subset of the data is considered. Figure adapted from Franz et al. [73]

In the past, comparing simulated protein unfolding to AFM studies has been problematic due to the vast differences in loading rates of the two techniques. With cutting-edge high-speed AFM and GPU acceleration, AFM and MD velocities are now approaching or even partially overlapping. To model the dependency of rupture forces on loading rates, a number of theoretical frameworks have been developed.

First and foremost, the well-known Bell model, [97] which postulates a linear relationship between rupture forces and the logarithm of loading rate, is frequently a good match for simulation or AFM data that only covers a few orders of magnitude in loading rate. However, the bell model tends to be insufficient for bridging the wide spread between simulation and experiment. When studying a particular system with force-probe simulations and AFM experiments, one usually observes steeper slopes in the rupture-force-over-loading-rate relation if one only fits the Bell model to the MD data. A fit to the AFM data would usually yield much more gradual slopes, which makes an interpolation over the wide range of loading rates spanned by the combination of both methods infeasible. As a matter of fact, data from this hypothetical study would be best fit with a curved function (see figure 2.6). The following models have been proposed to introduce curvature in the

rupture-force-over-loading-rate relation: 1) The Bullerjahn-Sturm-Kroy (BSK) [98] model aims to explain the difference in slopes by a gradual change from a thermally activated, and hence probabilistic regime at small loading rates to a deterministic regime at high loading rates. 2) Dudko et al. [99] suggest that the distance to the transition state is decreasing with rising force. Furthermore, Pierse and Dudko [100] have proposed that conformational changes in proteins typically occur through a variety of pathways which may result in several obstacles along a reaction coordinate (not included in figure 2.6). The rupture-force-over-loading-rate shows a similar curvature in models that account for friction with water molecules, which inevitably increases with velocity. [101] As we have shown, there is a variety of theoretical approaches available that can explain the curvature that typically occurs in these scale-bridging studies. The reality is most likely a combination of them all, which makes the interpretation of such data a challenging task.

2.3. Ultra-long magnetic tweezers single protein experiments

In addition to AFM experiments, the use of magnetic tweezers constitutes another valuable single-molecule technique that allows the investigation of proteins under force. The principle behind the setup used by our collaborator on one of the projects presented in this thesis, Dr. Rafael Tapia-Rojo, is straightforward. A single molecule is tethered between a glass cover slide and a superparamagnetic bead. The latter is moved by a controlled magnetic field, which effectively applies force to the molecule. Simultaneously, the extension of the protein is measured in real time by tracking the z-coordinate of the bead.

In the extension to classical magnetic tweezers developed by Tapia-Rojo et al. [59], a tape head – basically an electromagnet – allows for the variation of the magnetic field which, in turn, permits the exertion of a precisely specifiable force on the superparamagnetic bead. Forces remain stable over timescales spanning several hours. [102, 103] Using the Karlqvist approach for calculating the magnetic field of a tape head, [104] a fully analytic description of the pulling force in relation to the distance to the superparamagnetic bead and the electric current is available. [103]

Using a camera with high read-out frequency and real-time image analysis, the relative z-position of the bead is inferred with respect to a non-magnetic reference bead. Prior to measurements, a z-stack library is built with the radial patterns of the reference bead. For this, the intensity of pixels with equal radius is integrated in the Fourier-transformed image of the bead. This gives a measure of the rings at different focal planes which is

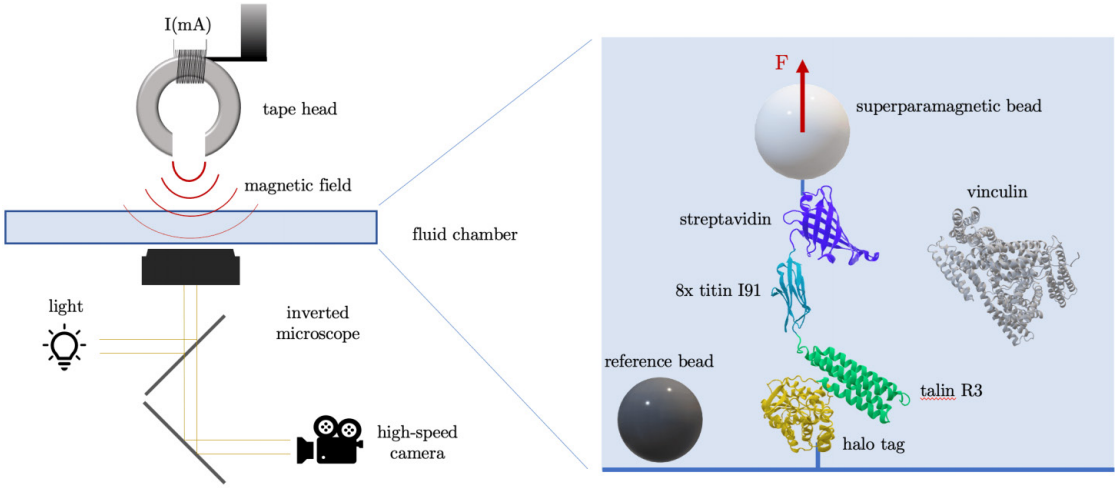

Figure 2.7.: Tape-head magnetic tweezers setup. Schematic representation of the magnetic tweezers setup used by Dr. Rafael Tapia-Rojo. Within the fluid cell a (talin-R3)-(titin-I91)$_8$ construct is covalently tethered to a glass coverslip by a halo tag, and to a streptavidin-coated magnetic bead by a biotin molecule. The solution in the fluid cell contains full-length vinculin and the distance between a reference bead and the magnetic bead is determined with an inverted microscope and a high-speed camera which are mounted underneath the fluid cell. The talin R3 domain is stretched via the magnetic bead which is controlled by tape head that finely controls the magnitude of the pulling force with an electrical current. The figure was inspired by Tapia-Rojo et al. [103], [59] to represent the setup used for the data presented in chapter 4.

then correlated to the radial vectors during the measurement. Thereby, a Gaussian fit on their Pearson's correlation [105, 106] yields two peaks, one for the magnetic bead and on for the reference bead. The distance between the two peaks gives the extension of the protein. Combining this with a calibration procedure that uses the unfolding of protein L and the theoretical worm-like chain model, the instrument can be provide precise control over a wide range of forces.

Figure 2.7 shows the setup used by Dr. Tapia-Rojo for the experiments that are featured in chapter 4 of this thesis.

2.4. Analysis methods for MD trajectories

Particularly in the light of the rapidly increasing amount of data that MD simulations can generate, efficient frameworks for their analysis are essential. This section aims to explain the principles behind the analysis tools used in this thesis.

2.4.1. Generalized correlated motions

The assessment of correlated motions is a very powerful tool to analyze conformational dynamics in biomolecules and can yield insights about the propagation of mechanical energy and allosteric signals. A popular method from general statistics which is also widely used to calculate correlations of motions within biomolecules from MD simulation is the Pearson correlation coefficient. [105, 106] To quantify the correlation of atomic fluctuations with the Pearson coefficient, the normalized covariance matrix is calculated as follows:

$$C_{ij} = \langle x_i \cdot x_j \rangle / \sqrt{\langle x_i^2 \rangle \langle x_j^2 \rangle} \tag{2.21}$$

Complete correlation where two atoms move with the same phase and the same period will result in $C_{i,j} = 1$. Completely anti-correlated motions give $C_{i,j} = -1$. The correlation measure, however, is only reliable if the angle between the directions of motion is near $0°$ or $180°$ degrees, that is, if x_i and x_j are co-linear vectors. In practice, this means two atoms which exhibit perfectly correlated oscillations with a $90°$ angle between their directions of motion will give a highly misleading Pearson correlation coefficient of $C_{i,j} = 0$. Second, this method is limited to the detection of linear correlations. By relying on the covariance matrix, one implicitly assumes a Gaussian distribution of the configurational space density. Because of this approximation, any higher order correlations cannot be captured. Lange and Grubmüller [107] address these drawbacks with a generalized correlation measure that leverages the concept of mutual information from statistical mechanics. Mutual information is measure for how different the joint distribution of two random variables is from the product of their marginal distributions. For truly independent random variables X and Y, the product of their marginal distributions equals their joint distribution, $P(X, Y) = P(X) \cdot P(Y)$, and their mutual information is zero. The Lange and Grubmüller [107] correlation, or generalized correlation, is defined as the deviation from this equality. The result is similar to the Shannon mutual information: $C(X, Y) = H(X) + H(Y) - H(X, Y)$, where C is the generalized correlation measure and H the entropy of the random variable. [108] With this approach any correlation can be captured and the result is invariant to scaling.

2.4.2. Force distribution analysis

Force distribution analysis (FDA) is a powerful tool for the study of the conformational space of biomolecules. While the detection of correlated motions relies on the time-resolved

atom coordinates, FDA uses internal forces. This comes with an advantage over correlation analysis in that the forces are intrinsic coordinates which makes them independent of the protein's translation and rotation. Furthermore, Costescu and Gräter [109] demonstrated that FDA can detect very low-amplitude, yet functionally significant fluctuations in a protein core, which establishes FDA as a highly sensitive framework.

FDA is solely based on MD simulations and is implemented as an extension to the GROMACS [110] simulation suite. Pair-wise forces are calculated and the length of the force vector is stored in so called 'force trajectories'. The focus on vector length rather than the vector itself ensures the above mentioned invariance to rotation and translation. Attractive and repulsive forces can still be distinguished as they are stored with opposing signs. Since the interpretation of the resulting data is based on time-averaged forces, it is essential to provide vast sampling of the conformational space in order to reduce noise and achieve meaningful results.

The pair-wise forces can be used to identify a protein's reaction to a mechanical or allosteric cue. More precisely, only the difference in pair-wise forces for two separate states yields interesting insights. FDA is used in this study to measure the allosteric disparity between a protein's apo and holo states. By comparing to an undisturbed reference, the method can be used to investigate any form of perturbation on a biomolecule. The best practice is to compute several independent trajectories for both the reference and perturbed states. Then, one calculates the difference in pair-wise forces ΔF_{ij} from the time-averaged data over all perturbed ($F_{ij,\mathrm{pert}}$) and unperturbed ($F_{ij,\mathrm{ref}}$) trajectories as follows:

$$\Delta F_{ij} = F_{ij,\mathrm{pert}} - F_{ij,\mathrm{ref}}. \tag{2.22}$$

A simple way of visualizing the force differences is given by a mapping from the pair-wise space to the atom space via the column-wise sum

$$\Delta F_i = \sum_j |\Delta F_{ij}|. \tag{2.23}$$

This atom-wise force differences can now be visualized with the help of a color map on a 3D structure. Additional insights may be obtained with a network representation. For this, the pair-wise forces are considered edges that connect atoms and each edge is weighted by the magnitude of ΔF_{ij}. With the introduction of a cut-off, a set of paths is generated that connects atoms that experience a force difference lager than the cut-off

($\Delta F_{ij} > \Delta F_{\text{cut-off}}$). To identify important networks that might mitigate allosteric effects, one typically considers the longest paths in the set.

2.4.3. Contact analysis

Intra- and intermolecular contacts can be visualized and interpreted with the help of a contact map. Contact maps are related to distance maps which are two-dimensional (2D) matrices that are constructed using the pair-wise residue-residue distances. A contact map is essentially a distance map with a user-defined cut-off that is appropriate for the molecule under investigation. Probably the most well known example for the use of contact maps is Google Alpha Fold's, which achieved outstanding performance at the CASP13, a contest where computational methods compete to predict the a protein structure with nothing but amino acid sequence as a starting point. [111] All features of secondary and tertiary structure that characterize the examined molecule can be captured and represented by contact maps. A bulging of the matrix diagonal identifies helices and narrow off-diagonal contact stripes represent antiparallel β-sheets, whereas contact stripes that lie orthogonal to to contact map diagonal indicate parallel β-sheets.

The contact analysis software ConAn, developed by Mercadante et al. [112], provides a simple way of performing a contact analysis on MD data. In addition to time-averaged data, ConAn provides means to analyze the time evolution of residue-residue contacts in an automated manner. This can be very valuable for the analysis of structural changes that happen during a MD trajectory.

3

The interplay between talin and the cell membrane

3.1. Autoinhibited talin structure and PIP2

Talin is arguably the most important protein in the focal adhesion complex. It binds to the cytoplasmic tails of integrins as well as to actin filaments, making it one of the most direct links between the extracellular environment and intracellular processes. It has been shown to activate integrins, which enhances their affinity for extracellular ligands and also to provide the groundwork for the recruitment of additional focal adhesion proteins on the intracelluar level. [113] The binding partners of talin illustrated in figure 1.2 encompass only a subset of the multitude of possible binding partners of this protein. For talin to be able to bind to its full range of partners, it first must overcome its auto-inhibited conformation. The focus of this section lies on a possible activation mechanism of the protein that is mediated by binding to a PIP_2-rich lipid membrane. Other binding

This chapter evolves around the results obtained by Jannik Buhr and me in the course of his master's project that I supervised.

partners that bind to talin and build up the focal complex and adhesions have been reviewed elsewhere. [12]

Talin is a 270 kDa heavy protein that exists in two isoforms, talin-1 and talin-2, encoded by the TLN1 and TLN2 genes, which share 76% sequence identity. [114] The expression of the two isoforms, however, varies considerably. While talin-1 is consistently expressed in all types of tissue, talin-2 is not present in certain cell types like, for example, endothelial cells. If none of the talin isoforms is present in a cell, focal adhesion stabilization and maturation are not possible, as has been demonstrated by confocal-microscopy experiments on talin knockout cells. [57]

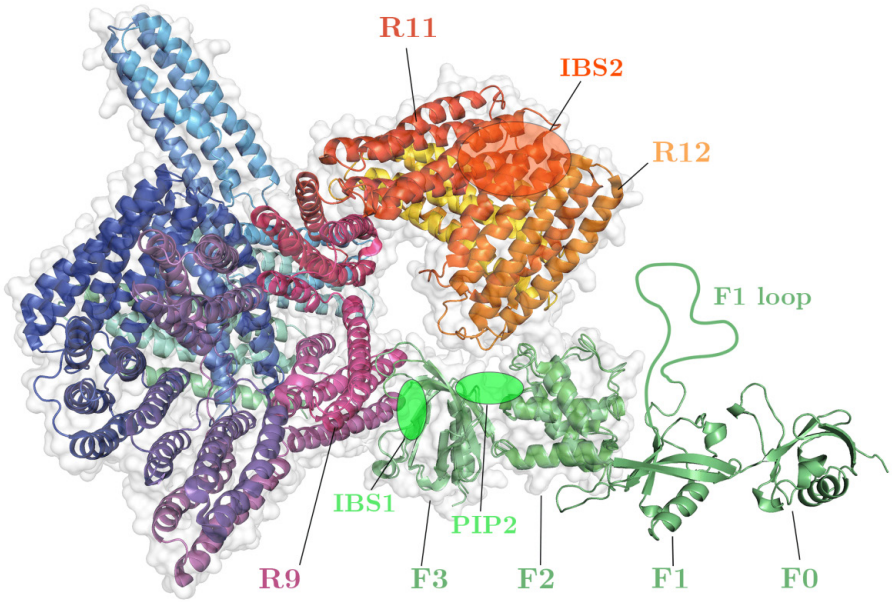

Figure 3.1.: Talin assumes an autoinhibited conformation in the cytoplasm. The structure of the autoinhibited talin by Dedden et al. [56] encompasses the whole tail domain and two subdomains of the FERM domain. To illustrate how the complete autoinhibited protein likely looks, a structural overlay with the complete FERM domain (green) [57] is shown. The loop, which is missing from this crystal structure, is painted in for illustrative purposes.

In the length of the talin protein, there are two integrin binding sites. The first and most significant is IBS1, which is found in the FERM F3 domain. IBS2 is found on the talin tail's R11 domain. Since talin can dimerize, a single talin homodimer can potentially bind up to four integrins, which provides the means for talin to grow focal adhesions. For simplicity, figure 1.2 only shows one interaction site of talin with actin, while, in fact,

talin has three actin binding sites which underlines the protein's pivotal role within the focal adhesion machinery. When actin and integrin are bound simultaneously to talin, mechanical tension along the talin rod exposes vinculin binding sites, [115] which helps to further strengthen growing focal adhesions. The recruiting of vinculin which, in turn, can bind to more actin filaments results in a scenario in which an increasing force leads to stronger focal adhesions which distribute the force over more connections, i.e. a negative feedback loop.

Whenever an integrin is associated to talin, the integrin's binding affinity for ECM ligands is significantly increased, [12] a concept which is known as inside-out activation. Conversely, there is also an outside-in activation mechanism that is yet to be thoroughly understood. As mentioned previously, one of the IBS of talin is located in its head domain, or FERM domain, which is short for four-point-one protein, ezrin, radixin, moesin. This nomenclature represents a settlement between the early in initial identification of this domain, which has been found in numerous peripheral membrane proteins like FAK, PYK2, kindlin, and talin. [116–118] Talin's FERM domain, however, is peculiar as it has four subdomains and the solved crystal structures available at the time this project was commenced suggest that it takes on a rod-like conformation. Most other FERM domains comprise only three subdomains arranged in a cloverleaf-like structure. [57, 119]

Of the four subdomains of the talin FERM domain, labeled F0-F3 (see figure 3.1), F1, F2, and F3, have been shown to bind to PIP_2 containing membranes in experiments (see figure 1.2). [120–122] As elaborated upon section 1.1, at nascent focal adhesion the GTP-binding protein Rho causes a local increase in PIP_2 concentration, reaching up to ~10%. [36] Literature points towards an important role of PIP_2 in talin activation and recruition: In a mutation study, Bromberger et al. [123] were able to show that RAP1 binding sites, as well as the PIP_2 binding sites on F3 and F4 were necessary to activate and localize talin at the cell membrane. The importance of the F3 and F4 PIP_2 binding sites is further underlined by data provided by Moore et al. [38], who demonstrated that an isolated F3F4 domain binds almost as strongly to a PIP_2-enriched membrane as the entire isolated FERM domain, whereas the F0F1 binds with much smaller affinity. Consistent with this, Chinthalapudi et al. [57] – whose crystal structure forms the basis for the investigations in this chapter – identify only one major binding site for PIP_2 in a shared location between the F2 and F3 domain. The position of the binding site partially overlaps with the patch in F2F3 that binds to the R9 domain locking talin in an autoinhibited conformation. This provides an explanation as to why lipid vesicles rich in PIP_2 compete with the talin R9 domain in experiments. [124] Furthermore, the F1 subdomain features an extensive loop, which was first identified by Goult et al. [122].

This loop is present in both talin isoforms and can interact with vesicles that contain negatively charged phospholipids. Their findings also indicate that the loop plays a key role in the activation of β1-integrins. In the cytoplasm, talin maintains its autoinhibited conformation [55] and the recently published talin crystal structure by Dedden et al. [56] (Figure 3.1) further confirms that the primary PIP_2 binding sites as well as the IBS, are cryptic. However, recent findings with synthetic membranes show that the presence of negatively-charged phosphoinositides is sufficient to recruit talin to the membrane, which in turn localizes vinculin and actin to the membrane. [42] Hence, the question of how the inactivated talin is recruited to the FA in the first place remains unanswered. A possible path towards the solution to this mystery starts with the large basic loop in the F1 subdomain and its possible interaction with the cell membrane.

The following sections aims to elucidate the role of the F0F1 domain in tethering talin to the cell membrane. The presented molecular dynamics simulations hint towards an activation mechanism in which the F0F1 establishes an initial link to the membrane which facilitates the binding of the F3F4 PIP_2 binding sites, and consequently talin activation. Using force-probe MD simulations, we go on to show that the F0F1 domain plays an important part in keeping talin attached to the membrane once the focal adhesion is subjected to force.

3.2. Methods

The simulations presented and analyzed in this chapter are based on a crystal structure of the FERM domain of talin published by Chinthalapudi et al. [57] with pdb-ID 6MFS. The structure does not contain a loop-like region within the F1 domain between L133 and W144. To include the loop in our simulations, we inferred its conformation using MODELLER [125–127] within Chimera. [128] The GROMACS input files for the membrane-protein systems were built combining the CHRAMM-GUI web app [129] and several GROMACS tools. [110] All simulations feature Tip3p water and were neutralized with a concentration of 0.15 mol/L of NaCl. After gradient decent energy minimization, a 6-step equilibration process gradually relieving restraints on protein and membrane was performed. The integration time step for production runs was set to 2 fs. Van-der-Waals interactions were treated with a Verlet cut-off scheme and long-range electrostatics were computed with the Particle Mesh Ewald method. Nosé-Hoover temperature coupling [130, 131] and semi-isotropic Parinello-Rahman pressure coupling [70] ensured an NPT-ensemble.

The initial equilibrium simulation of the talin FERM domain in water was run for 75 ns, and the average structure and root mean square fluctuation (RMSF) were calculated

with GROMACS. [110] The truncated system containing residues 1 to 197 (F0F1) used for protein-membrane-association simulations was assembled using an in-house script which placed the protein 1.5 nm away from a POPC membrane in multiple orientations, totalling 360 simulations, of 50-200 ns and a cumulative simulation time of 60.5 µs. Of the 119 lipids in the upper leaflet of the used POPC membrane, 12 lipids were PIP_2s to mimic a 10% concentration.

Two sets of equilibrium simulations were run for the entire FERM domain. In both cases, a POPC membrane with 26 PIP_2 lipids in the 273 lipids of the top leaflet was used. The first system features the modelled loop and was simulated in 7 replicas for 400 ns each. The second system was based on the unmodified crystal structure (pdb-ID 6MFS, [57]) where the crystallized PIP_2 head in was converted into full lipid using pymol. To avoid overlap between the membrane and the protein, the lipid extruded slightly from the membrane, which is why a 50 ns equilibration was run to restore the integrity of the membrane. Subsequently, 8 replicas of 1 µs were simulated.

From the loop-containing equilibrium simulations, we selected a common and representative configuration with high membrane-protein association level to initiate force-probe MD. An in-house script was used to convert the 10% PIP_2 concentration to ~1% (3 PIP_2 molecules of 273 lipids). Both systems were pulled with two pulling directions and two pulling speeds for a cumulative simulation time of 7.2 µs.

3.3. Completing the structure of the talin FERM domain

The first challenge that arose when aiming to simulate the influence of the F1 loop on FERM-membrane interactions was that it is omitted by the FERM crystal structures available at the time of writing this thesis, [57, 119] presumably because it is too flexible to be reliably crystallized. The only available structural data on the F1 loop comes from an NMR ensemble [122] that encompasses a number of very different conformations of said loop. Given the entailed flexibility, the exact initial loop conformation for our simulations is not extremely relevant if the flexibility is preserved in simulations. Hence, we chose to complete the most recent crystal structure of the FERM domain (pdb-ID 6MFS, [57]) using MODELLER. [125–127]

The RMSF during an preliminary 75 ns-long equilibration simulation reflects the high flexibility of the loop (see figure 3.2). A visual inspection of the trajectory confirmed sampling of a large conformational space in the loop region validating our approach by suggesting that the modelled starting structure of the loop constituted a negligible bias to

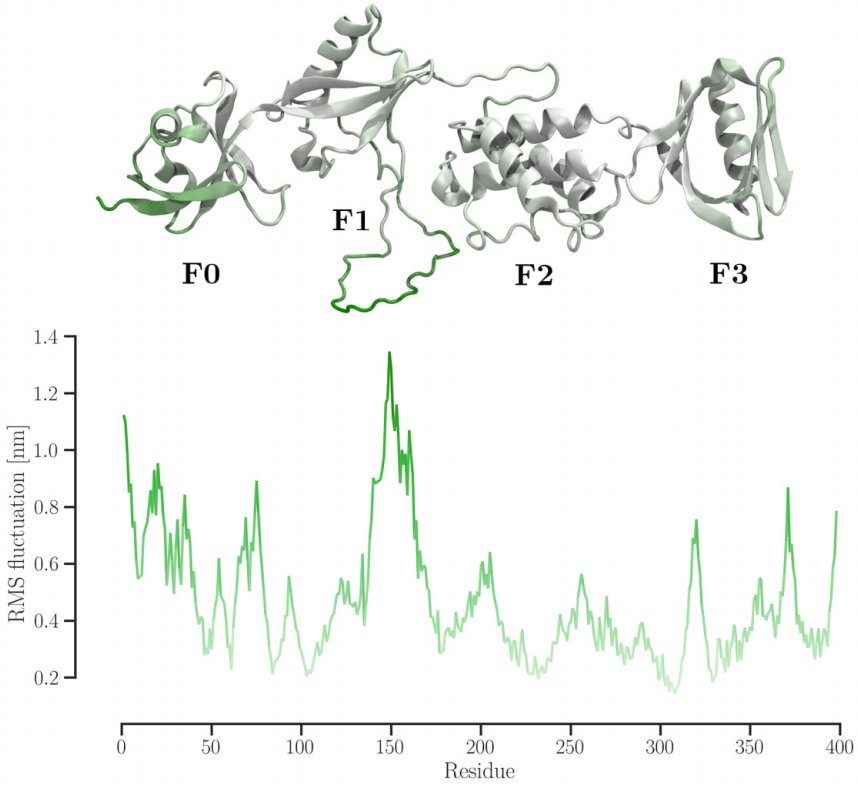

Figure 3.2.: The F1 loop is the most flexible region in the talin FERM domain. *Top)* The average structure resulting from the last 10 ns of a 75 ns equilibration simulation is shown in cartoon representation. The color code represents the magnitude of the Root mean squared fluctuations at a given residue. *Bottom)* RMSF over residue number, the hue serves as a guide to the eye for comparison with the top structure.

the simulation outcome. The second highest flexibility was observed for the F0 domain, whereas the F2F3 domains exhibited the smallest fluctuations. This is interesting because F2F3 are in contact with the talin tail in the autoinhibited conformation (see figure 3.1), which would only further stabilize them. Can we assume that the high relative flexibility of F0F1 and particularly of the loop is actually a feature which helps in the search for binding partners and thereby can alleviate the autoinhibition?

3.3.1. The F1 loop, a potential first contact site?

To study the potential membrane binding capabilities of the F1 loop, this first subset of simulations was limited to the F0F1 domain and a POPC membrane patch with 10% PIP_2 in the upper leaflet, which is depicted in figure 3.3. The smaller system size allowed

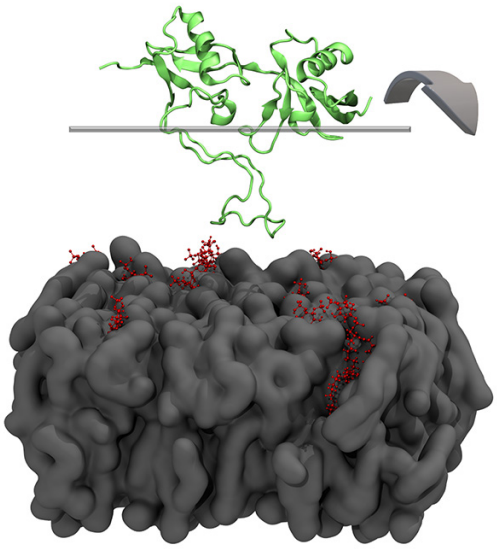

Figure 3.3: Representation of the system used for the rotational sampling. The F0F1 construct (green cartoon) was distanced 1.5 nm away from a PIP_2 containing POPC membrane (grey surface). One in ten lipids of the upper membrane leaflet was a PIP_2 lipid (red). The protein was rotated around an axis chosen to feature the state in which the loop is in maximal proximity to the PIP_2 containing leaflet as well as the state in which it is maximally distant. A set of six independent simulations was spawned every 6° resulting in a total of 360 simulations.

an extensive sampling which is important as binding events are not always within the accessible time scale of MD simulations [132] and, here, we started from an unbound conformation. The protein was positioned at a small distance of 1.5 nm away from the membrane as a starting point; the conformation is depicted in figure 3.3. The two 300 ns-long simulations of the system showed that the loop did indeed make contact with the membrane quickly and, even more importantly, once the loop has established a link to the membrane, more contacts with the remainder of the protein followed. To eliminate any bias arising from the initial conformation and to confirm whether or not the loop can initialize membrane binding, we carried out a 'rotational sampling' approach. To this end, the protein was rotated around an axis parallel to a vector connecting N and C-terminal residues. Six independent simulations were started for every 6° of rotation, resulting in a total of 360 trajectories with 60 different staring conformations.

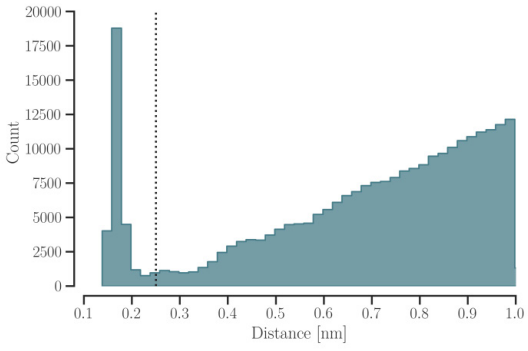

Figure 3.4: Threshold contact distance. The histogram gives the distribution of distances between the protein and PIP_2 in the membrane. Distances were evaluated every 100 ps and are only shown if smaller than 1 nm. Any distance below 0.25 nm is counted as a contact.

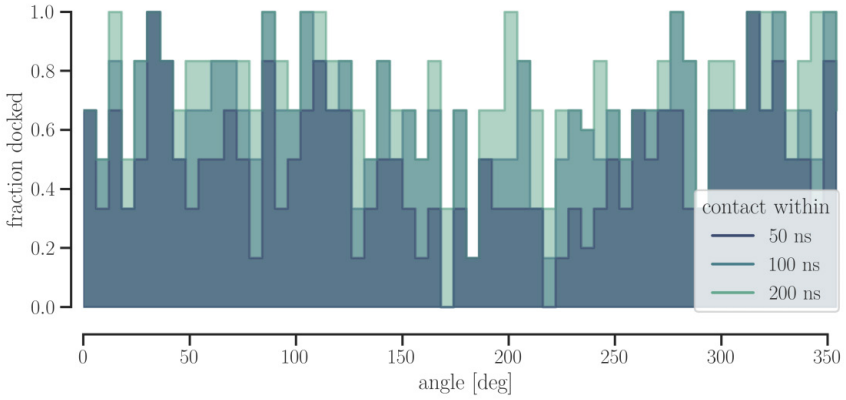

Figure 3.5.: Rotational sampling revealed high association rate. The 360 trajectories from the rotational sampling were classified depending on when tethering to the membrane occurred. The figure shows what fraction of the simulations made contact within the first 50, 100, or 200 ns. A trajectory that, for example, has made contact within the first 50 ns, but has only a total length of 100 ns will still be counted for the 'within 200 ns' group. The reference is always the total of simulations started.

To be able to analyze in which of the simulation a link to the membrane was established, a contact criterion needed to be defined. A suitable decision boundary was found by examining the distribution of distances between the the protein and any PIP_2. Figure 3.4 shows how protein–PIP_2 distances are distributed over the course of the simulations. Note that we considered the minimum distance between any two atoms of the molecules in question. While exhibiting a pronounced peak at a distance of ~0.16 nm, rather in contrast to the gradual increase for distances larger than 0.35 nm, a comparatively small number of observations fell within the range between 0.20 and 0.35 nm. Consequently, a distance of 0.25 nm is well-suited for distinguishing the bound from the unbound state.

While simulations were intended to run for 200 ns, issues with the HPC infrastructure led to some trajectories being shorter. Out of the 360 runs, 358 completed at least 50 ns, 337 completed 100 ns, and 304 completed at least 165 ns. Out of the entire ensemble, 243 simulation formed a stable connection with the membrane. Nonetheless, of the 23 simulations covering no more than 100 ns, only six did terminate without previously binding to the membrane. Figure A.1 in the appendix shows in detail how long simulations ran and that there was no bias from certain angles being simulated for longer time spans. For every run, the time of first contact was recorded. Figure 3.5 shows what fraction of the initially started simulations docked to the membrane for a given starting angle and whether the contact was established within the first 50, 100, or 200 ns.

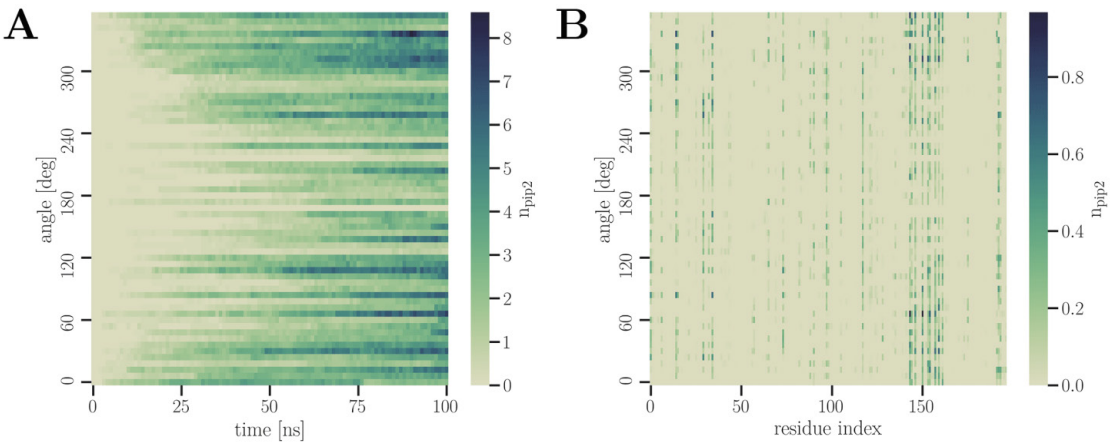

Figure 3.6.: Loop-membrane association was observed for all starting angles. *A*) The heat map illustrates the average number of PIP_2 molecules that were interacting with the F0F1 construct at a given time for a given angle during the first 100 ns. Here, the average refers to the ~6 simulations that are available per angle. *B*) The heatmap illustrates which residues in F0F1 were most involved in PIP_2 binding. The average number of associated PIP_2 is shown for each residue. To calculate the average, all simulations were considered, but excluding the first 50 ns, as the number of contacts below this time threshold was small. This implies a selection bias, for which this figure should only serve for a qualitative interpretation.

Overall, the association rate was very high, as in 75% of the trajectories a connection formed between protein and membrane. If the loop was oriented more towards the membrane, binding tended to occur on a faster time scale. Thereby, the range of favorable angles was large and encompassed more than the ones in which the loop was oriented directly towards the membrane and binding oftentimes occurred within the first 50 ns. Only in the region at around 180°, the fraction of associated proteins was comparatively smaller within the first 50 ns, but caught up during the subsequent 150 ns. Taken together, association was slower yet very likely for unfavorable angles. Figure 3.6 shows this process in more detail by depicting the average number of PIP_2s among all simulations that ran for at least 100 ns for every angle and time frame. It is immediately obvious that the time to binding increased with the distance from the loop to the membrane. This goes to show that, when concerning the F0F1 construct, it was indeed the F1 loop that first anchored the protein to the membrane. And more importantly, the loop had the capabilities of 'finding' the membrane quickly, even if the starting condition was such that the loop was turned away from the membrane completely. From figure 3.6, we can also discern a cluster of PIP_2 interactions between T144 and K162, precisely the region of the flexible loop, underlining that the loop was the most important actor when binding to PIP_2.

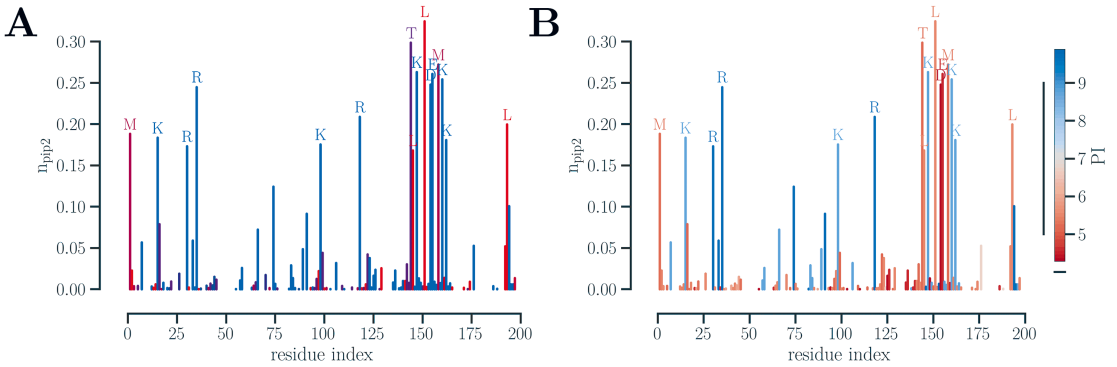

Figure 3.7.: PIP_2-binding residues in F0F1. *A*) The average number of PIP_2 in contact with each F0F1 residue across all time frames following the initial contact calculated from the data set generated by the rotational sampling. The color map represents the most hydrophobic residues in red and the most hydrophilic ones in blue. *B*) As on the left, with residues colored according to their PI in solution.

In the next step, we determined which residues were involved in membrane binding. For this, we considered all trajectories but discarded the frames before the first interaction between protein and membrane. Figure 3.7 highlights which F0F1 residues had the highest propensity to bind PIP_2 with the average number of PIP_2 in contact with the respective residue. For this, all time frames after the initial contact were considered. Consistent with previous data, figure 3.7 shows a large cluster at the F1 loop region. Like one would expect for PIP_2 binding, the residues that were most likely to bind to PIP_2 were the basic residues K and R, which are known PIP_2-binders. [57] In addition to these, we observed a set of rather hydrophilic residues with acidic side chains, as indicated by the low PI (see figure 3.7). T144, for example, interacted frequently with PIP_2 in our simulations and has previously been identified as major phosphorylation site on the talin FERM domain. [133] This poses a possible target for PIP_2-dependent phosphorylation which may have implications for the interaction with transmembrane proteins. [134] The next section will extend the scope to the entire talin FERM domain and its PIP_2 interactions.

3.3.2. F1-loop binding can facilitate strong anchoring of the FERM domain to the membrane

Thus far, the focus was limited to a construct of the F0 and F1 domain, which showed that F1 loop and its flexibility make for a very effective mechanism for the protein to encounter and attach to the membrane. Next, we set out to investigate how the entirety of the talin

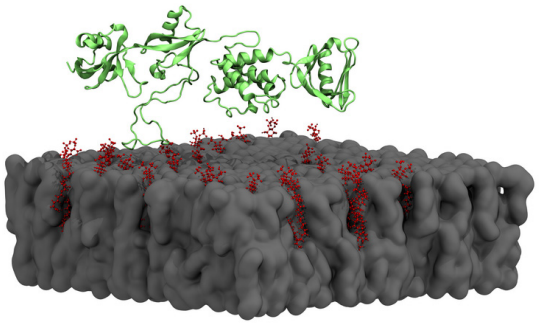

Figure 3.8: The entire talin FERM domain on a PIP_2-rich membrane. The starting conformation for a system intended to study how the FERM (green) domain engages with the membrane (gray surface) containing 10% PIP_2 molecules (red) in the upper leaflet.

FERM interacts with a membrane high in charged phosphoinositides. To answer this, a set of simulations was initiated from a conformation in which the F1 loop is in very close proximity to the membrane. This aims to reproduce a situation in which the loop acts as a first-contact site and allows the study of the dynamics of the FERM domain after this initial contact. The system depicted in figure 3.8 served as the starting conformation for seven independent replicas; each of which was simulated for 400 ns without any bias.

To evaluate the association between protein and membrane, the number of PIP_2 in contact with the FERM residues of the FERM domain over the course of six simulations was calculated with ConAn (see section 2.4.3, [112]) and is depicted in figure 3.9. In accordance with figure 3.4 and like previously defined, contacts were considered if the distance between any two atoms of two residues or molecules was shorter than 0.25 nm. Observe that a total of seven simulations was started but in one simulation no contacts with the membrane were formed. This would result in a plank panel in figure 3.9 and is hence not explicitly shown.

The six simulations that did make contact with the membrane all formed stable interactions with the latter, i.e. there were no occurrences of a bound protein spontaneously detaching from the membrane. At the chosen distance cut-off of 0.25 nm for contacts, the highest recorded number of PIP_2 that interacted simultaneously with one amino acid was two, but predominantly, interactions involved only one residue. As in the F0F1 truncation model, the F1 loop formed extensive interactions with negatively charged phosphoinositides. In addition to the interaction characterized earlier, there were strong interactions formed with the F2 and F3 domain. More specifically, the involved residues were localized between residues 250 and 280 in F2 and residues 320 to 370 in F3. This contrasts to some extent with the findings presented by Chinthalapudi et al. [57], who identified only one major interaction site for PIP_2 when crystallizing the FERM domain of talin with PIP_2 heads by hanging-drop vapor diffusion: K272 in F2, as well as K316, K324, E342, and K343 in F3 all bound to a single PIP_2 head group. Figure 3.10 shows the respective crystal

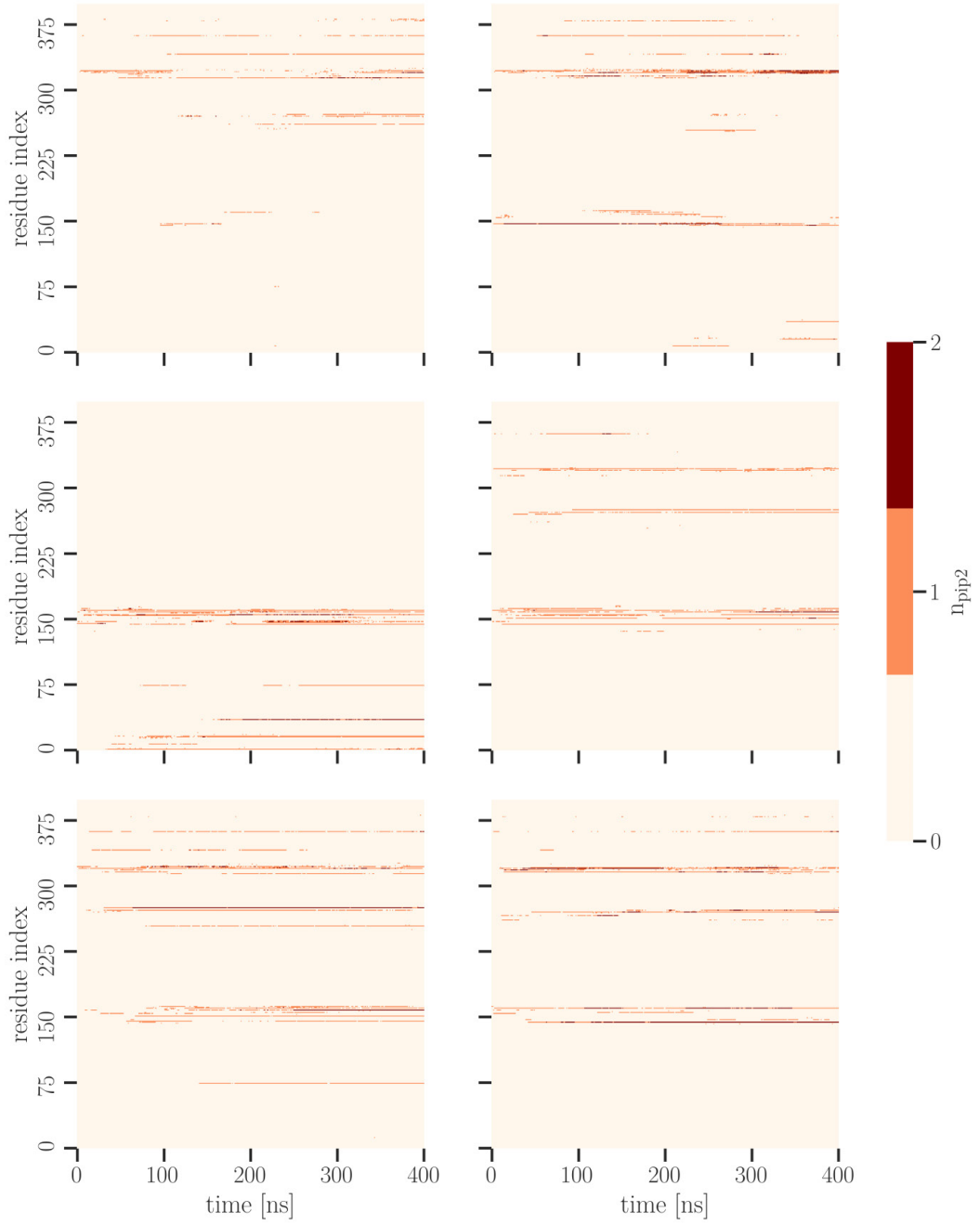

Figure 3.9.: Number of PIP_2 per residue. Every panel represents an individual, independent simulation and shows how many PIP_2 molecules bind to the FERM's residues over the course of the simulations. Of the seven simulations, here, only six are shown, since one did not establish any contacts with the membrane. Contacts between the FERM domain and PIP_2 were tracked with the ConAn-suite (see section 2.4.3, [112]). If the distance between any two atoms of two different molecules falls below 0.25 nm, it is considered a contact. The color code encodes how many PIP_2 are in contact with a given residue at a given time.

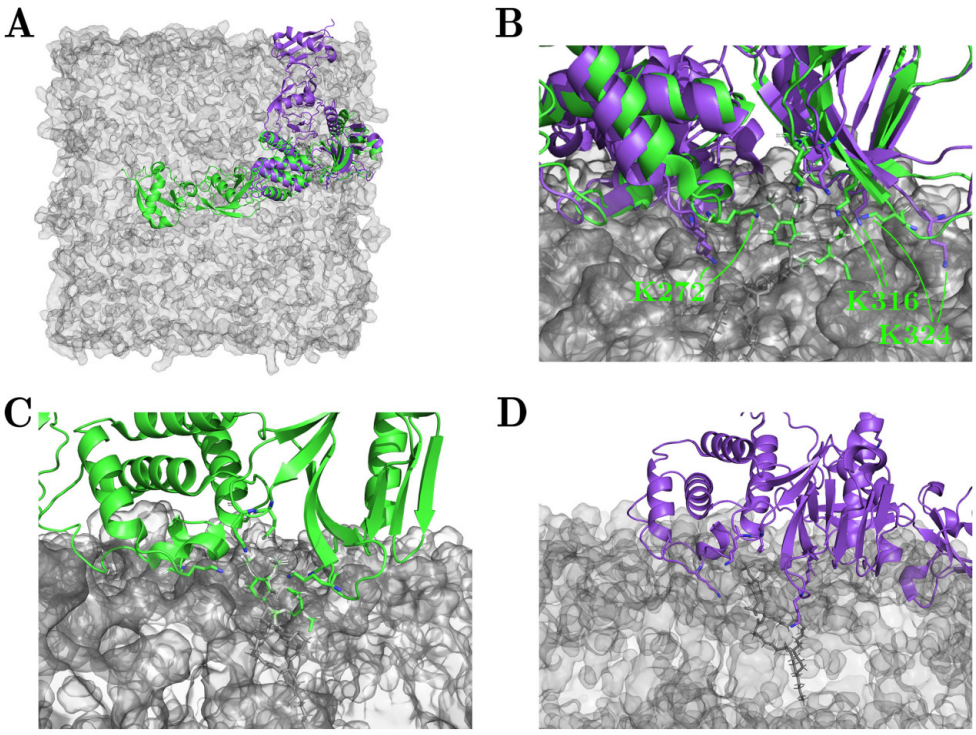

Figure 3.10.: Crystal structures with membrane. *A*) The PIP_2 head included in the crystal structure by Chinthalapudi et al. [57] (pdb-ID 6MFS, green) fitted to a PIP_2 molecule within a membrane. The clover-leaf-like structure (pdb-ID 6VGU, purple) by Zhang et al. [135] was aligned respecting the F2F3 sub domains. *B*) Magnified view of the interaction site and the alignment of the PIP_2 cyclical head. *C,D*) The rod-like and clover-leaf-like shown individually.

structure and an overlay of the crystal-structure PIP_2 head domain (PIP_2diC8) with our PIP_2-containing membrane. The figure also includes an overlay of recently published structure by Zhang et al. [135], which does not include bound PIP_2. When comparing the position of K272 between these two structures (Figure 3.10b) we see that the latter exhibits a much higher distance between K272 and any of the PIP_2 binding residues in F3 (e.g. the distance between K272 and K316 increases from 1.24 nm to 2.07 nm). Another obstacle that arose while matching the crystallized PIP_2diC8 to a full PIP_2 molecule embedded in the equilibrated membrane was the alignment of the crystal contact between K324 and PIP_2diC8 which is not with one of the phosphate groups in the lipid head but with an oxygen located closer to the hydrophobic tail of the lipid. For this, a full alignment involving all crystal positions of PIP_2diC8 would always result in part of the F3 domain overlapping strongly with membrane. Only when restricting the fit to the carbon ring and the phosphor groups, an alignment that respects the integrity of the membrane could be achieved. In the latter case, however, K324 and K316 are no longer in direct

contact to PIP_2 (see figure 3.11b) This poses a very interesting observation that motivates further analysis on the protein-PIP_2 interactions that formed during our simulation. For this, we employed contact analysis (see section 2.4.3, [112]) on our trajectories to find which FERM residues made contact with an individual PIP_2 in order to pinpoint possible PIP_2 binding sites in the presence of a biological membrane.

While the simulations showed all of the residues identified by Chinthalapudi et al. [57] to be frequently involved with PIP_2, we did not reproduce the specific cluster of interactions. Even though we observed a single PIP_2 making contact with up to four and even five talin residues at a time, the simulations failed to reproduce the crystallographically defined combination. Table 3.1 shows the most abundantly occurring interactions between individual PIP_2 and either 1, 2 or more than 2 talin residues at a time (refer to appendix table A.1 for full list of recorded interactions). The data shows that PIP_2 preferably interacted with either (in addition to the loop and the F0F1 domain), a cluster located in the residue-ID range between 250 and 280, or a cluster centered around residue K320 The strong peaks at D341 and S362 (see figure 3.11a) often interact together with the cluster close to K320 for which we included those residues in the F3 cluster used for the analysis presented in figure 3.11. In an extended effort to reproduce the experimental binding site [57], an additional set of simulations was run using the unmodified crystal structure with the PIP_2 head converted into a full lipid within a similar membrane as used in the previous simulations. An identical cluster analysis was performed and the results are summarized in the appendix table A.2. The observed one-to-many interaction confirmed our preceding results, as the specific experimental binding site was already lost during the preceding equilibration simulation and clusters of similar sizes and residue participation as in table 3.1 formed.

The three major PIP_2 binding clusters identified by these simulations are summarized in figure 3.11a. Based on this clustering, the time evolution of the total number of PIP_2 associated with each of the clusters was calculated. Figure 3.11b shows this average over all simulations and to obtain an estimate on how quickly these clusters saturated and with how many PIP_2s they did so, a function of the form $N_c \cdot \left(1 - e^{-\lambda_c t}\right)$, which essentially is a scaled cumulative distribution function (CDF) of an exponential distribution, was fit to the data. The resulting fit parameters for the PIP_2 saturation number N_c and the associated rate constant λ_c are tabulated in table 3.2. The loop and the F3 interaction site, in particular, attained the PIP_2 saturation number significantly faster than the cluster in F2. While this is not surprising for the F1 loop because our initial conformation favored a loop-membrane interaction, F3 appeared to have a higher affinity for PIP_2 than F2.

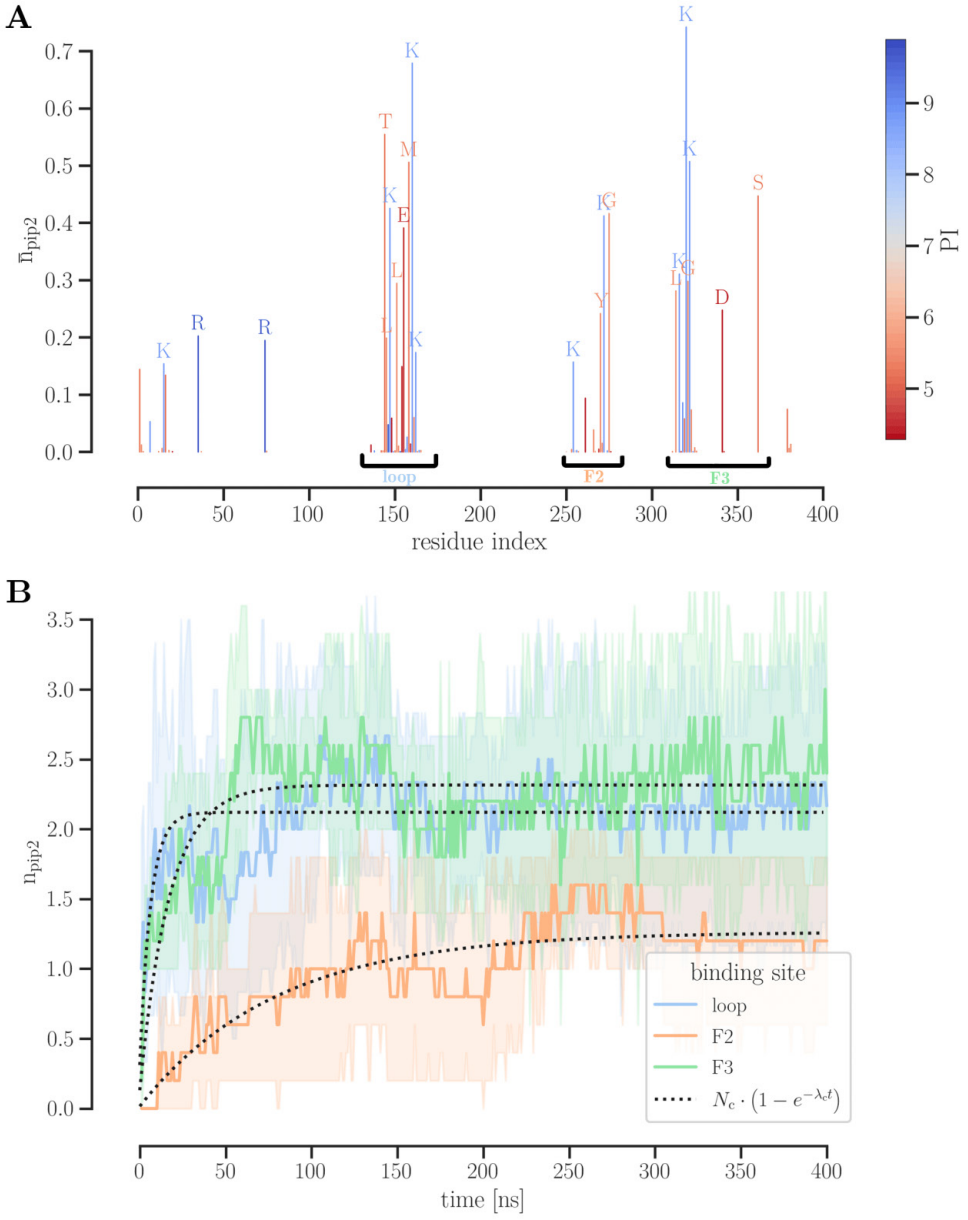

Figure 3.11.: Simulations reveal three PIP$_2$-binding clusters along the FERM domain. *A*) The average number of PIP$_2$ in contact with each FERM domain residue during six 400 ns-long simulations. Residues are colored according to their PI in solution and described by their one-letter amino acid code if $\bar{n}_{\mathrm{pip2}} > 0.15$. *B*) For the three interaction clusters identified (loop, F2, and F3), the number of unique PIP$_2$ is tracked. The number of PIP$_2$ averaged over all simulations $\hat{n}_{\mathrm{pip2}}$ is shown as a solid line; the shaded region represents the standard deviation entailed. For each binding site, the CFD of an exponential distribution scaled by N_c is fit to the curve.

Table 3.1.: One-to-many interactions of PIP_2 molecules with the FERM domain. The most common residues or clusters of residues that were in contact with an individual PIP_2. Counts refers to the number of frames in which these interaction were observed. Here, we considered one frame per nanosecond. A non-truncated list can be found in table A.1.

$n = 1$	**Counts**	$n = 2$	**Counts**	$n \geq 3$	**Counts**
K147	641	G275, K272	586	K160, L151, T144	190
K320	579	K320, K322	493	G321, K316, K320	180
D341	468	K160, T144	331	G321, K320, K322	161
M158	435	G275, K254	292	K15, R35, T16	104
S362	431	K160, M158	278	K147, K15, R35, T16	87
K160	361	L314, S362	270	D261, K272, Y270	82
K322	339	E155, M158	157	K147, K160, T144	81
M1	319	E155, T144	119	K162, L145, L151, R74	75
Y270	311	D154, E155	114	E155, K160, T144	71
R35	243	K162, M158	81	K160, L151, M158, T144	66

Table 3.2.: Fit parameters. The parameters obtained by fitting $N_c \cdot \left(1 - e^{-\lambda_c t}\right)$ to the data presented in figure 3.11. Fitting was carried out using Levenberg-Marquardt algorithm to minimize the sum of the squares of the residuals.

binding site	N_c	**SE**(N_c)	$\lambda_c\,[1/ns]$	**SE**(λ_c)
F1 loop	2.120	0.023	0.159	0.028
F2	1.264	0.029	0.013	0.001
F3	1.814	0.019	0.060	0.006

The computational efforts presented in the following section aim to further quantify the role of PIP_2 in the FERM–membrane interaction. To this end, force-probe MD simulations displacing the protein relative to the membrane were carried out while varying the concentration of PIP_2 within the lipid bilayer.

3.4. High PIP2 concentrations prevent lateral displacement on the membrane

The results presented previously in this chapter, as well as recent experimental findings [42], underline the role of PIP_2 in the talin activation process. Because of the many possible interaction sites for PIP_2 on the FERM domain, one can speculate that the

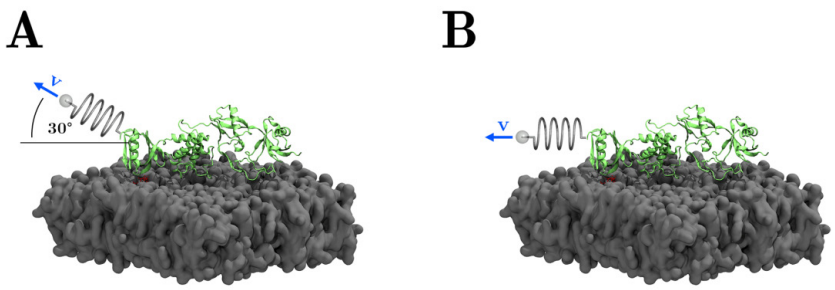

Figure 3.12.: Simulation protocol that drags the talin FERM domain across a membrane. The simulation setup used to investigate the influence of the high PIP_2 concentrations in focal adhesion. We compare between high and low PIP_2 concentration and two directions of force application: *A)* in a 30° angle, and *B)* parallel to the membrane. Ergo, we distinguish between four types of setups.

high PIP_2 concentration has also a part to play in maintaining activated talin proteins at the membrane, i.e. close to their workplace – the focal adhesions. Additionally, talin inevitably experiences mechanical force as it starts to bridge between the ECM and the actin cytoskeleton. [40, 41, 136, 137] These mechanical forces seem to have a large lateral component according to super-resolution imaging of FAs. As elaborated upon in section 1.2, talin lies diagonally in the FA complex. [28, 29] Furthermore, Liu et al. [138] demonstrated that the actin-bound talin forms an acute angle with the membrane. Another possible important role for lateral diffusion can be imagined for PIP_2-activated talin which have not yet engaged with the remainder of the FA machinery. With the rod domain of the protein comprising over 1200 amino acids, intuitively, a strong connection to the membrane to prevent already activated talins from detaching from the membrane too easily and a reduced lateral diffusion could facilitate the binding to further FA proteins.

The hypothesis investigated in this section assumes that the multitude of possible PIP_2 anchorages together with a high local concentration of PIP_2 at nascent FA can provide means to associate the protein to the membrane much stronger than the primary binding site would do on its own. This would support an accumulation of talin in proximity to the focal adhesions, where it can engage in and support FA growth and, hence, force transmission.

As a reference and starting point for the here presented MD simulations, a FERM-membrane 'complex' was used in which PIP_2 from all clusters identified in section 3.3.2 form contacts with the protein. To probe the influence of the PIP_2 concentration, we compared this system and its response to lateral pulling forces to a system with little

(~1%) PIP_2 concentration. To this end, we converted selected PIP_2s into uncharged phosphatidylinositols using an in-house script. The reason for the conversion to uncharged phosphatidylinositols rather than POPC lipids–as found in the remainder of the membrane– was the structural similarity which allowed for a modification of the membrane without the introduction of overlapping molecules while eliminating the charges responsible for the protein-PIP_2 binding. This was realized by substituting the charged phosphate groups on the PIP_2 head by uncharged OH groups. To account for the altered system charge, the script also adapted the topology file by excluding surplus Na^+ ions. Hence, we generated a topology that maintains three of the initial 22 PIP_2 molecules located in the region of the of the earlier defined F3 binding site. Using force-probe MD simulations, we probed whether a high PIP_2 concentration increases friction between membrane and protein and, therefore, the resistance against lateral diffusion. By applying constant velocity pulling to the linker, we mimicked a force originating from the the talin rod.

In terms of pulling direction, we followed two distinct approaches. Pulling was carried out either along a vector that spans a 30° angle with the plasma membrane, or a vector which is parallel to the membrane (see figure 3.12). Solely for the purpose of investigating the lateral drag on the membrane, a pulling vector parallel to the latter seems intuitive and sufficient. However, for a close mimicry of a biological context in which – as described above – talin and the membrane do not lie parallel encompass an acute angle we focused on simulation with a 30° angle. [138] The two pulling directions we followed are presented jointly in the following.

Simulations were run for each, a low and high PIP_2 concentration of ~1% and 10%, respectively (see section 3.2 for specifics); parallel, and with a 30° upward angle; and with pulling speeds of 0.1 m/s and 0.03 m/s. Figure 3.13 compiles the results obtained by the three replicas of force-probe MD that were run for each of the eight combinations. Evidently, the PIP_2 concentration had a significant effect on the forces arising while pulling, most notably for the higher pulling speed of 0.1 m/s. Table 3.3 demonstrates that the mean force during the first phase of the simulation (before the protein detaches or starts unfolding) approximately doubled for higher concentrations with the effect being more pronounced when pulling at an 30° upward angle. This restriction to the first phase of the simulations is necessary, as direction-periodic pulling with an upward angle did eventually lead to the protein unfolding or detaching from the membrane, as the virtual point that connected the virtual spring to the protein increased its distance to the membrane steadily. Nonetheless, a phase of drag was observable before the contact to the PIP_2 molecules and the membranes was lost. Interestingly, a total loss of contact between protein and membrane was only observed for low PIP_2 concentrations. At 10% PIP_2, the

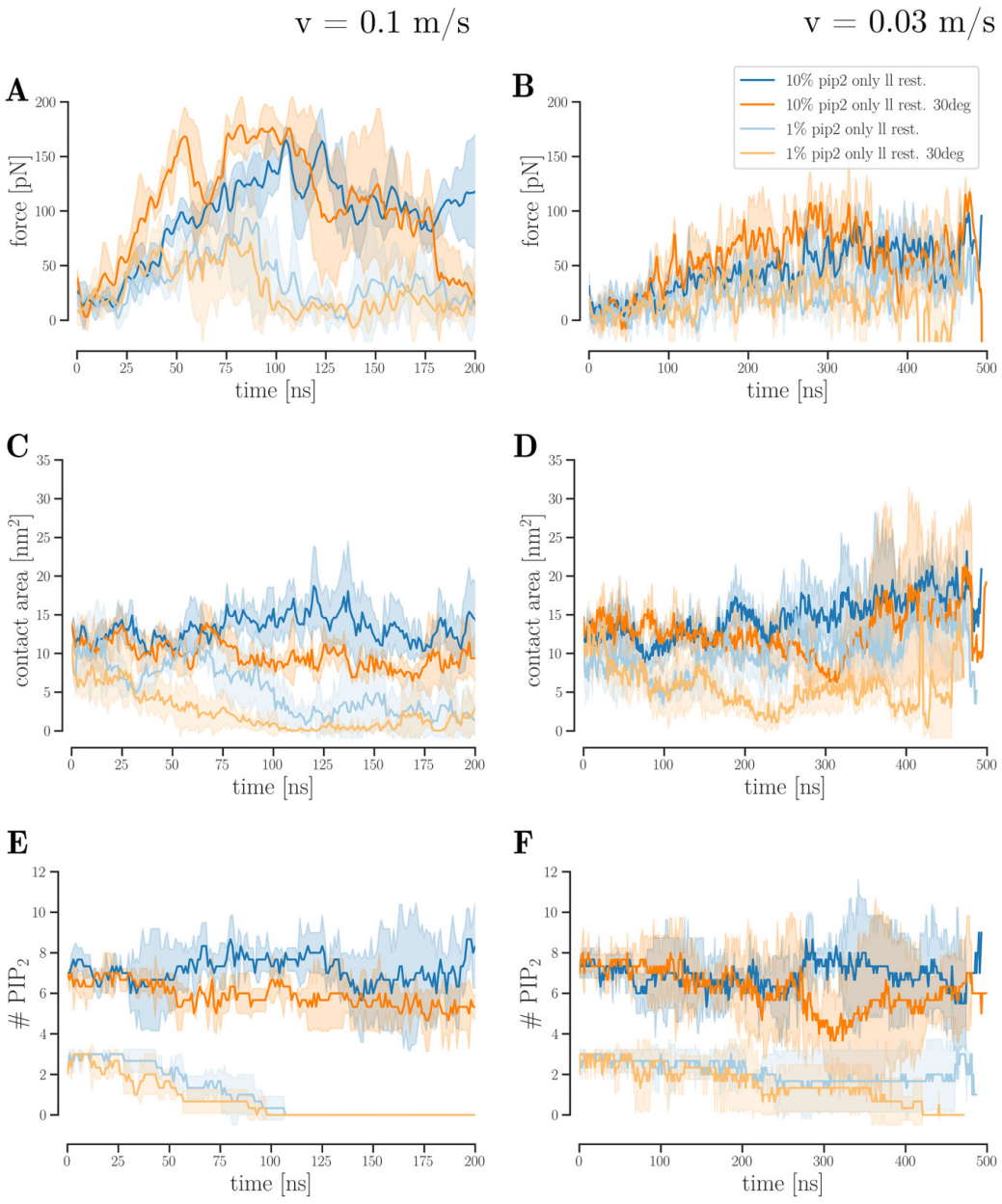

Figure 3.13.: PIP_2 increases the lateral friction between membrane and FERM domain. Analysis of the force-probe MD simulation are presented from pulling speeds 0.1m/s (*left column, A)C)E)*) and 0.03m/s (*right column, B)D)E*). Data from simulations the pulling vector parallel to the membrane are illustrated in blue; data from pulling with a 30° angle with respect to the membrane are shown in orange. Data from high PIP_2 concentration of 10% is shown in dark colors, while the low PIP_2 concentration is depicted with light colors. *A)+B)* The measured forces on the virtual spring with spring constant $500\,\mathrm{kJ\,mol^{-1}\,nm^{-2}}$ between FERM linker and a constantly progressing point. *C)+D)* Contact area between protein and top leaflet of the membrane. *E)+F)* Number of unique PIP_2s interacting with the protein.

contact between protein and membrane was preserved with very small influence of the direction of force application. At ~1% PIP_2 and 30° degree pulling, the protein always detached from the membrane. When the pulling vector was parallel to the membrane, contact was only lost at the higher pulling speed.

Table 3.3.: Forces during lateral pulling. Mean, standard deviation, and maximum of the measured forces during the first 100 ns and 300 ns for pulling with $v = 0.1$ m/s and $v = 0.1$ m/s, respectively.

topology	speed [m/s]	mean [pN]	std [pN]	max [pN]
10% PIP_2	0.10	74.6	42.2	145.9
10% PIP_2 30°		110.0	54.9	178.8
2% PIP_2		45.7	23.3	93.6
2% PIP_2 30°		43.3	19.1	77.3
10% PIP_2	0.03	33.2	16.2	84.3
10% PIP_2 30°		50.9	29.5	107.9
2% PIP_2		17.0	13.2	61.1
2% PIP_2 30°		18.7	14.1	50.1

With the parallel-pulling approach, (see figure 3.12a) an effect at low PIP_2 concentration emerged in which the PIP_2 binding at F3 acted as a pivot point resulting in a lever-like behavior that pushed the F0-F2 domains off the membrane. Figure 3.14 illustrates this effect. In the case of high PIP_2 concentration, the F0F1 domain was bound more strongly to the membrane, which led to a different behavior: the strong anchor between loop and membrane here acted as a pivot point which resulted in the F3 domain being pushed down into the membrane. The effect was not observed in the simulations which feature a 30° angle between membrane and the pulling vector.

At parallel pulling and high PIP_2 concentration, the contact area between membrane and protein slightly increased. This can be attributed to the lever-effect described above, where the F3 domain was effectively pushed down towards the membrane, which, did slightly bend the membrane as a consequence. Note that in all simulations, the x- and y-positions of one head group atom of the POPC lipids in the lower leaflet were restrained. Even though there was no direct restraint on the z-axis, bending was still partly dampened by the x- and y-restraints, as membrane bending generally involves a lateral displacement of lipids as well. Hence, we would expect membrane bending to be more pronounced in unrestrained simulations. The restraints in these simulations were nonetheless necessary as the periodic lateral direction of pulling would simply displace the entire system inhibiting an evaluation of drag against the membrane. The restraints combined with the 30° upward

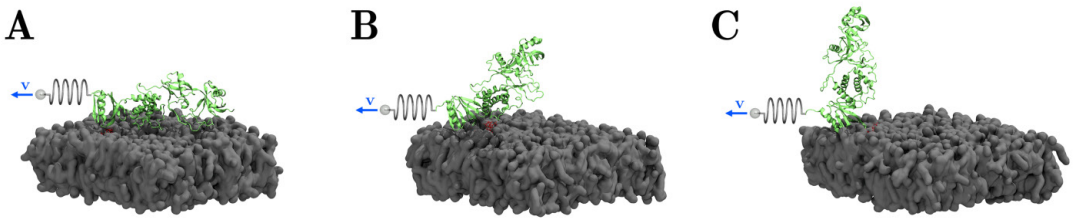

Figure 3.14.: Lever mechanism in parallel pulling. With an external force pulling on the linker located on the top of the F3 domain and the PIP_2 binding site located at the bottom of the F3, a lever-like effect acts towards tilting the F0-F2 domains away from the membrane. A) - C) depict the time progression of the described system with the FERM domain colored green, and a gray surface representation of the membrane. The linker is pulled with constant velocity v as represented by the red arrow. PIP_2s are depicted as red ball-and-stick model.

angle did indeed eliminate any downward pressure on the membrane and generated a nicely observable dragging of the protein over the membrane surface.

The findings presented here suggest an important role of high PIP_2 concentrations and underline the PIP_2 binding-capability of the FERM F1 flexible loop. The strong relative increase in drag-forces during pulling is consistent with the idea of increased friction resulting from additional interaction sites along the FERM domain, whereas an interaction with only the 'primary' binding site [57] is much more receptive to detachment and lateral displacement.

3.5. Discussion

In this chapter we studied the interactions of talin with PIP_2-containing lipid bilayers by means of equilibrium and force-probe MD simulations. We revealed that a highly flexible loop within the F1 subdomain of the talin FERM domain can act as a first contact site of the autohinhibited protein with the cellular membrane. We conducted a rotational sampling that systematically probed different initial orientations of the loop with respect to the membrane. For a 10% PIP_2 concentration and physiological ionic strength of 150 mM, a connection typically forms very rapidly within 200 ns–even at maximal distance between loop and membrane.

Next, we detected that after the loop has made contact, other binding sites follow quickly. The simulated PIP_2-membrane interactions presented here differ from the the PIP_2 binding-site residues suggested by the crystal structure [57] in a notable way. While our

simulations largely reproduced the key PIP_2-binding residues observed experimentally, we distinguished two interdependent binding sites, one in F3 and one in F2, instead of one single binding site involving residues from both subdomains. We conclude that the the two-dimensional membrane forces talin to locally adopt and open its F2-F3 interface and thereby impedes the concurrent PIP_2-interactions of the two subdomains observed in the PIP_2-talin crystal structure, in which such a constraint in form of a flat membrane is absent. The analysis further suggests that the residues in F3 represent the more important PIP_2 binding site (see figure 3.11).

The fact that *in silico* data shows that the F1 loop forms a strong first connection upon which further interaction follows, constitutes an interesting finding in the light of talin activation. We suggest that the loop-PIP_2 interaction is able to keep talin in sufficient proximity to the PIP_2-enriched membrane, increasing the probability for F2 and F3 to forego the autoinhibitory link to R9 and R12 and bind to PIP_2. While this hypothesis would benefit from truncation or mutation studies, it is very well consistent with recent finding by [42], who suggest that a PIP_2 containing membrane is indeed able to promote talin activation.

Rossier et al. [139] combined single-protein tracking with super-resolution imaging to probe the dynamic organization of talin in FAs and concluded that after talin is recruited directly to the FAs from the cytosol and free diffusion in the plane of membrane is impeded. Furthermore, β3-integrins experience a similar restriction in diffusion when bound to talin. While the origin of such diffusional barriers remains poorly studied to date, our *in silico* experiments show that extensive interaction between PIP_2 and all talin FERM subdomains harbours the potential to fixate the protein to regions with high PIP_2 concentration. This means, the effect of the high PIP_2 concentration is two-fold. On the one hand it activates talin and on the other hand restrains it to the area of the FA.

Future work could comprise simulations of a larger part of the entire talin protein including the FERM domain and the rod domain, or the subdomains in contact with FERM domain in the autoinhibited talin conformation. This could help to better understand to what extend the autoinhibition can indeed be relieved by PIP_2. Our finding in context with the result of recently published experiments do already point in this direction. [42] Nonetheless, directly testing the molecular underlyings of talin activation remain an interesting topic for further investigation.

Taken together, this chapter of the thesis strongly suggests that membrane binding that involves PIP_2 is sufficient to relieve the autoinhibited talin conformation. Dedden et al. [56] and Kelley et al. [42] proposed further that the interaction with a PIP_2-containing

membrane also suffices to reveal at least on vinculin binding site – potentially by causing secondary structural rearrangements within the rod domain. The exposure of vinculin binding sites promotes the association of vinculin to the focal adhesion complex. In the following chapters, our focus will shift towards the investigation of the force-dependent interplay between talin and vinculin.

4

Force-dependence of talin-vinculin association

4.1. Introduction

The mechanosensitive talin rod responds to force by forming a complex network of connections with its molecular partners, whose recruitment is strongly dependent on the intensity of the mechanical cue on talin. With a total count of eleven vinculin binding sites (VBS), vinculin is talin's most important associate. [43] In general, VBS are six-turn amphipathic α-helices (approx. 22 residues) contained within four or five helix bundles in the talin rod domain. These helix bundles are typically held together by strong hydrophobic interactions, [58] and the exposure of VBS usually requires mechanical unfolding. Once exposed and under force, vinculin binds to talin, [59] which in turn leads to the recruitment of further F-actin filaments. As a consequence, the mechanical coupling and strength of the focal adhesion is increased. [140] This coupling is illustrated by figure 1.2 in the introduction chapter.

The talin rod is made up of 13 helical bundle domains, and VBS1 is contained in the first bundle (R1, see figure 1.2 and figure 4.1). The interesting characteristic of VBS1 is that it forms a particularly strong interaction with vinculin in binding essays. [58] VBS33 also forms a strong bond with vinculin; located in R7, its intermolecular interactions with vinculin are stronger than the intramolecular ones it exhibits when bound within the intact rod domain helix bundle. [141] In contrast the VBS36-vinculin bond is on the weaker side of the VBS-spectrum. [58] Nonetheless, VBS36 is interesting because of its location in the R8 domain of talin; R8, which also has a paxillin binding site, is not found between R7 and R9, like one would expect, but rather as an extrusion of the R7 domain. Consequently, the R7 domain must, at least partly, lose its integrity before R8 may be unfolded by any force across the talin backbone. An overarching scheme found all of the talin VBS are hydrophobic residues at positions 4,5,11,15,18, and 19 as denoted in figure 4.1. These residues are usually found deep inside the core of the talin rod helix bundles and are responsible for the strong interactions with vinculin when attached to it.

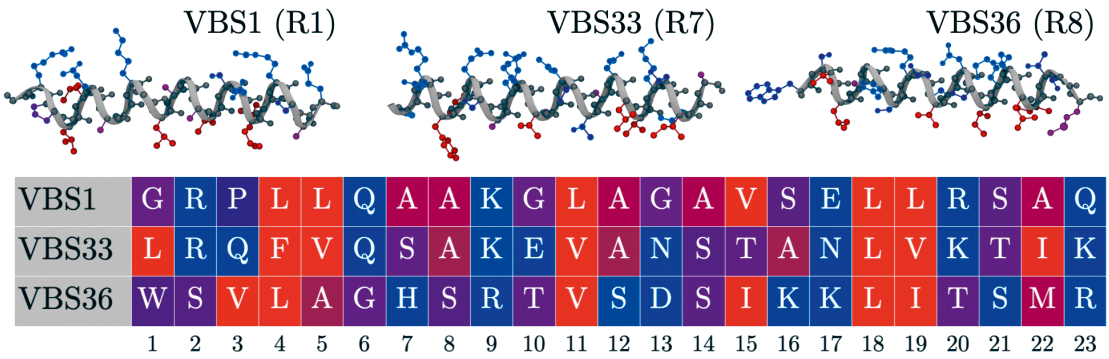

Figure 4.1.: Structure and sequence alignment of the investigated VBS. (*Top*) The structures shown here, are taken directly from the respective crystal structures (pdb-IDs: 1T01 (VBS1), 3S90 (VBS33), and 1ZW3 (VBS36)), hiding the attached vinculin D1 domain. The most hydrophilic sidechains are colored blue, and the most hydrophobic ones are colored red. (*Bottom*) Sequence alignment of the three investigated VBS, as obtained by Clustal Omega [142]. The Coloring encodes the sidechain hydrophobicity as above.

Previous results [59] obtained by our collaboration partner on this project Dr. Rafael Tapia-Rojo demonstrated VBS containing R3 talin construct binds to vinculin when subjected to a small constant force in experiments with magnetic tweezers. [59] The talin helix bundle unfolds and refolds dynamically prior to a binding event. A decrease in the end-to-end distance at the time of vinculin binding suggests that the unfolded VBS has contracted into a single helix. Once bound, much larger forces are necessary to reverse the process in which the helix unfurls again and vinculin dissociates. This is remarkable since

the process by which VBS bind to vinculin and convert the vinculin D1-domain 4-helix bundle into a 5-helix bundle has previously been unknown. Nonetheless, the molecular picture of the force-dependent dynamics of the many VBS along the talin rod, as well as the molecular mechanism by which a coil-to-helix transition can occur remain elusive.

In this chapter, we study the dynamics and kinetics of VBS-vinculin unbinding by means of constant-force MD simulations. We compare three different VBS – depicted in figure 4.1 – and our data brings to light remarkable dissimilarities in the complex' resistance to mechanical force across the different VBS. The presented results help to understand previously observed kinetics in magnetic tweezers experiments. [59] Also, we find the vinculin head domain to weaken VBS binding if the latter stands under force, a feature that was confirmed by magnetic tweezers experiments (Tapia-Rojo, unpublished). We further demonstrate that the coil-to-helix transition also poses a pathway for talin to bind full length vinculin.

We further investigate the dynamic coexistence of helical and coiled conformations in VBS1 under varying tension, providing a better understanding for the force-dependent molecular recognition of talin by vinculin. Interestingly, at a force of $\sim$10 pN, the end-to-end distance follows a bi-modal distribution and the peptide retains a residual alpha-helix propensity up to $\sim$10 pN. Higher forces cause uncoiling and stretching of the peptide. These findings shed light on how tiny variations in force across talin can influence the probability of vinculin-talin binding.

4.2. Methods

4.2.1. Simulation and experimental details

The GROMACS [110] version 2020.3 was used for all simulations discussed in this chapter. Here, we made use of strong GPU acceleration by running PME calculations on the graphics unit. The AMBER-ff99sb-ILDN force field with Joung ions, [62, 143] and the Tip3p (and Tip4p in one case which is explicitly marked) water model were utilized. The simulation procedure was started with the VBS-D1 complexes structures with pdb-IDs 1T01 (VBS1) [144], 3S90 (VBS33) [141], and 1ZW3 (VBS36) [58]. Because of the use of hydrogen virtual sites (v-sites) in the main set of simulations, the integration time step could be increased to 5 fs. [145] In the case of individual peptides, additional validation simulations were carried out, which use explicit hydrogens and fall back to a 2 fs time step. An NPT ensemble was kept at 300 K using the v-rescale thermostat [72] and pressure was controlled at 1 atm using the Parrinello-Rahman barostat [70] with a τ_p of 2.0. Prior

to production runs, simulations containing the complex of VBS and vinculin head were each equilibrated for 100 ns, whereas the VBS peptides in isolation were only exposed to a 15 ps NVT and a 100 ps NPT equilibration, since the helical structure was lost quickly under equilibrium conditions. For the production runs, we used distance-pulling along the x-axis applying a constant force to the N-terminal and C-terminal C-α atoms of the respective vinculin binding site. For the single peptide simulations, we conducted 3x3x1 µs-long runs for 10 forces between 0 and 20 pN, i.e. three replicas for every force and every topology (Tip3p+v-sites, Tip3p, Tip4p). For the VBS-vinculin-head complex we simulated 20x1 µs-long runs for 4 different forces and each complex type. In case of the full length vinculin complex, 20x50 ns were simulated for 5 different forces.

Magnetic tweezers experiments (of figure 4.8c) were carried out by Dr. Rafael Tapia-Rojo of King's College London to probe the force-dependence of the vinculin-talin complex. A brief overview on the specifics of the magnetic tweezers method can be found in the methods section 2.3. The (talin-R3)-(titin-I91)$_8$ – as used in the previous study [59] – was subjected to a constant force while the z-position of the bead indicates the current extension of the R3 domain (refer to figure 2.7). In the fluid cell, either full-length vinculin or the D1 domain were available for association to the tensed talin domain. Samples of the full-length vinculin were provided by the Geiger lab (Weizmann Institute of Science, Israel) and the Medalia lab (University of Zürich).

4.2.2. Analysis details

We quantified the dwell periods between transitions in each trajectory to compare the helix unfolding duration across the three distinct VBS. For each transition, we created a cumulative distribution function (CDF) by grouping the dwell periods by force, transition state, and topology. Within each of the groups, the smallest occurrence was subtracted from all dwell times. This permitted, assuming a constant rate of failure over time, the use of the CDF of an exponential distribution to fit the cumulative distribution of dwell periods; $N * (1 - e^{-(x/\tau)})$, where N is the number of replicas for a given force. Using ConAn (see section 2.4.3), we initially identified the native contacts from each of the crystal structures before analyzing how the amount of native contacts changed during the course of pulling simulations. Here, the cut-off that defines a contact was set to 0.35 nm and contacts were calculated every 1 ns. The DSSP secondary structure identification method was used to analyze the number of residues in helical or coiled conformation. [146]

In constant force experiments, as the name suggests, the applied force does not change over time (see section 2.2.1). This implies that the magnitude of applied force must be adequate for the investigated system. Generally, the objective is to overcome a certain energy barrier by biasing the simulation in a certain way. If the applied bias is small, the expected time necessary to overcome the energy barrier increases. As this relationship is of exponential nature, sufficient sampling can be infeasible for computationally expensive simulations. On the other extreme, too large forces will result in a deterministic outcome which would impede a stochastic analysis. [99]

In a first effort, we set out to find an appropriate range of forces to study the dynamics of the three selected VBS. For VBS1, VBS33, and VBS36 (pdb-IDs 1T01, 3S90, and 1ZW3, all in complex with the vinculin D1 domain) we carried out simulations following the protocol illustrated in figure 4.2. The C- and N-terminal C-α atoms of the helical peptide were driven apart by a constant force, which we vary between 100 N and 260 N. This 'force sweep' allowed us to select a range of forces in which unfolding of the peptide reliably occurred on a timescale of a few hundred nanoseconds. Figure 4.3 compiles the time evolution of the end-to-end distances of these preliminary simulations where the three VBS peptides exhibited no, partial, or complete helix unfolding and straightening within 1 µs and our force range.

Note, that even though D1 remained attached to the stretched VBS in all simulations, complete unfolding can be regarded a prerequisite for dissociation since VBS must be helical for stable vinculin binding. [44, 58, 59, 141] If a complete dissociation shall be

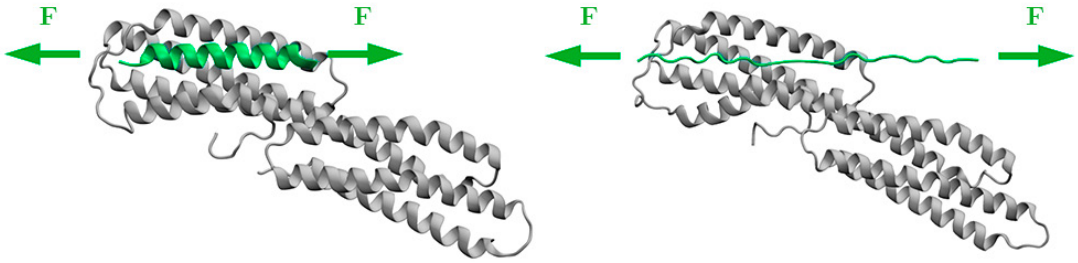

Figure 4.2.: The VBS in complex with vinculin D1 is subjected to a constant force. The simulations are intended to mimic mechanical signals sent along the talin backbone. The N-terminal and C-terminal Cα atoms of the vinculin binding site (green) were subjected to a constant forces acting opposing directions. The D1 domain is colored gray.

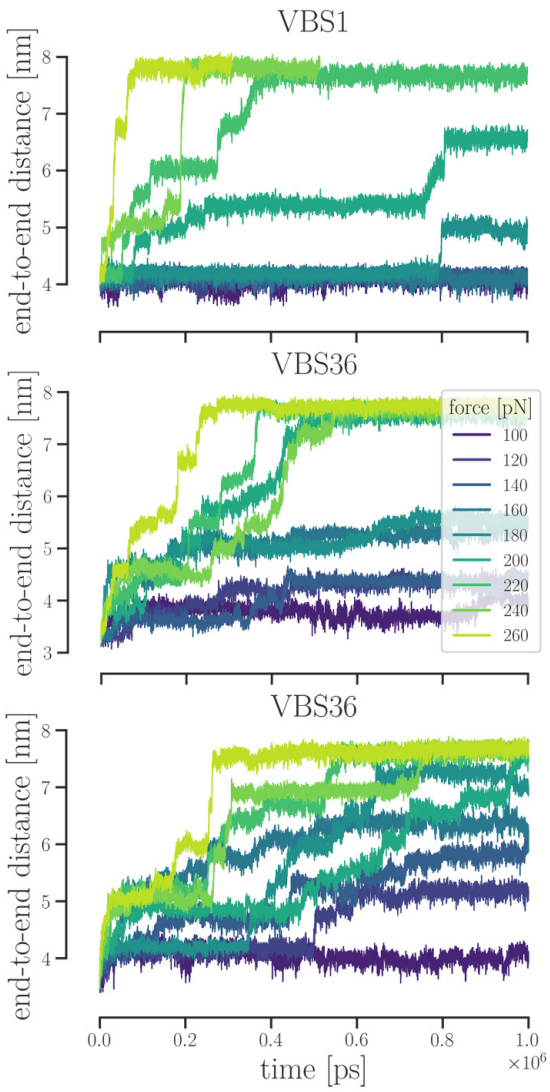

Figure 4.3.: Force sweep indicates differences in the stability against forced unfolding for the VBS helices bound to vinculin D1. End-to-end distance traces for the tensed VBS peptides for forces between 100 and 260pN for VBS 1, 33 and 36. The color legend in the centre plot applies to all panels.

observed, yet longer simulation times, or even an additional bias would be necessary. The VBS1 peptide led to many trajectories that do not exhibit unfolding, in fact, only forces greater than 160 pN led to an increase in the extension of this molecule during the 1 µs-long simulations. Conversely, the VBS33 and VBS36 molecules started to unfold at forces as low as 120 pN, albeit with higher forces necessary full unfolding within 1 µs. Ergo, on a qualitative level, the data suggests that VBS1 is more resistant to force-induced unfolding (and hence dissociation) than VBS33 and 36.

For the subsequent simulations, the pulling forces were narrowed down to 200 to 260 pN for VBS1 and to 180 to 240 pN for the other VBS. With now four forces per peptide and 20 replicas per force, we were able to record a sufficient amount of events to quantify the unfolding kinetics of these vinculin binders. As evident from figure 4.3, unfurling of the VBS helices happened step-wise where the steps spanned distances between 0.5 and 1 nm. With the large sampling achieved for the narrowed force range, the distribution of end-to-end distances permitted an identification of possible large energy barriers between the aforementioned steps. Figure 4.4 shows that for all VBS, three areas along the reaction coordinate exist which exhibited a very low observation-count of end-to-end distances.

The fast passage through these areas speaks for larger energy barriers and allowed us to identify two intermediates (I1, I2) that were populated during force-induced unfolding. The approximate locations of the transition states were determined by finding local minima in the distribution and are marked by black horizontal lines in figure 4.4. The intermediates were conserved for VBS33 and VBS36, albeit with lesser clarity and subtle differences, and thus appear to be robust with respect to the variations in sequence.

When the end-to-end distance of the identified energy barriers, as shown in figure figure 4.4, is crossed for the first time in a trajectory, we call it a passage. Here, we refer to the time that elapsed between two passages as dwell time. We quantified these dwell times between transitions for each trajectory to compare helix unfolding timescales across the three VBS.

Following the procedure explained in section 4.2.2, the CDF of an exponential distribution was fit to the shifted cumulative dwell times; figure 4.5 shows the results for this analysis of the VBS1 trajectories, the data for VBS33 and VBS can be found in figure A.2. This approach comes with the advantage of being robust with respect to fact that not all trajectories attained the fully unfolded state during the 1 µs-long simulations. This means, the method did not require

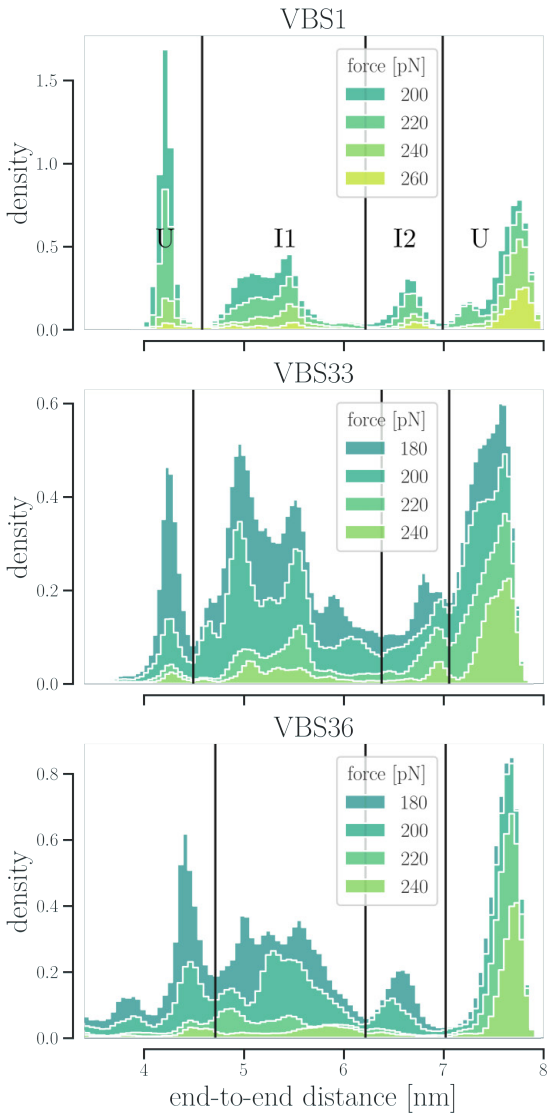

Figure 4.4.: Different VBS have varying levels of resistance to mechanical unfolding. Over 20 1 µs-long simulations, the distribution of end-to-end distances was recorded. For each individual force, the stacked histogram is normalized to 1. The locations of the main barriers along the reaction coordinate, identified by a low density of end-to-end distance measurements at that distance, are indicated by the black horizontal lines.

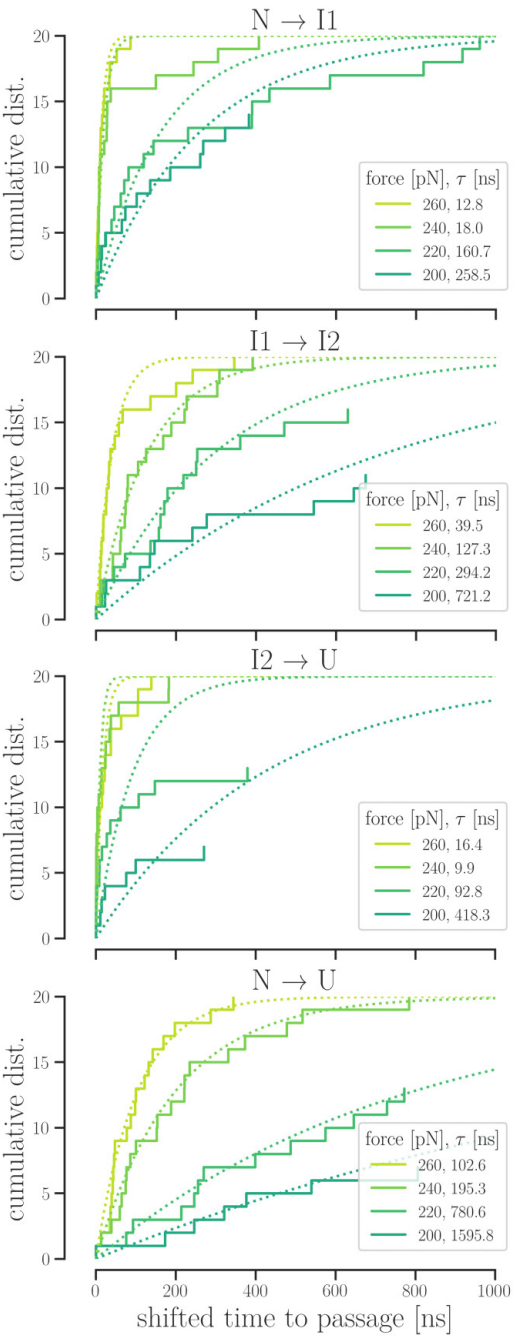

Figure 4.5.: The two intermediates are separated by the highest energy barrier. Cumulative distribution of shifted dwell times for VBS1 unfolding. Data was fit to $N * (1 - e^{-(x/\tau)})$ which is depicted as dotted lines.

all trajectories to reach the fully unfolded state as, for example, was the case for many trajectories between 200 and 220 pN. The smaller amount of data points did however decrease the accuracy of the fit.

The fitting procedure yields an estimate τ for the expected dwell time at a given force, which can be used to compare the mechanical stabilities of the vinculin-bound VBS helices. Figure 4.6 illustrates the force-dependence of the fitted dwell times for the transitions from N to I1, from I1 to I2, as well as for the complete unfolding, N to U. As expected, higher forces led to smaller dwell times, except for VBS33 and VBS36, where the data point for 240 pN lay higher than the one at 220 pN, especially for the middle passage. However, for VBS33 and 36 and the forces of 200 and 220 pN, there were only 10 trajectories available for which the errors here were likely underestimated. For complete unfolding, the data confirmed the intuition gained from figure 4.3, where VBS1 offered the most resistance to unfolding, with τ being almost everywhere higher than for VBS33 and 36. Generally, the transition from I1 to I2 posed the most arduous barrier to overcome, with crossing times up to ten times longer than for the first transition. Also in the second transition on the path to unfolding, the resistance of VBS1 was higher than for the other VBS (except for 240 pN), yet the differences here were not as pronounced. Taken together, VBS1 locked into the vinculin head more tightly than VBS33 or VBS36.

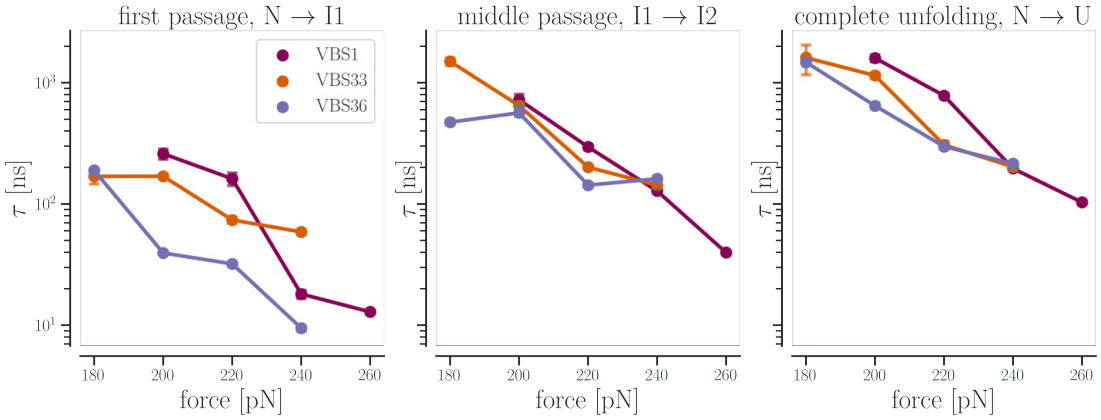

Figure 4.6.: The resistance to mechanical unfolding varies across different VBS. For the first (N → I1), second (I1 → I2), and entire unfolding transition (N → U), the expected dwell time (time to passage) was plotted versus pulling force. The error bars represent the curve fitting error estimates.

To further quantify the subtle differences so far observed in the mechanical response across different VBS, we set out to examine the mechanism of VBS unbinding by analysing the contacts in the VBS-vinculin interface. More specifically, we monitored the contacts of five VBS residues during the pulling simulations and computed the percentage of remaining native contacts, i.e. the contacts with vinculin D1 which were present before application of an external force, over the course of unfolding. As elaborated in section 4.1, there are six positions occupied with hydrophobic residues which are common among all VBS. [58] Two groups of two are in direct proximity for which we selected only one of each group and additionally considered a hydrophobic residue at position 22 (Figure 4.1). This selection of five residues is evenly spread across the sequence and well suited for the study of VBS-vinculin binding or unbinding. Figure 4.7 displays the percentage of native connections in relation to the end-to-end distance of the VBS peptides. Evidently, the first transition from U to I1 involved a loss of contacts around position 22, indicating that helix unfolding starts from the C-terminal end in all cases. If integrated in the talin domain this would correspond to an unfolding starting on the side of the rod domain. For all investigated VBS, the six important and conserved hydrophobic residues [58] remained in contact with the protein when in state I1. The end-to-end distance observation counts histograms shown in figure 4.4 indicated that I1 (more precisely: the transition from I1 to I2) encompassed a wide range of end-to-end distances including several smaller steps. However, there was no distinct separation between the resulting peaks, advocating that I1 reflects a larger ensemble whose conformations share a similar central core that preserves its helicity, rather than one discrete intermediate that results from the unfolding of one

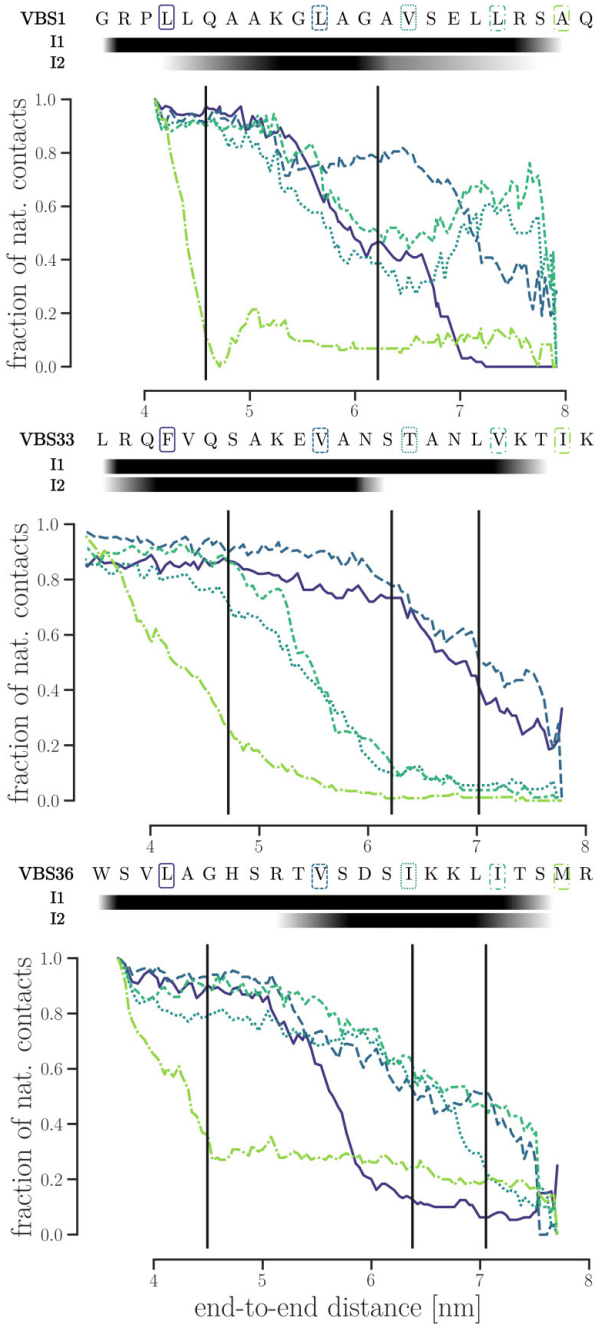

Figure 4.7.: The VBS show the strongest dissimilarities in the second intermediate I2. For five critical, hydrophobic binding residues (compare figure 4.1), the fraction of native VBS-D1 interactions as a function of end-to-end distance is shown. On top of each plot, the sequence of the respective VBS is shown and the binding residues are highlighted according to their appearance in the plot. The bars aim to illustrate which parts of the helices remain intact at the intermediates (compare figure 4.4 for their definitions).

or multiple defined helix turns. Unfolding VBS1 further from I1, Leu4 and Leu19 as well as Val15 lost contact when transitioning to I2. Accordingly, the transition from I1 to I2 involved unfolding of the peptide from both sides. This is particularly interesting in relation to the other VBS; VBS33 only lost contacts from the C-terminal side on its way to I2, whereas VBS33 continued unfolding from the N-terminal end. As the passage from I1 to I2 led to the slowest time constants and, hence, was rate limiting, we concluded that the arrangement of the previously identified six VBS-classifying residues interact strongly as a collective across all VBS.

4.4. Full-length vinculin

Extending the scope of our study, we sought to determine how vinculin and its activation state further regulate VBS unfolding and dissociation. Our previous simulations focused on the vinculin D1 domain, which can be thought of as the vinculin active state, as the vinculin tail domain is not in proximity. Crystallographic studies suggest that talin binding to vinculin leads to decreased contact strength between the D1 and tail domains of vinculin, which in turn, helps vinculin activation. [44] Naturally, the question arises whether the presence of vinculin tail does also have an impact on the binding strength of VBS. To corroborate this, we ran further simulations of a complex including VBS1 coupled to full-length vinculin, based on the pdb structure 1TR2. The structure of the complex was generated by a protocol described in section 5.2.1. The simulation protocol is depicted in figure 4.9a. A set of individual simulations for forces between 100 and 260 pN was conducted for 1 µs each in a force scan comparable to the the procedure carried out for the VBS–vinculin-head complexes. Figure 4.9 shows the force-scan data and suggests that when VBS1 is bound to full-length vinculin, an end-to-end distance of over 5 nm was reached much more frequently and at lower forces compared to the D1 domain alone (see figure 4.9b). To quantify this finding, we performed a large number of short simulations using the full-length vinculin-VBS1 compound, stretching the VBS peptide with forces ranging from 180 to 260 pN. In order to achieve a statistical evaluation of the first transition while keeping the computational cost manageable, 20 replicas with a duration of 50 ns for each force were simulated. The analysis presented in figure 4.9c revealed that transitioning from merely the vinculin D1 domain to the full-length protein had a substantial influence on the first passage from U to I1, speeding up the time to failure by 5 to 10 times and resulting in even smaller dwell times than observed for VBS33 and 36.

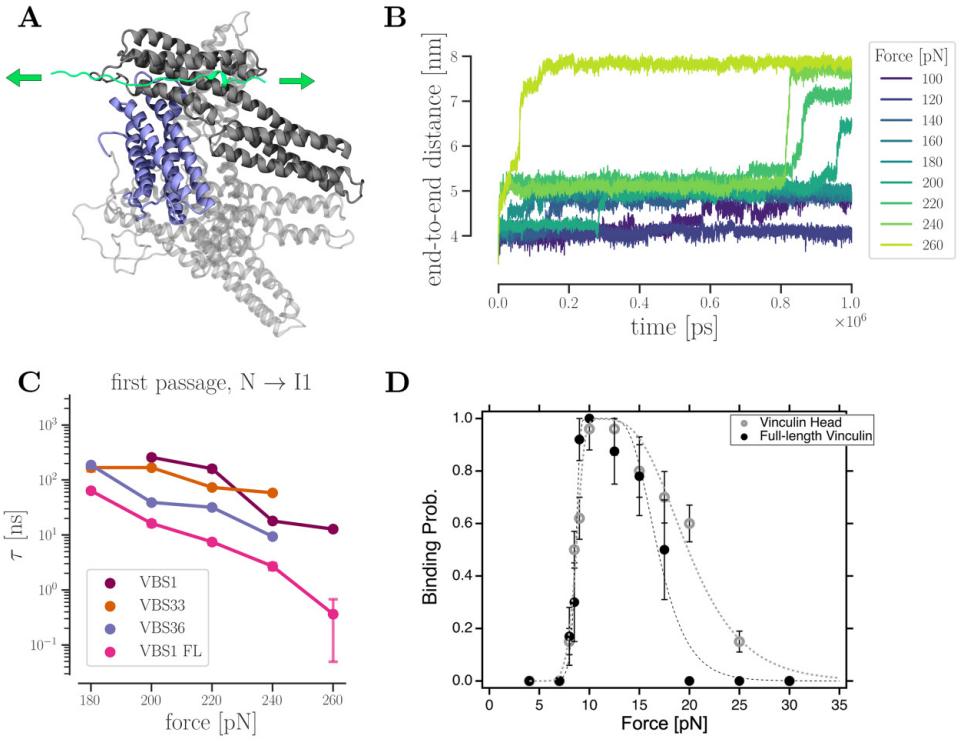

Figure 4.8.: VBS-vinculin binding is weakened by the presence of the vinculin tail domain. *A)* The VBS1-complex employed in this study was based on the full-length vinculin structure (pdb-ID 1TR2) with the VBS shown in green cartoon representation, the vinculin D1 domain in grey, the vinculin tail domain in purple, and the remainder of the vinculin protein in transparent purple. *B)* Force scan: end-to-end distance traces for 9 1 µs-long simulations with forces between 100 and 260 pN. *C)* Expected dwell time before the first transition (N → I1) as depicted in figure 4.6, but extended by the data gathered for full-length vinculin. *D)* Figure and experiments were provided by the collaborator Dr. Rafael Tapia-Rojo (King's College London). In magnetic tweezers experiments the probability of full length vinculin or the vinculin head (D1-domain) binding to a talin R3 domain under force was evaluated with respect to the magnitude of the force across talin R3.

Interestingly, Tapia-Rojo et al. [59] observed a coil-to-helix transition in talin when the vinculin D1 domain binds to it. Motivated by our intriguing results (Figure 4.8a-c), Dr. Rafael Tapia-Rojo used the magnetic tweezers method [59, 103] on full-length vinculin and examined the force-dependence of the binding probability between talin and vinculin. For the D1 domain, the binding probability was characterized by a sharp activation at ~8 pN and a fading probability between 15 and 25 pN (Figure 4.8d). Strikingly, full-length vinculin also bound to the tensed talin construct. Here, the window of high binding probability was narrowed significantly. While the threshold for binding onset remained at ~8 pN, the probability declined dramatically at higher forces, dropping to 0 at 20 pN.

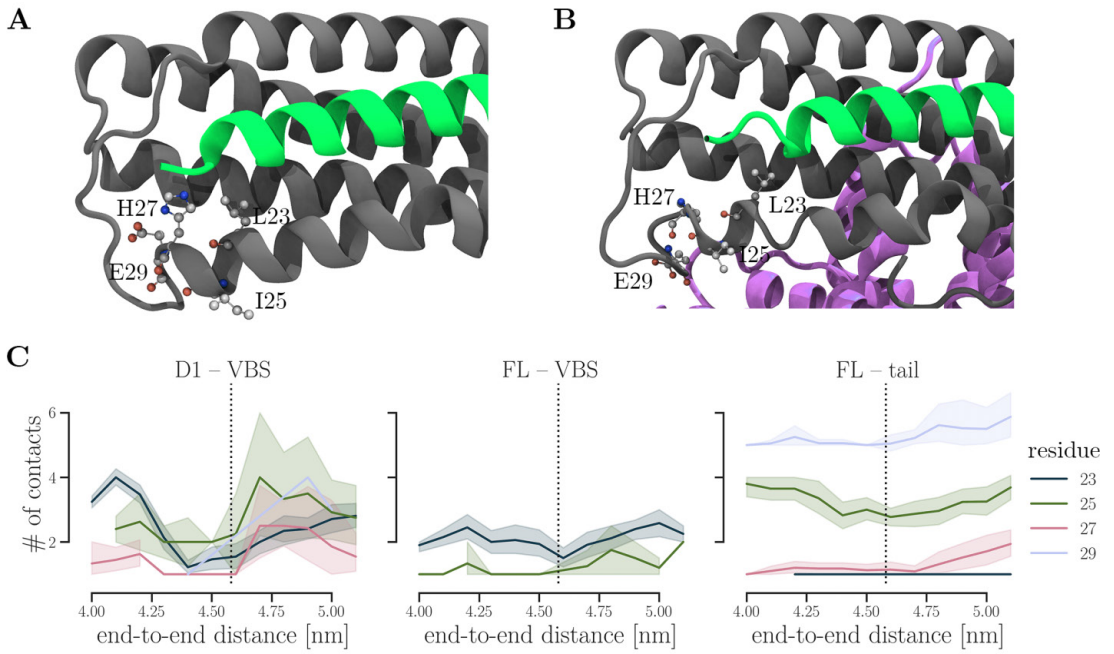

Figure 4.9.: The vinculin tail and talin VBS compete for the attention of D1. *A)* Cartoon representation of the vinculin D1 domain (grey) - VBS1 (green) interaction. Residue L23 and H27 reinforce the complex. *B)* With full-length vinculin, L25 and E27 orient towards the vinculin tail (purple). *C)* The evolution of selected interresidue contacts with respect to the VBS end-to-end distance. *Left*) D1 residues in contact with VBS for the D1-VBS1 complex. *Center*) Residues in contact with VBS when simulating the full length vinculin complex. *Right*) The number of contacts between D1 and the tail domain. The solid lines show the average obtained from up to 60 simulations, the shaded area represents the standard deviation.

To elucidate what molecular mechanism underlies the influence of the vinculin tail domain on the binding strength of the VBS peptide, we used a combination of contact analysis and visual trajectory inspection. Note that VBS and vinculin tail bind on opposing sides of the D1 domain. Since we already established the particular acceleration of the first transition (U $\rightarrow$ I1), the run time of 50 ns of the full-length vinculin simulations is sufficient for an analysis focused on the the parts of the protein involved in that first passage. We performed a visual screening and a contact analysis on the trajectories which revealed that the residues L23, I25, H27, and E29 were specifically influenced by the presence of the vinculin tail (compare figure 4.9a-b). Most notably, H27 turned away from VBS and oriented more towards the tail domain. Furthermore, contacts between VBS and H27 E29 were lost completely when going from the D1 domain to the full-length protein (see figure 4.9c, left and center panel). Instead, I25 and E29 formed a high number of contacts the vinculin tail (see figure 4.9c, right panel). Once VBS1

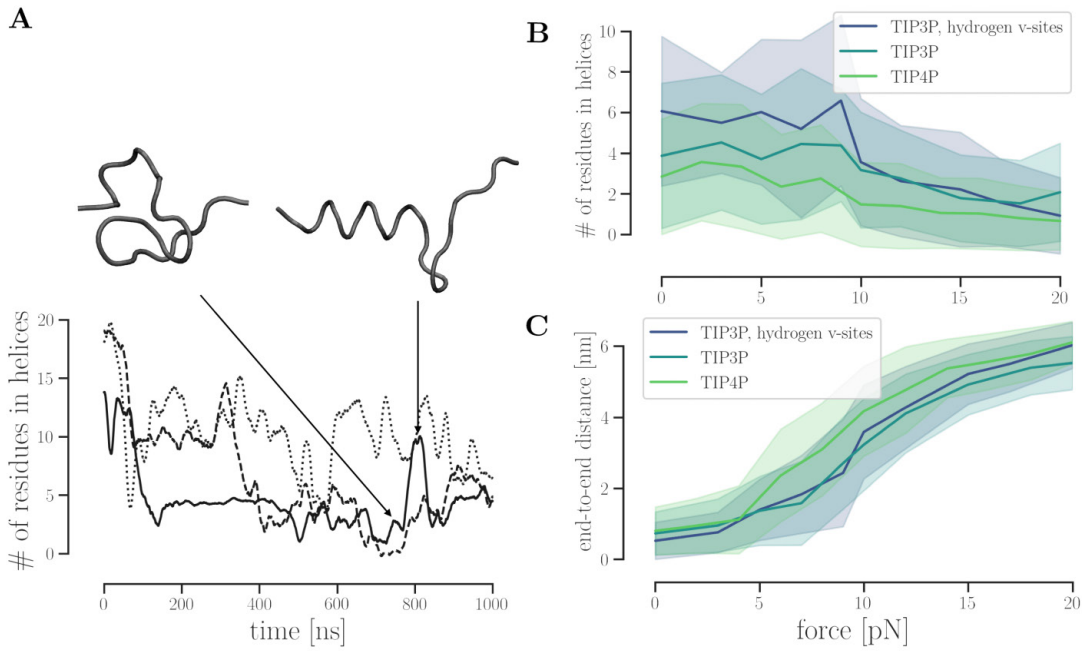

Figure 4.10.: Dynamic coexistence between coiled and helical state at low forces. *A)* Residues partaking in helical structures shown for three example runs conducted with Tip3p water and hydrogen v-sites at 9 pN. *B)* The VBS1 end-to-end distance when subjected to forces ranging from 0 to 20pN. For varied force fields, the standard deviation (shade) and average (solid lines) were calculated excluding the first 75 ns of each trajectory. (see legend and Methods). *C)* The DSSP hydrogen bond estimating technique [146] was used to assess helical content at each time frame. Like before, the standard deviation (shade) and average (solid lines) were calculated excluding the first 75 ns of each trajectory.

has crossed the first energy barrier towards unfolding (extension > 4.6 nm, dotted lines in figure 4.9c), I27 started to make contact with the tail, as well. This speaks for an interesting competition-like mechanism in which VBS and the vinculin tail compete for association to the D1 domain.

4.5. The VBS peptide shows a bimodal distribution of end-to-end distance under force

The eleven vinculin binding sites distributed along the talin rod domain are usually folded away in four- or five-helix bundles and are inaccessible to vinculin unless the bundles unfold, which can happen, for example, by a tensile force across the protein. [43] This force-activation is an intricate process where a force that is too low will prevent VBS exposure, while a force that is too strong will weaken the helicity and make vinculin

binding more difficult. Hence, the goal of this section is a characterization of the force dependence of the helical propensity of the VBS peptide. The first set of simulations was built up with the same framework as previously, using the AMBERf99sb-ILDN force field with hydrogen virtual sites and the Tip3p water model. The results show dynamic folding and refolding of helices that was heavily force-dependent, as seen in figure 4.10. To rule out any unanticipated influence on the folding and refolding process arising from the use of hydrogen virtual sites, completely atomistic simulations were run as a control. Common protein force fields are known to be slightly too sticky, i.e. they overvalue protein-protein interactions, which helps to recreate protein structures on the one hand, but can trap disordered proteins in coiled up states, on the other. Since the peptide on its own is very similar to a disordered protein, we aimed to alleviate this problem by running a third set of simulations with the Tip4p water model. The results of the simulations are compiled in figure 4.10. When compared to Tip3p simulations, Tip4p simulations on average showed a slightly larger end-to-end length at intermediate forces. The overall helix propensity was also smaller, but the elevated likelihood of observing a helix below 10 pN remained intact. In the low-force environment, the Tip3p water model did indeed over-represent helical states. Yet, the general scheme was preserved across all simulation classes; the helix propensity was more pronounced at forces under 10 pN, after which it started to decline. 10 pN corresponded to the inflection point in the peptide end-to-end distance, which increased from a coiled/helical state with ~1 nm to a fully unfolded and stretched state with ~6 nm at 20 pN.

Prior to the previously discussed coil-to-helix transition described by Tapia-Rojo et al. [59], the magnetic tweezers experiments showed that a tensed talin R3 domain folds and refolds dynamically and that the contraction in end-to-end distance that is attributed to vinculin binding occurs from the unfolded state. With our novel insights about the intriguing dynamics of the VBS1 peptide, Dr. Rafael Tapia-Rojo set out to further analyze the extension traces gathered for the published study [59]. By this, a total 20 events of smaller variability that were not related to vinculin binding were discovered. One of these events is shown as an example in figure 4.11d. These events were characterized by a duration of a few tens of seconds and a bimodal distribution of extensions, as evident from figure 4.11d-e. Revisiting our single-peptide simulations, we found a similar bimodal distribution at forces close to the inflection point of the peptide extension (see figure 4.11a-c). The bimodal distribution was observed most clearly for a force of 10 pN with Tip3p water and hydrogen virtual sites. Without virtual sites, the double top persisted at 10 pN, albeit less clearly separable, while with Tip4p water the peptide extension was shifted towards a more unfolded state.Higher forces shifted the peak positions towards longer extensions

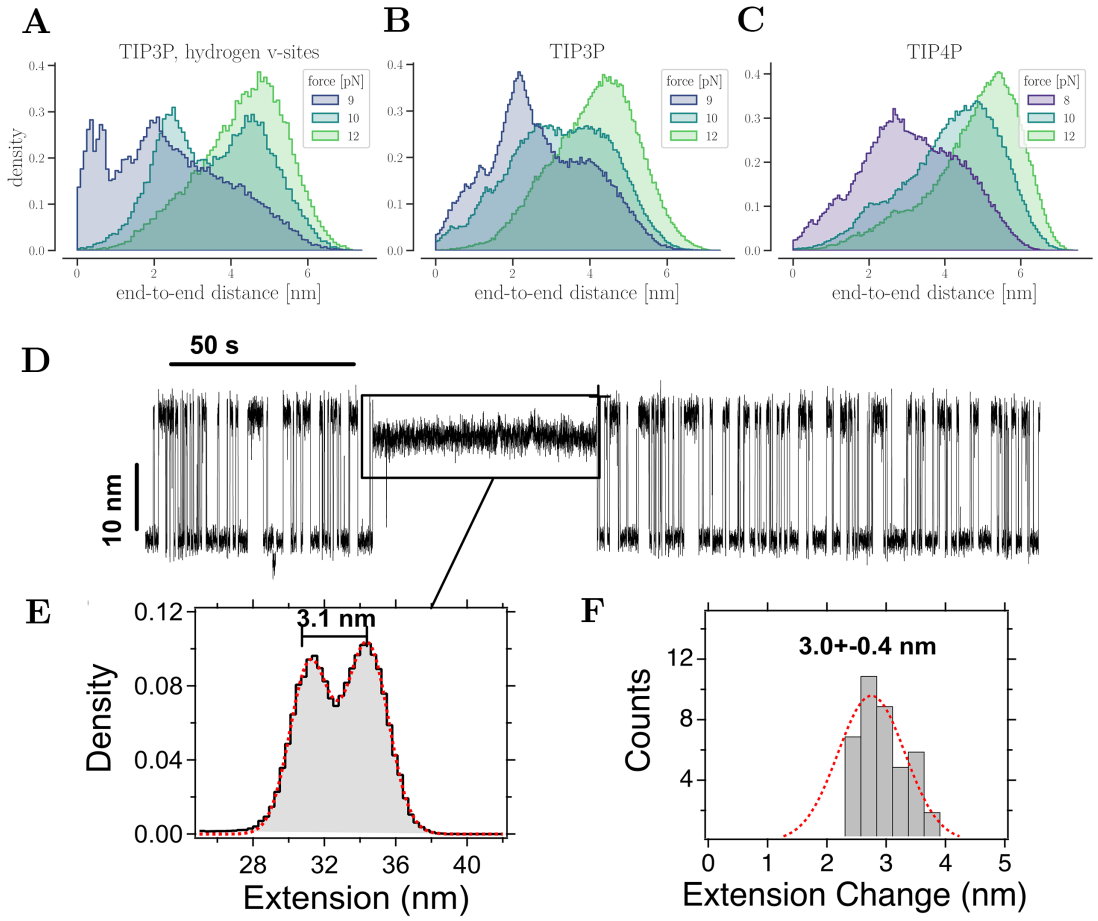

Figure 4.11.: Simulations and experiments agree on bimodal distribution of VBS end-to-end distances under force. *A)-C)* Transition of the distribution of VBS-extension at forces in proximity of the inflection point (compare figure 4.10c). The data shown in each panel stems from 3 replicas per force where the first 75 ns of the 1 µs-long run were excluded. *D)* A representative recording from magnetic tweezers experiments where a talin R3 IVVI mutant that contains two VBS (as featured in [59]) is tensed with a constant force of 9 pN. During the analysis of 15 molecules, 20 of these events were found. *C)* The events are characterized by a bimodal distribution of extensions. *F)* The contractions, i.e. the step sizes, across the 20 analyzed events follow roughly a Gaussian distribution. *D)-F)* Experiments were carried out by the collaborator Dr. Rafael Tapia-Rojo (King's College London).

and, in the case in which a bimodal distribution can be clearly discerned (10 pN, v-sites), the separation of 2.6 nm lay slightly under the experimentally observed value of 3.1 nm.

Since 2004, structural data has accumulated providing evidence for where VBS bind on the vinculin D1 domain and how the bound structure differs from the apo state. The VBS1 helix inserts into the 4-helix D1 bundle and turns it into a 5-helix bundle. [44, 144] All crystallographically resolved VBS-D1 complexes to date display this 'helical bundle conversion' scheme. [44, 58, 141, 144, 147] The crystallographic data demonstrates that if VBS is bound, the hydrophobic interactions in D1-Tail interface are weakened which allows for easier vinculin activation. However, at the time this project was commenced, binding between a VBS peptide and vinculin had only been observed with truncated vinculin constructs which lack the tail domain. [43, 59] The recently published preprint by Wang et al. [148] and our study are the first to report full-length vinculin directly binding to talin on a single-molecule level. Similar to the data presented for the D1 domain, [59] the binding involves a contraction of a tensed VBS which demonstrates that a mechanical force across the talin rod is imperative for focal adhesion reinforcement by vinculin.

We showed that a single VBS peptide undergoes a full transition from a fully coiled and helical state to a fully extended state for forces between 0 and 20 pN with a turning point in end-to-end distance at 9-10 pN. Furthermore, we observed a bimodal distribution of end-to-end distances over the course of the simulation indicating a dynamic coexistence of helical and extended state. Interestingly, experiments by Dr. Rafael Tapia-Rojo found events with a very similar bimodal distribution for the talin R3 domain under 9 pN of tensile force in magnetic tweezers. Assuming this effect can be attributed to a dynamically un- and refolding VBS, together with the maximum in vinculin binding probability at this force leads to the hypothesis that this dynamic coexistence provides the ideal precursor for talin-vinculin association. The increased distance between the peaks of the bimodal distribution in experiments may be accounted for the by the existence of two VBS in the talin R3 domain whereas our simulation only consider one individual VBS. Taken together, our findings provide an explanation on how the vinculin D1 4-helix bundle is turned into a 5-helix bundle; a completely helical VBS does likely not fit into the D1 binding pocket, but one that has been unfolded does and subsequent refolding inside of the binding pocket constitutes the binding event and causes the conversion of the D1 helix bundle.

Our force-probe MD simulations revealed subtle differences in the resistance against unfolding across different VBS. According to Haining et al. [149] some of the talin rod domains are more resistant to force than others. In fact, they classify the 12 rod domains into three categories: strong, intermediate, and weak. Interestingly, there are no VBS

in the strong rod domains, but the weak and intermediately strong domains harbour all eleven known VBS. Our findings imply that VBS1 is more force resistant than VBS33 and 36 (Figure 4.6). We may generalize our findings using sequence alignment (see appendix figure A.3) and hypothesize that 'weak' talin domains contain stronger VBS and intermediate domains include weaker VBS. This argument is reasonable in the context of focal adhesion turnover, because under mechanical stress, the weakest talin domains would recruit VBS first during FA maturation, and they would also be the last to release vinculin during FA disassembly.

Remarkably, full length vinculin displayed a different unbinding probability than its fragment D1 (Figure 4.8). This was observed both in our simulations and also confirmed by experiments. Analysis of the MD data helped identify a competition-like mechanism that involves particularly four residues that either interact with the VBS or the vinculin tail. This also provides a first clue towards how talin binding is involved in activation of vinculin which will be investigated in more detail in the following chapter.

5

Talin loosens the vinculin inactive state

5.1. Introduction

Focal adhesions develop when nascent adhesions, which are tiny, dot-shaped and only transiently stable, mature inside the lamellipodia. Maturation is myosin-II-dependent and grows the nascent adhesions into large band-shaped structures as more and more FA proteins are hierarchically recruited. [20, 150] Each FA turns into a highly force-sensitive signalling hub in which the interplay between talin, vinculin, and F-actin is responsible for the core regulatory action (see figure 1.2 and section 1.2). The cellular forces that govern the lifecycle of focal adhesions originate from the actomyosin machinery and are strongly fluctuating in space and time. The locations that exhibit the highest cellular forces typically coincide with the assembly sites of FAs. [3, 151] Single-molecule force measurements have shown vinculin to be under forces as high as 10 pN if engaged in FAs. [40, 152] Similar experiments have shown talin to be subject to similar forces [41] and that the extracellular domains of integrin receptors can even experience forces exceeding

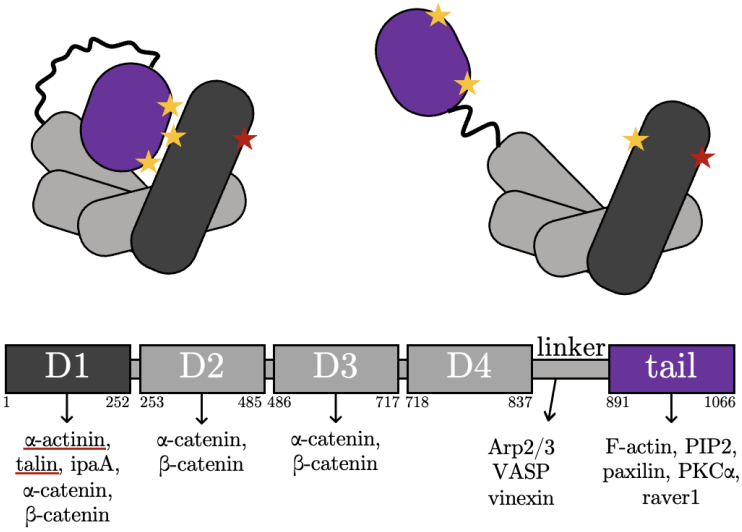

Figure 5.1.: The majority of the protein binding sites on vinculin are cryptic. Schematic representation of vinculin and its protein interaction sites. The four head domains (D1, D2, D3, and D4) are shown in gray and the tail domain in purple. Cryptic binding sites are represented as yellow stars and are only accessible if the tail domain dissociates from the head domain, i.e. the protein is activated. The interaction site for talin (red star) is located on the solvent accessible surface of the D1 domain (dark gray).

50 pN. [136, 137] Consequentially, mechanical force plays a pivotal role in all stages of focal adhesions development and turnover.

The 5-domain, 1066-residue-long protein vinculin can be found in force-bearing cellular junctions including focal adhesions, adherens junctions, as well as immunological synapses. [153–155] Undoubtedly, vinculin constitutes an important signaling molecule since it harbours binding sites for a large variety of proteins as indicated by figure 5.1. A well-established, and arguably the most important role of vinculin, is the mechanical reinforcement of the link between the actin cytoskeleton and the cellular adhesion complex. [115, 150, 152] The adhesion proteins talin, α-actinin, and α-catenin all contain so-called vinculin binding sites. As elaborated upon in the previous chapter, VBS are helical and, in absence of any mechanical cue, usually hidden away in helix bundles. While α-actinin and α-catenin only contain one VBS, talin contains eleven [47, 58, 156] and, interestingly, the structural mechanism by which the VBS bind to vinculin is conserved across all of them. [44, 47, 144] The mechanism was discovered by Izard et al. [44] and coined as 'helical bundle conversion' (for an explanation refer to section 4.1). The findings presented in the preceding chapter demonstrated that different VBS exhibit varying

stabilities against unfolding. Now, in this chapter, the focus lies on the influence of the different VBS on the vinculin protein itself.

For vinculin to unfold its full signalling potential, activation is required as the majority of the binding sites are of a cryptic nature, i.e. they are not accessible to other proteins as long as vinculin remains in its auto-inhibited conformation. [157] The exact process by which vinculin is activated is not yet fully understood, and literature offers different hypotheses. Bois et al. [47], for example, suggest that the α-actinin VBS alone can cause vinculin activation. Other studies argue that a collaborative effort of a VBS and actin is necessary to open up the protein. [45, 46]

Literature describes three possible actin binding sites on the vinculin tail which all share a common feature; the binding site is either partially or fully occluded in the auto-inhibited conformation and, hence, actin is not able to bind to closed vinculin on its own. [24–26] While VBSs readily bind to isolated vinculin D1 domains, [44, 47, 144] binding to full-length vinculin had previously only been observed when the head-tail interface was artificially weakened [158] or the protein was constrained to an opened conformation in simulations. [46] The results we obtained in collaboration with Dr. Rafael Tapia-Rojo (4.4) are amongst the first – to our knowledge – to report single-molecule evidence of auto-inhibited full-length vinculin binding to a VBS-containing talin domain if the latter is under force. This supports the hypothesis that mechanosensitive VBS-binding activates vinculin either directly or partially, allowing actin to attach more readily and establishes an order of events in which VBS binding proceeds actin binding.

In this project, we sought to understand how vinculin activation is influenced by talin VBS1, talin VBS3, and the α-actinin VBS (ACT). Using force-probe MD simulations with modelled full-length vinculin complexes, we found that the talin VBSs decrease the barrier that counteracts activation, while there was no effect caused by the α-actinin VBS. With VBS1 causing the strongest effect, we next aimed to understand the molecular underlyings of the facilitated activation. Combining force distribution analysis (FDA) and correlated motion analysis, we identified the responsible residues and designed two novel vinculin mutants that aim to destabilize the D1-tail interface in a similar manner to VBS1-binding. In an experimental effort with the Geiger lab (Weizmann Institute of Science, Israel) and the Medalia lab (University of Zürich), we revealed that the new vinculin mutants are able to bundle actin filaments without the presence of functionalized talin-VBS1, indicating that the mutations do indeed facilitate activation and, as a consequence, actin binding and bundling.

5.2.1. Simulation details

The GROMACS [110] version 2018.4 was used for all simulations discussed in this chapter. The AMBER-ff99sb-ILDN force field with Joung ions, [62, 143] and the Tip3p water model [159] were utilized. Prior to production runs, the proteins were solvated, neutralized with a 0.15 mol/L concentration of NaCl, and subjected to a 15 ps NVT and a 100 ps NPT equilibration. The NPT ensemble was kept at 300 K using the v-rescale thermostat [72] and pressure was controlled at 1 atm using the Parrinello-Rahman barostat [70] with a τ_p of 2.0. The use of hydrogen virtual sites [145] allowed for an integration time step of 5 fs. The 1TR2 full-length vinculin structure [160] excludes the proline-rich linker between residues P843 and P877. For our study, we inferred its conformation using the Chimera [128] interface to MODELLER. [125–127] To model the full-length VBS

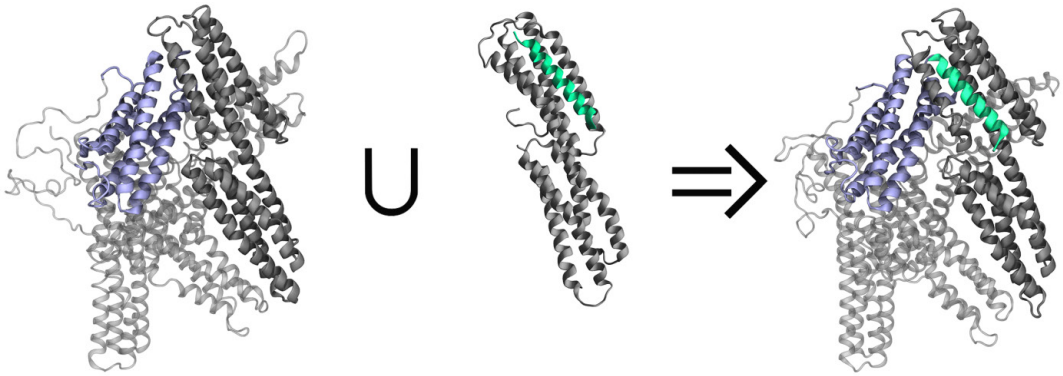

Figure 5.2.: Assembly of the full-length vinculin VBS complex. The complexes were built combining the full-length vinculin apo structure (pdb-ID 1TR2). Using pymol, the structures of the vinculin D1 domain in complex with the α-actinin VBS (pdb-ID 1YDI), VBS3 (pdb-ID 1RKC), and VBS1 (pdb-ID 1T01) were fused to the the remainder of the protein and subsequently equilibrated for 1 µs.

complexes, we use the pdb structures 1T01 (VBS1) [144], 1RKC (VBS3) [44], and 1YDI (ACT) [47] and combine them with the full-length vinculin structure 1TR2 adapting the procedure described by Golji and Mofrad [161] and illustrated in figure 5.2. Using pymol, we generated a hybrid structure minimizing the RMSD between the Cα-atoms of the D1 domains. The new structures were first energy minimized in vacuum, then, the simulation box was filled with Tip3p water and 0.15 mol/L NaCl after which the solvent energy was minimized by enforcing position restrains on the protein backbone and sidechains. Subsequently, the position restraints were gradually released in a three-step procedure

in an NVT ensemble. Finally, an extensive 1 µs-long NPT equilibrium simulation was conducted to ensure proper relaxation of the complexes.

For the force-probe MD runs, force was applied to the centre of mass of the tail domain, and on the the talin binding site located on the D1 domain as described by [44]. For the complexes, two distinct locations of force application were compared, the first one being the centre of mass of the talin binding site as for the apo-state protein, and the second being the VBS peptide itself. Figure 5.3a and figure 5.4a represent the simulation protocol for the unbound protein and the complex, respectively.

5.2.2. Umbrella sampling

For the free energy profiles computed here, we used a method called umbrella sampling. Details on this method are provided in section 2.1.7. To evaluate the free energy of the protein opening, the pull coordinate was used as a reaction coordinate. For each of the investigated systems, we exported 30 snapshots from one of the slowest pulling simulations and ran 3 10 ns-long harmonically biased simulations using a spring constant of 1000 $\mathrm{kJmol^{-1}nm^{-2}}$.

5.2.3. Experimental methods

Vinculin mutant production

The plasmids for the newly designed vinculin mutants were constructed by the protein production unit at the Weizmann Institute of Science in Israel in collaboration with the Geiger lab. The 4 and 5 mutations were introduced into the vinculin coding sequence with the TPCR method [162] using a Q5 High-Fidelity Master Mix (NEB). In the initial step the 4 mutations (K944A-R945A-D1013A-E1015A) were introduced and on the resulting construct the 5th E986A mutation was introduced. The primers that were used to introduce the mutations are:

- vinculin 944,945A-F: GAGGGGGCAGTGGTACCgctgcaGCACTCATTCAGTGTGCC
- vinculin 1013,1015A-R: CTCTGTGGCCTGCTCAGAtgCCTCAgCACTGATGTTGGTCCGGC
- vinculin 986A-F: CAACCTCTTACAGGTATGTGccCGAATCCCAACCATAAGCACC

The entire open reading frame including the promoter region was verified by DNA sequencing. Protein expression and purification was carried out in the Medalia lab at the University of Zürich following the protocol described by Boujemaa-Paterski et al. [163]

TIRFM actin bundling experiments.
The plasmids for these mutants were sent to Dr. Rajaa Boujemaa-Paterski from the Medalia lab at University of Zürich, who had previously shown that vinculin – if activated by substrate-bound VBS1 – bundles effectively branched actin networks. However, without the activating influence of VBS1, bundling was much less pronounced. [163] With the plasmids of the 4- and 5-mutant, the proteins were expressed and purified and tested for their actin-bundling capability by total internal reflection fluorescence microscopy (TIRFM). In their recently published study, Boujemaa-Paterski et al. [163] combine adhesive surface pattering on a protein-repellent surface with dual-color TIRFM, to show that vinculin, if associated to talin-VBS1, interacts with branched actin networks and initiates actin bundling. The plasmids for the mutants we designed in this work were made by the protein production unit at the Weizmann Institute of Science in collaboration with the Geiger lab and then sent to the Medalia lab at the University of Zürich. There, using the method described in the publication [163], Dr. Rajaa Boujemaa-Paterski carried out similar TIRFM experiments to probe the here-described mutants interaction capabilities with branched actin networks.

5.3. Force-induced vinculin activation

5.3.1. The apo-state protein requires high activation forces

The most likely pathway of *in vivo* vinculin activation involves talin binding on the D1 domain and subsequent actin recruition to the vinculin tail domain. In a first step, we sought to evaluate the forces required to accomplish an opening of the vinculin protein using force-probe MD simulations. As anchor points for force application, we chose the talin binding site, and since the exact first-contact site of actin is unknown, the COM of the entire tail domain. Figure 5.3a illustrates the pulling protocol with snapshots extracted from a representative simulation, and figure 5.3b shows the ensuing force-extension curves. Note, that the extension shown here is not the distance between the two pull groups, but the distance between the constantly moving-apart points that are connected with virtual springs to the pull groups. In phase 1 (as highlighted in figure 5.3), force builds up across the protein, as indicated by the linear slope in the force-extension curve. At the moment when the head–tail interface ruptures, a steep drop in force can be observed (2). After the rupture event, the protein extends without any notable resistance as the head and tail move further apart (3). We recorded the maximum force in each trajectory, which corresponds to the the moment right before rupture occurs. The magnitude of this rupture force depends on the pulling velocity (see figure 5.3c), as one would expect considering

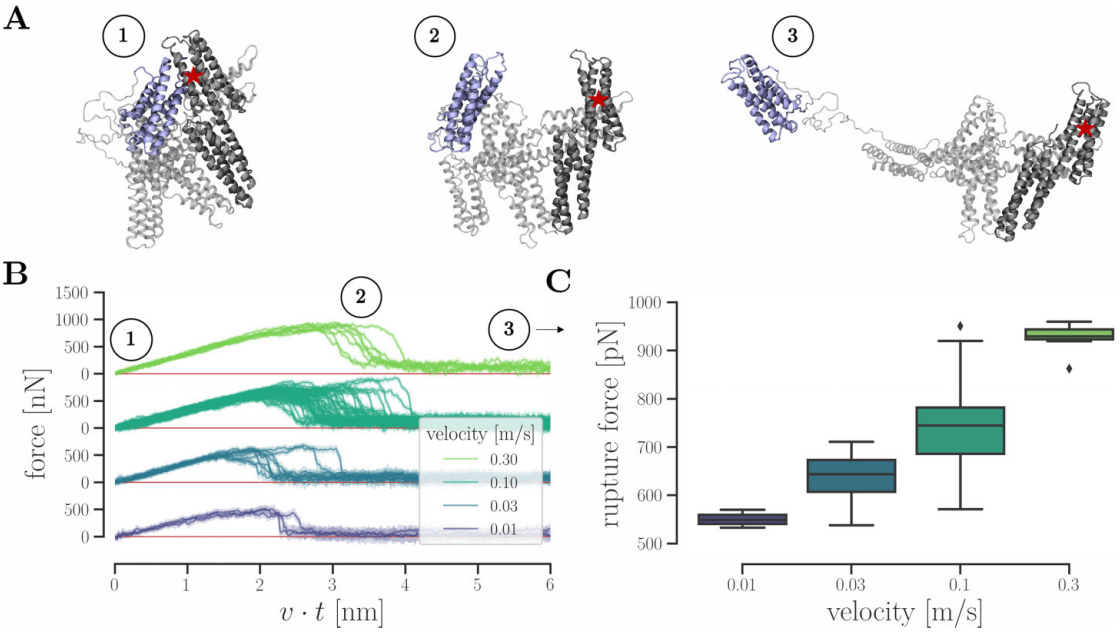

Figure 5.3.: Vinculin opening requires high forces. *A)* Illustration of the force-induced vinculin opening. Force is applied to the COM of the talin binding site (red star) which is located on the D1 domain (dark gray) and the COM of the tail domain (purple) of vinculin. The force acts in opposing directions along the axis that connects the two pull groups. *B)* Corresponding force-extension curves for pulling speeds between 0.01 and 0.3 m/s. At the peak force, D1 and tail dissociated. *C)* Dependence of the rupture force on the pulling velocity.

the bell model. [97] However, we did not attempt a fit of the data to a such a model, as we do not deem the here-obtained sampling extensive enough for this purpose. The forces recorded here lay between 551 pN (minimum at 0.01 m/s) and 960 pN (maximum at 0.3 m/s), and with that, they are comparable in magnitude to the forces recorded for simulated dissociation of the streptavidin-biotin complex, [82, 93] which speaks for the remarkably high stability of the D1-tail interface.

5.3.2. VBS binding decreases the activation force

As crystallographic data suggests, the vinculin D1 domain undergoes dramatic structural changes upon VBS binding, which also affects the D1-tail interface. [44] Understanding the implications of these changes on vinculin activation is of great interest. To this end, we subjected a thoroughly equilibrated VBS1-vinculin complex (see section 5.2.1) to similar force-probe simulations as described above for the apo-state protein. The protocol is illustrated by snapshots gathered from one of the pulling trajectories in figure 5.4a. On the D1 domain, force was applied either to the COM of talin binding site, like above,

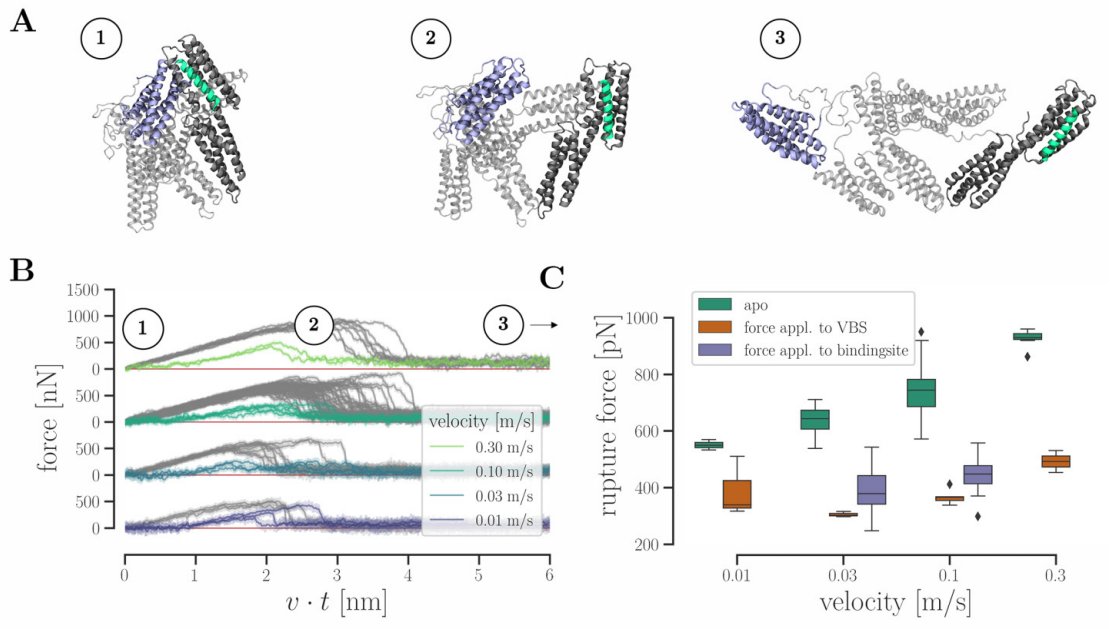

Figure 5.4.: VBS1 strongly decreases the force required for vinculin opening. *A)* Representation of the pulling protocol, which is similar to figure 5.3. For the twos simulation sets, force is either applied on the VBS peptide (shown in green) directly or on the talin binding site on the D1 domain. *B)* Force-extension curves for force-application to VBS1 and pulling speeds between 0.01 and 0.3 m/s. For comparison, the force-extension traces of the apo-state protein are shown in gray in the background. *C).* The resulting rupture forces in relation to the previously obtained rupture forces for the apo-state protein.

or to the COM of the VBS1 peptide. Figure 5.4b shows the force-extension curves for pulling directly on the peptide, and figure 5.4c compares how the rupture forces changed when varying the anchor point of the force, as well as when put in relation to the rupture forces of the unbound protein. From the force-extension curves, we can immediately discern that the forces required for detaching D1 from the tail decreased dramatically in the presence of VBS1. If force was applied directly on the VBS, the lowest resulting force of 305 pN (0.03 m/s) and the highest resulting force of 530 pN (0.3 m/s) illustrate the strength of the effect. At a pulling velocity of 0.1 m/s, the speed with the highest available sampling, the mean of the rupture force dropped from (745 ± 16) pN to (368 ± 12) pN, which constitutes a (48 ± 2)% decrease. Despite this large difference, we cannot rule out a possible influence of the slightly changed pulling direction due to the different force-anchor point. To quantify this further, we set up additional simulations where the complex was tensed from the talin binding site, akin to the protocol used for the unbound protein. Indeed, force application to the talin binding site ensued slightly higher rupture forces. With (446 ± 8) at 0.1 m/s, these simulations only exhibited a decrease of (40 ± 2)%

compared to the apo-state protein, which is still significantly smaller. To ensure better comparability and eliminate any influence arising from a changed pulling axis, subsequent complex simulations and associated analysis were carried out with the force applied to the talin binding site.

Before proceeding with study and extending the investigations with more VBS peptides, a series of tests was conducted to assess the quality of the bound complex's structure. By this, we aim to ensure that our results are not tainted by any artifacts arsing from the complex-building procedure. VBS1 was removed from the bound VBS1-vinculin complex which was used as a starting structure for four equilibration simulations of 1 µs. From each of the relaxed deletion structures, 10 force-probe simulations at 0.1 m/s, analogously to figure 5.3a, were conducted. Figure 5.5a gives the force-extension traces resulting from one of the independent equilibration runs, and figure 5.5b shows the resulting rupture forces after each of the four equilibration simulations. Upon deletion of VBS1, the force extension curves matched much more closely those seen for the unbound structure (see figure 5.5a, blue and green curves) with forces peaking at around (877 ± 17) pN. A full description of the data is presented in the appendix table A.4. For the equilibration trajectories, the residue-residue contacts, within a cutoff radius of 3.5 Å, were calculated and classified according to whether or not they matched one of 53 contacts identified in the crystal structure. In figure 5.5c the evolution of the number of these contact classes is given. With ≤ 20 the number of crystal-structure-like contacts started at a low level but after approximately 400ns the number rose to ~35 indicating a recovery of ~60% of the apo contacts. The number of other contacts remained at a low level, unaffected by the progress of the simulation.

As a last control, the free energy profiles along the pull-coordinate were calculated, with windows extracted from representative activation trajectories (Figure 5.5d). Here, ϵ is the distance between the COMs of the respective pull groups. For details on the free energy calculations used here, please refer to section 2.1.7. As expected, ΔG rose much more steeply in the apo simulations compared to the VBS1 complex, reaching an almost twofold higher difference in ΔG. After VBS1 deletion, particularly the region of the reaction coordinate between 3 and 5 nm recovered to be almost indistinguishable from the apo simulation. This is precisely where the first rupture between D1 and the tail has been observed to happen. The subtle differences beyond 5 nm may be due to differences in the subsequent protein unfolding steps which may simply depend on the chosen trajectory. For the the initial activation step which consists in a rupture of the D1-tail interface, we fully recovered apo-like properties after VBS1 deletion. Hence, we may assume the complex-building protocol yielded a functional protein.

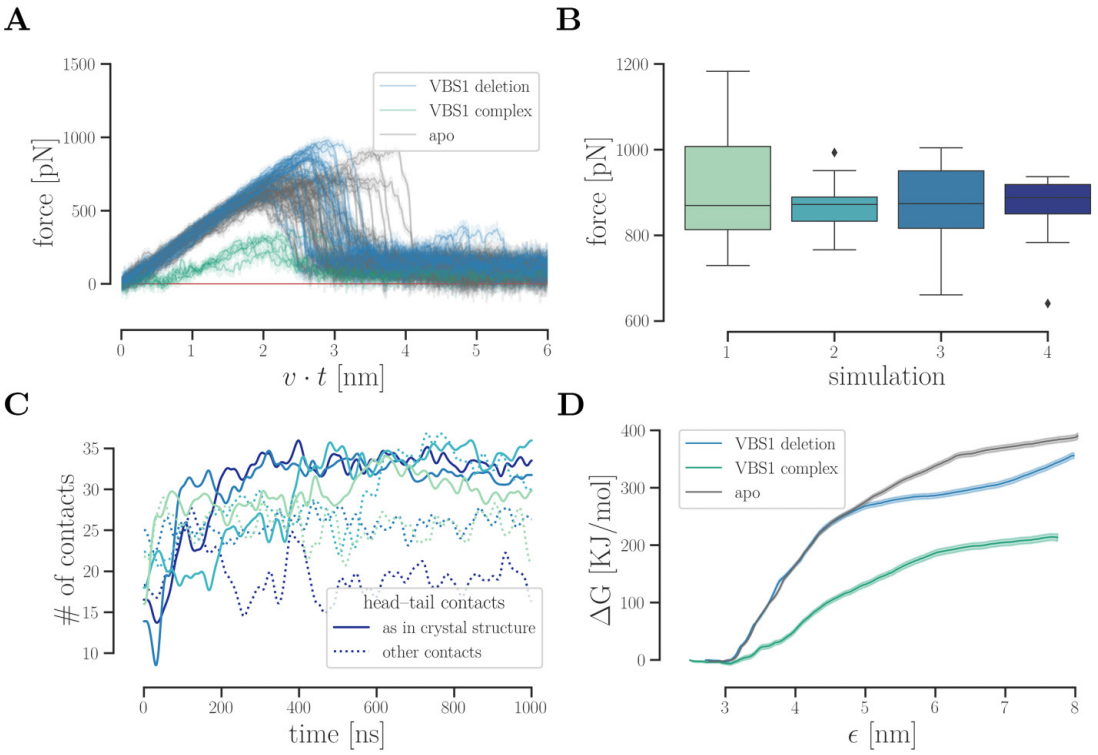

Figure 5.5.: Apo-state properties are recovered after VBS1 deletion. *A)* Force-extensions curves for force-probe simulations of the VBS1 complex (green), the apo-state protein (gray) and the 'recovered' apo state after the VBS1 peptide was deleted and the resulting structure was equilibrated. *B)* Following VBS1 deletion, four independent equilibration runs were carried out. The box plot shows the highest forces observed in 10 pulling simulation started from each of the relaxed structures. *C)* The solid lines show the number of contacts that are recovered during the four equilibration simulations. As a reference, we used 53 head-tail contacts identified in the crystal structure with a 3.5 Å cut-off. Dotted lines show the number non-apo contacts. *D)* Mean (solid line) and standard deviation (shaded area) of the free-energy profiles calculated by umbrella sampling for the opening of the described structures.

Having validated the complex formation protocol, we extended the study by two additional VBS, the talin VBS3, and the α-actinin VBS (ACT), which have both been reported to also weaken the D1-tail interface. [44, 47] As before, the D1-complex structures were combined with the full-length protein and relaxed with the procedure described in the methods section 5.2.1 with a 1 µs-long equilibration run as a last step. We computed the average structures from the final 100 ns of each trajectory and performed a least-square fit to match the D1 domain's Cα-atoms of each of the complexes to the apo structure. For a visual comparison, figure 5.6 gives the result of the least-squares overlay for the ACT, VBS3 and VBS1 bound structures in orange, cyan and deep purple, respectively. In each structure, the bound VBS is colored green and the underlying apo structure

gray. Next, we analyzed the intradomain contact map for the D1 head domain of the apo structure of vinculin in order to better understand the allosteric implications of VBS binding. Using ConAn [112] (see section 2.4.3), the average distances between residues throughout the last 100 ns of the simulations were used to identify residue pairs fewer than 1 nm apart. Taking advantage of the symmetric nature of contact maps, we present a traditional map only on the top half of the diagonal for the complexes (Figure 5.6). The distance discrepancies between the residues of the complexes and the corresponding residues of the apo structure are depicted below the diagonal. In the contact map of the apo structure, we can clearly identify prominent interfaces between helices 1 and 2; helices 2 and 3; helices 2 and 4; helices 3 and 4; and helices 1 and 4, as predicted by the crystal structure. [160] The intradomain contacts for the bound complexes reveal that the helix 1- helix 2 interface vanished in all three complexes, which is consistent with the VBS insertion location. Further, the contact analysis revealed subtle variations in the interface of helix 1 and 4 in the case of VBS1 and 3, as a sequence of rises and declines suggests a barrel roll of the two helices. Looking at the VBS1 complex, we see that the binding of VBS1 caused a tighter packing, forming a more compact helix bundle compared to the other two complexes. In contrast, the binding of ACT and VBS3 led to an increase in the angle in helix 2, resulting in a kink which more closely resembled the one observed on the apo structure (see the structures shown in figure 5.6). For the ACT complex, the interface between helix 1 and helix 4 weakened as distances increase by ~0.5nm, which underlies the observation of a less dense packing of the helix bundle.

Overall, the structural differences of the three VBS in question were rather subtle. However, our focus has been restricted to the D1 domain up to now. To find out, whether the different VBS differ in their impact on the D1-tail interface, and hence the activation of the protein, a set of pulling simulations, following the protocol depicted in figure 5.4a, was carried out and analyzed. Based on the force-extension curves, the amount of force required for the rupture of the head-tail interface, for the apo structure and each of the vinculin complexes, was estimated and is illustrated in figure 5.7. The corresponding raw data is tabulated in the appendix table A.3.

When the results for the apo and complex structures are compared for both pulling velocities, it is clear that binding of VBS1 and VBS3 to vinculin decreased the head-tail interface rupture force, but binding of ACT appeared to have little or no influence on the force required to rupture the interface. At a pulling speed of 0.03 m/s, the rupture force of the apo structure is approximately (637 ± 21) pN with that of the ACT complex being approximately (590 ± 29) pN. At a pulling speed of 0.1m/s, we recorded (745 ± 16) pN for apo, and (760 ± 19) pN for the ACT complex. A two-sample t-test on this data gave

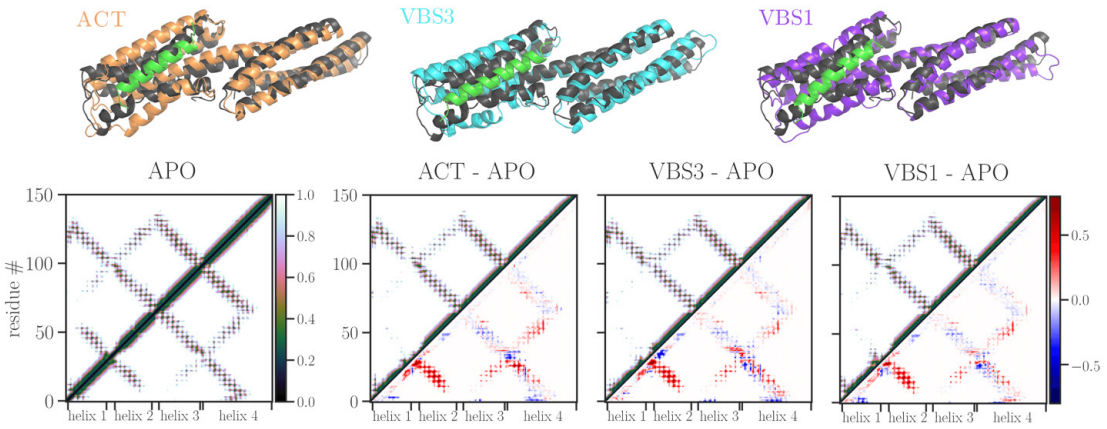

Figure 5.6.: Different VBS cause subtle differences in the D1 conformation. The D1 domain in complexes with α-actinine (orange), talin VBS3 (cyan), and talin VBS1 (purple) are superimposed with the apo structure (gray) with a least squares fit between Cα-atoms in the D1 domain. For the apo-state D1 domain, a contact map is shown which depicts distances of less than 1 nm between residues. For the complexes, contact maps of the intradomain contacts are given above the diagonal. The distance difference maps between the apo-state and the complexes are shown below the diagonal and measured in nanometers. (The bottom front helix is 1, the front top helix is 2, the rear top helix is 3, and the bottom back helix is 4.)

p-values of 0.22 and 0.57, respectively, leading us to conclude that the binding of the α-actinine VBS did not have a significant impact on the activation barrier. The distributions of rupture forces of the VBS1 and VBS3 complex both led to a p-value of $p < 0.001$, with VBS1 causing the strongest reduction in rupture force.

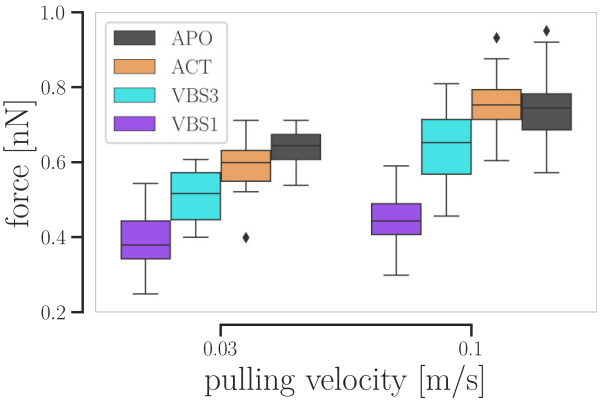

Figure 5.7: Different VBSs dissimilarly impact the rupture force. The distributions of the highest observed force in each trajectory for a set of simulations ranging over two pulling speeds (0.03m/s and 0.1m/s) are represented by a box plot. For each velocity and complex type, the plot represents data from at least 10 replicas. The date and statistics the plot is based on can be found in the appendix table A.3.

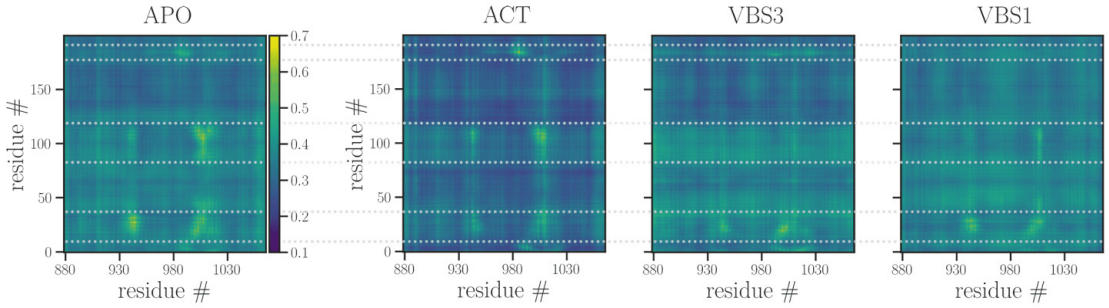

Figure 5.8.: The interactions between vinculin D1 and tail portrayed by generalized correlations maps. The data shown is extracted from force-probe MD trajectories with a pulling speed of 0.1 m/s. The correlations were computed for each simulation using a 5 ns-long fraction of each trajectory that precedes the moment of 300 pN force across the protein. The average of 20 runs is presented for each complex type.

5.4. What causes the weakening?

In order to understand the mechanism behind the variations in rupture forces, the generalized correlations [107] between the residues motions in the D1 and tail domains were computed for the apo structure and the various complexes (see section 2.4.1 for details). Figure 5.8 illustrates the average correlation coefficients which were calculated for the 5 ns of each trajectory that antecede a force of 300 pN applied to the protein. The force of 300 pN was chosen to ensure comparability in a force range that was reached by all trajectories. Strongly correlated motions are indicators of residues being strongly coupled together, helping to pinpoint possible force transmission pathways. Examining the apo structure, three major regions on the D1 domain with pronounced correlation with the tail domain were identified. The regions lay between residues numbers 19-33, 88-116, and around 185. As a guide to they eye, the gray dotted lines in figure 5.8 mark their positions. Even though the ACT complex experienced a slight loss of correlation especially in the 19-33 region where it interacts with the tail residues 940-945, the 5 major interaction clusters present in the apo state remained intact. In the case of VBS3 binding, almost all correlation within the 88-116 cluster was lost, and, while strong correlations stayed in place in the 19-33 cluster, residue 29 was particularly affected showing a smaller correlation in comparison to the reference. In addition, residues 19 to 25 gave away most of their correlation with tail residues 944 and 945. Similar to VBS3, VBS1 led to an extensive loss of the strong correlations of residues 88-116, except for the residues interacting with the tail residue 1008 which remained strongly coupled to the 88-116 residue range. The locations of correlations between 19-33 and the tail domain were

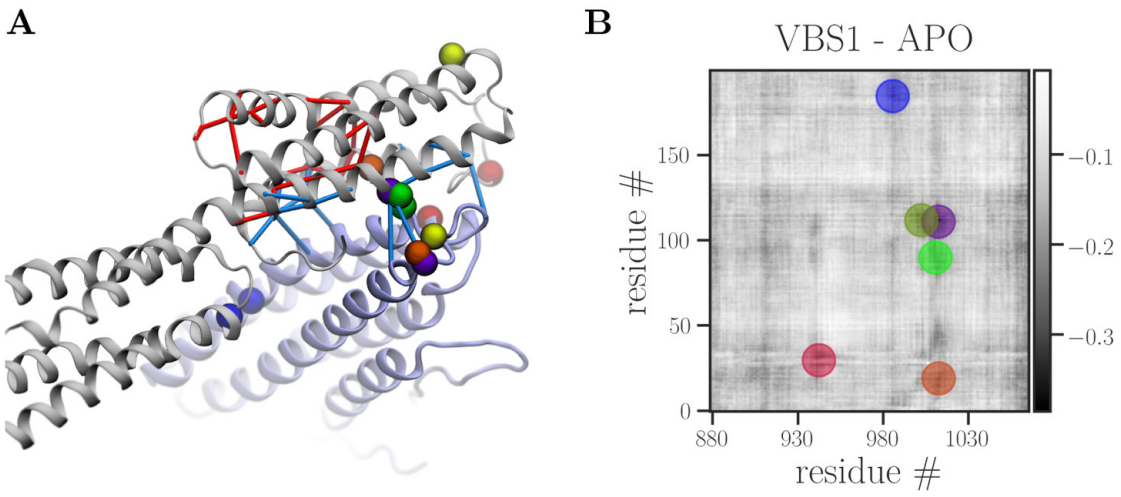

Figure 5.9.: Force distribution analysis and correlated motion analysis identify an overlapping set of residues responsible for the 'loosened' interface. *A)* Results of force distribution analysis on the the VBS1 complex and the apo-state protein. In the network representation, edges represent residue pairs that show a high change in pair-wise force with either negative (blue) or positive (red) sign. The Cα-atoms in VdW-representation correspond in color to the residues experiencing the highest correlation loss within the clusters indicated in B). *B)* Correlation difference map from APO-state to VBS1 complex. Colored circles represent groups of interaction loss identified by a weighted clustering analysis. Table 5.1 shows the strongest contributors in for each cluster.

similar to the apo state but with less intensity. Most notably, VBS1 binding caused a complete loss of the correlated motions around residue 185, which is unique to VBS1.

It is important to observe that the data presented in figure 5.8 originated from biased simulations. For control and validation purposes, the generalized correlations were also computed for equilibrium simulations and for each pulling trajectory using the 5 ns right before the rupture event as opposed to the 5 ns leading up to a force of 300 pN. The resulting correlation maps are shown in the appendix figure A.4. While they paint a similar picture, the pre-300 pN correlations we based our main analysis on seem to be best suited for the purpose. Similar force over all measurements permit a comparison across the different topologies and – other than data from unbiased simulations – may give a better intuition about the residues that are responsible for the resistance against unfolding.

Because of the comparatively high decrease in activation force and the tighter helix packing in the D1 domain (compare figure 5.6), the VBS1-bound complex was selected for further investigation. To compare the correlation differences more quantitatively, a difference map was computed (Figure 5.9b) and a simple weighted K-means cluster algorithm was used

Table 5.1.: Residue pairs with highest correlation loss. The clusters identified in figure 5.9 were scanned for the strongest contributors which are summarized in the table below and colored according to figure 5.9b.

cluster	ID1	ID2	correlation loss
0	185	987	-0.279
1	113	1013	-0.386
2	33	945	-0.289
3	20	1013	-0.262
4	113	1004	-0.296
5	93	1011	-0.247

to identify clusters of residues that lose interaction in close sequential proximity. Of each cluster, the top contributor is tabulated in table 5.1 and the residue-pair is highlighted in the structure in figure 5.9a.

We next compared this result to force distribution analysis (FDA). FDA identifies networks of residues that gain or lose interactions together. Here, networks consisting of at least five pairs of connected atoms were considered. For further details on FDA, please refer to section 2.4.2. Performing FDA on the last 500 ns of equilibration simulations of the unbound protein and the VBS1 complex, we found connected networks of pair-wise force differences which are illustrated in figure 5.9. Upon binding of VBS1 and formation of the complex, a network of interactions of increasing strength was revealed (red edges in figure 5.9). The first four helices of the vinculin D1 domain formed part of this network. Hence, the increase in interaction strength in this area stabilized the head domain, allowing very strong connections to form between VBS1 and vinculin. This is consistent with our findings from pulling simulations where VBS1 never detached from the D1 domain, even if the bias was applied directly to the peptide. Also, it is in agreement with the tighter helix packing in the D1 (see figure 5.6).

Consolidating the results from FDA and correlated motion analysis, we obtained an excellent agreement across the two methods, especially for the clusters 0-4 specified in table 5.1 (compare with appendix figure A.6). With the help of these data, we sought to design vinculin mutants that incorporate mutations that weaken specifically those connections in the head-tail interface that are affected by VBS binding. In close collaboration with the Geiger lab and the protein production unit at the Weizmann Institute of Science, we determined the residues best fit for such an undertaking and defined two novel vinculin mutants. A 4-mutant K944A-R945A-D1013A-E1015A that

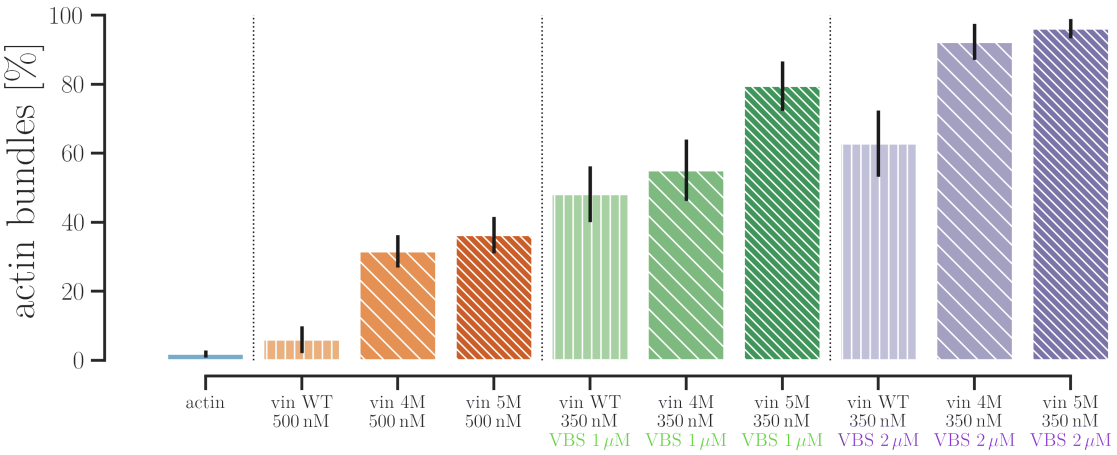

Figure 5.10.: The newly designed mutants induce actin bundling even without VBS present. The presence of bundles actin filaments was measured by TIRFM. The percentage values were obtained by dividing the amount of pixels occupied by bundled structures by the total amount of actin pixels in the full field of view (50 x 50 µm^2). The experiments were carried out by Dr. Rajaa Boujemaa-Paterski from the Medalia lab at the University of Zürich and the provided data is summarized in table 5.2.

Table 5.2.: Tabulation of the data presented in figure 5.10. Data provided by Dr. Rajaa Boujemaa-Paterski from the Medalia lab at University of Zürich.

	actin	vin WT 500 nM	vin 4M 500 nM	vin 5M 500 nM	Vin WT 350 nM VBS 1µM	Vin 4M 350 nM VBS 1 µM	Vin 5M 350 nM VBS 1 µM	Vin WT 350 nM VBS 2 µM	Vin 4M 350 nM VBS 2 µM	Vin 5M 350 nM VBS 2 µM
n	3.0	7.0	5.0	3.0	7.0	11.0	15.0	8.0	8.0	14.0
min, %	0.9	1.6	24.5	30.7	41.2	45.8	65.0	47.7	80.2	91.1
max, %	2.9	11.9	35.4	41.3	61.0	70.1	90.1	73.7	96.3	99.4
mean, %	**1.9**	**6.0**	**31.6**	**36.3**	**48.2**	**55.1**	**79.5**	**62.8**	**92.3**	**96.1**
std	1.0	3.9	4.7	5.3	8.1	8.9	7.2	9.6	5.2	2.8

is designed to weaken the interaction responsible for clusters #1-3 and a 5-mutant with an added mutation E986A that addresses the interactions of cluster #0 (see table 5.1). Remarkably, the residues involved in the competition mechanism between vinculin tail and VBS1, 27 and 29, which were identified in chapter 4 and described in figure 4.9 belong to the here-found cluster #2 (Table 5.1). Both residues interact strongly with the tail residues 944 and 945 in the apo state (see figure 5.8), which further supports these mutation sites for our intention of mimicking VBS-binding and VBS-induced activation.

5.5. Actin-binding assays confirm vinculin activation mechanism

Boujemaa-Paterski et al. [163] have previously shown that vinculin – if activated by substrate-bound VBS1 – bundles effectively branched actin networks. However, without the activating influence of VBS1, bundling was much less pronounced. With the plasmids of the 4- and 5-mutant, the proteins were expressed and purified and tested for their actin-bundling capability by TIRFM. In these experiments, branched actin structures move though a mirco-flow chamber mimicking the retrograde actin flow in lamellipodia. By the time of writing this thesis, first data from TIRFM experiments were already available. The prevalence of actin bundles as observed in these experiments is summarized in figure 5.10 and table 5.2 is based on multiple TIRFM measurements as shown in appendix figure A.7. The TIRFM data also revealed that branched actin networks exhibit a very low bundle propensity when on its own. If wild-type vinculin (vin WT) is added at a concentration of 500 nM, a slight yet not significant increase in actin bundling was discerned. When instead the mutants were added, the percentage of bundled actin grew to $(31.6 \pm 2.1)\,\%$ for the 4-mutant (vin 4M), and to $(36.3 \pm 3.0)\,\%$ for the 5-mutant (vin 5M).

Here, the findings from their publication [163] were reproduced, as the addition of vinculin-activating VBS1 elevated the level of actin bundles measured with wild-type vinculin – to higher levels than observed for the mutants. Nonetheless, the highest levels of actin-bundling were detected when combining VBS1 with the mutants, with the 5-mutant leading to even higher levels than the 4-mutant. These findings suggest that the computationally motivated mutations do indeed lead to vinculin activation in a way that resembles VBS1-binding. While the mutations alone were not as effective in vinculin activation, the contributions of the mutations and VBS1 binding were partly additive, suggesting that mutants do not fully disrupt the head-tail interaction but significantly increases the proteins propensity to forego the head-tail interaction.

5.6. Discussion

The subject of this chapter was the investigation of vinculin activation and the implications brought upon it by talin or α-actinine binding. Interestingly, in the case of VBS1, a similar protocol for force-induced activation was simulated by Golji and Mofrad [161]– whose complex-building process we adapted here. However, the authors of this study did not find any weakening of the protein after VBS1-binding and subsequent force application. As the authors acknowledge, the conformational changes in vinculin relevant

for the activation are likely occur on the timescale of several micro seconds, whereas, at the time the study was published limited computational resources only permitted the sampling of several hundreds of picoseconds. Our VBS1-deletion simulations demonstrated that approximately 400 ns of simulation time were required to observe the structural rearrangement responsible for the variation in activation force, which led us to conclude that our extensive relaxation protocol after the construction of the complex allowed us to identify the entailed 'loosening' of the D1-tail interface.

Throughout our µs-long simulations of the VBS complexes, we did not observe any spontaneous opening events during which the D1-tail interface was lost completely without the presence of force. The locations of the actin binding sites on the vinculin tail, however, suggest that a complete opening of the protein is required for talin to bind completely. [24–26, 164]. Appendix figure A.8 illustrates how actin binding in the vinculin closed conformation is unlikely. Nonetheless, our experimental data (Figure 5.10) shows that VBS-bound vinculin, as well the VBS-mimicking mutants readily bind and bundle branched actin networks. This observation allows for two possible explanations. First, actin can form a pre-complex with VBS-bound vinculin and the electrostatic nature of the talin-vinculin interaction delivers the force to fully rupture the already weakened D1-tail interface. Second, VBS-binding leads to a wider ensemble of possible vinculin conformations with an increased likelihood for an opened conformation, a process that is known as 'molecular breathing' [165]. Rare events like this are unlikely to be sampled by unbiased MD simulations but can have important biological functions and implications. [166] Emerging enhanced sampling techniques offer an exciting prospect for future computational work in this direction. The two explanations are not mutually exclusive and possibly a combination of both effects is responsible for full vinculin activation.

In 2005, Cohen et al. [158] presented a mutagenesis study which systematically replaced clustered charged residues in the vinculin tail and evaluated their binding probability to vinculin head and actin. The low head-binding probability of the T12 mutant made the latter a widely used mutant in studies as 'open' vinculin. [167, 168] However, the T12 mutant affects mostly the D4-tail interface, not akin to the effect of VBS-binding. [44] We used force-probe MD simulation and correlated-motion analysis to suggest novel mutants that combine amino-acid substitutions that previously had only been investigated individually (T8, T13, T16 by Cohen et al. [158]). While neither of the T8, T13 and T16 mutants showed a decrease in head-tail binding probability, [158] the combination of these mutations works effectively together and allows for interactions with actin even in the absence of VBS1 (see figure 5.10). While earlier attempts to crystallize the open vinculin

conformation have not been successful [168], the novel mutants pose an interesting new opportunity for this, and, at the time of writing this thesis, efforts by the Medalia lab (University of Zürich) in this directions are in progress. Furthermore, cell experiments by the Geiger lab (Weizmann Institute, Israel) are underway probing the *in vitro* implication of our mutants.

Even though all our mutations are located on the tail domain, which is the actin-binding domain (see figure 5.1), interaction with actin was not hindered. On the contrary, actin-affinity was enhanced as bundling was stronger for all experiments involving the mutant when compared to WT vinculin (see figure 5.10). Also VBS1 binding is not negatively affected in the mutants; the additional binding of VBS1 led to stronger actin bundling for both mutants. This is in line with the idea that the tail domain and VBS compete for their interaction sites – even though they are located on opposing sides of the D1 domain [24, 44] and mutations shift the balance away from the tail. This leads to the interesting observation that binding of one of the two 'ligands' enhances the affinity for binding the other.

Our simulations demonstrated that the effect strength of different VBS can vary significantly (see figure 5.7). With a total of eleven VBS on the talin rod domain alone, which may all differ in their capability to weaken the vinculin D1-tail interface, this suggests that focal adhesions are finely regulated machines which react to mechanical cues in intricate ways. While, in terms of complexity, cellular adhesion sites surpass the models we used in this work vastly, our results provide intriguing new insights on vinculin activation and open the door to exiting further research using the here-presented mutants.

6

Summary and Conclusion

The goal of this thesis was to improve our understanding of the interaction and activation of talin and vinculin. We used equilibrium as well as force-probe molecular dynamics simulations to study the dynamics of these two prominent focal adhesion proteins on a molecular level. We further corroborated our findings with experiments carried out by several collaborators; Dr. Rafael Tapia-Rojo of the King's College London provided data from single-molecule magnetic tweezers experiments, and the Medalia lab at the University of Zürich supplemented findings from total internal reflection fluorescence microscopy. The proteins used in these experiments were manufactured by the Geiger lab and the Protein Production Unit at the Weizmann Institute of Science in Israel. Section 6.1 and figure 6.1 provide a summary of the key findings of this thesis in the context of focal adhesion maturation.

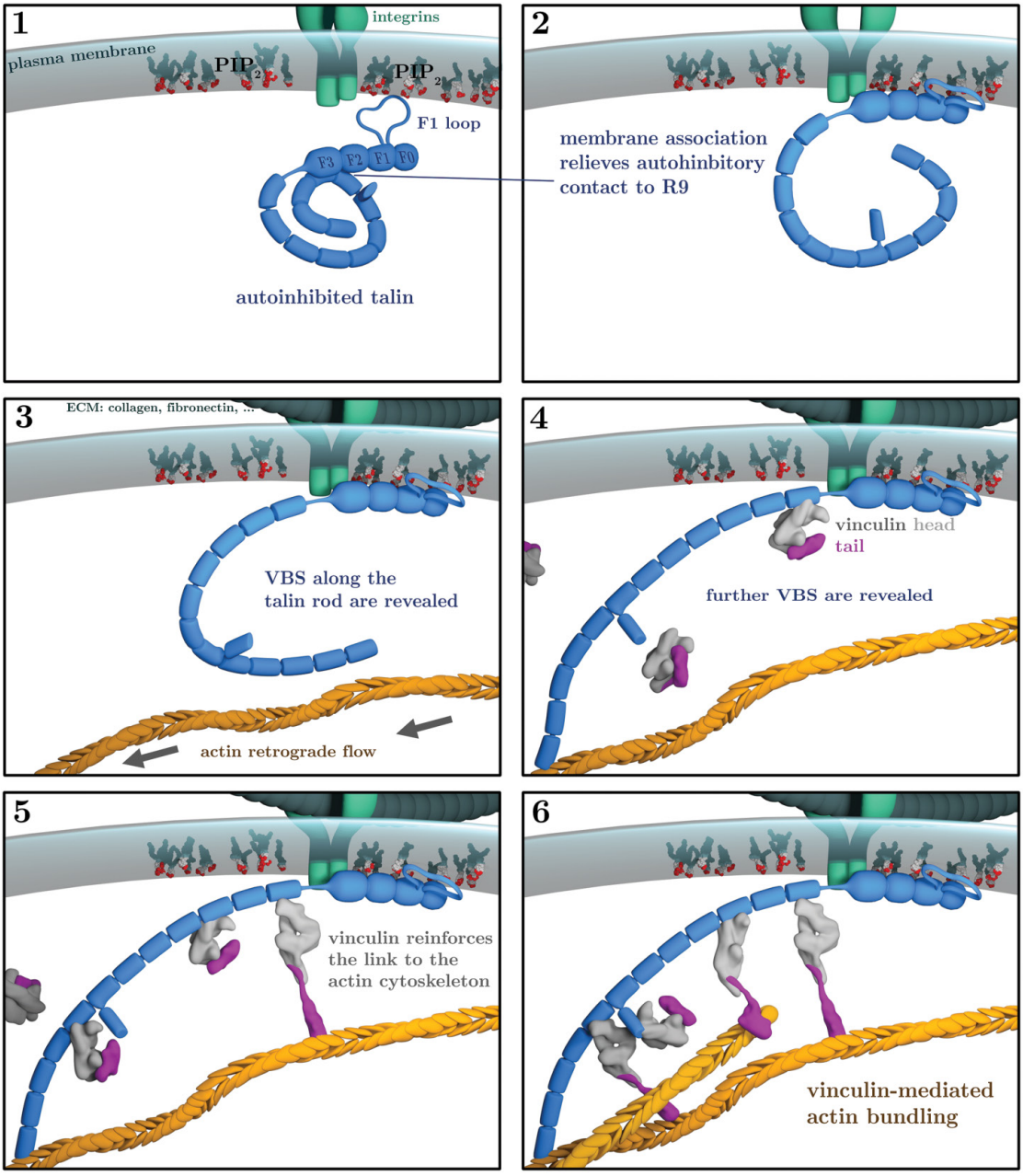

Figure 6.1.: Focal adhesion initiation and maturation. The key findings presented in this thesis are summarized in a six-step process of focal adhesion maturation.

6.1. Summary of the key findings in the context of focal adhesion maturation

Membrane-dependent talin activation

Step 1 in figure 6.1 depicts a cartoon of the closed talin protein. In the cytoplasm, the protein is autoinhibited and the known binding sites for PIP_2 (F2,F3), integrins (F3), and vinculin (along the rod) are not active. [56, 57] In chapter 3, we propose a mechanism by which the flexible loop in on the talin FERM domain poses an initial contact site that allows for and facilitates further PIP_2 interaction. Our extensive computational efforts demonstrate that the loop is a highly flexible region that – independent of the starting conformation – encounters and binds to PIP_2. Subsequently, this first contact leads to more pronounced PIP_2 interactions with additional FERM subdomains. The findings corroborate our hypothesis in which talin can be activated in a PIP_2-mediated way (step 2 in figure 6.1). Experimental findings [42] that were published while this project was underway also support this hypothesis by showing that the presence of PIP_2-containing membranes is sufficient to promote further interactions of talin with other proteins such as vinculin. With force-probe MD simulations, we then investigated the role of the increased PIP_2 concentrations at focal adhesions [36] and found that the resistance to lateral displacement was greatly increased compared to a small PIP_2 abundance. Our findings highlight the multi-purpose role of PIP_2, as it can not only mediate talin activation but also localizes the protein to the adhesion site.

Dynamics of the talin-vinculin interaction

Numerous vinculin binding sites [58] are buried in helix bundles along the rod domain of talin. [43] An activated, membrane-associated talin may bind to actin filaments in the retrograde flow giving rise to a force over the protein which, in turn, reveals VBS, as illustrated by steps 3 and 4 in figure 6.1. In chapter 4, we set out to study the force-dependent dynamics of the vinculin-talin interaction. Force-probe MD simulations on the VBS1 peptide showed a dynamic coexistence of coiled and helical states. Of the here-investigated VBS, VBS1 shows the highest sequence identity with VBS11 which is located in the talin R3 domain and undergoes a coil-to-helix transition in magnetic tweezers experiments. [59] The experimentally measured contraction matched the one observed in the simulated conformational ensemble very well. This led us to conclude that the very force-sensitive co-existence of helical and coiled states is essential for vinculin binding. We further identified the residues in the vinculin D1 domain involved in a competition mechanism between VBS1 and the vinculin tail domain on opposing faces of the vinculin head domain. Our simulations showed a reduction in resistance against

mechanical unfolding of VBS1, and magnetic tweezers experiments confirmed a lower binding probability at higher forces across the VBS-containing talin domain (Tapia-Rojo, unpublished). Interestingly, the competition works both ways and binding of VBS1 does also facilitate the disruption of the vinculin head-tail interface as illustrated in step 4 of figure 6.1. The D1 residues involved in the competition mechanism interact with parts of the vinculin tail domain that – according to the findings presented in chapter 5 of this thesis – are responsible for a significant decrease in the activation force of vinculin.

Talin-dependent vinculin activation

Step 5 of figure 6.1 displays how vinculin reinforces the link to the actin cytoskeleton. [115, 150, 152] In chapter 5, we found that the binding of different talin VBS to vinculin is a prerequisite for this reinforcement, as otherwise the vinculin tail is attached very strongly to the D1 domain. We combined force distribution analysis [109] and generalized correlated motions [107] to pinpoint the head-tail interactions which were most weakened by VBS-binding. The introduction of mutations on vinculin tail residues involved in this interaction led to two novel vinculin mutants that intend to specifically mimic the effect of talin-association. TIRFM experiments (Boujemaa-Paterski, unpublished) confirmed that both our mutants can initiate the bundling of branched actin networks. Wild-type vinculin bundles actin networks only in the presence of a VBS-containing talin fragment. [163] Actin bundles are the precursor for force-bearing stress fibres which are necessary for focal adhesion maturation and mechanotransduction. [169] With the actin binding sites being cryptic and located on the vinculin tail [24–26], these findings suggests that the novel mutants do weaken the head-tail interface as intended. These promising results suggest the computationally designed mutants to be an invaluable tool to study vinculin function *in vitro* and *in vivo*.

6.2. Closing thoughts and future directions

Taken together, the findings presented in this thesis further our understanding of the activation processes of two principal focal adhesion proteins, talin in vinculin. We provided insights into the molecular mechanisms by which the cellular membrane aids to relieve the talin inhibition which, in turn, recruits and activates the versatile signalling hub vinculin.

While the summary of the key findings in section 6.1 is focused on focal adhesion maturation, the results of this thesis may also have implications for FA disassembly.

In chapter 4, we revealed that different talin VBS show varying resistances to force-mediated unbinding from vinculin, which points towards a force-sensitive hierarchical FA dismantling. This underlines that both, FA assembly and disassembly, are highly force-regulated processes which are able to react precisely to minimal mechanical cues. Naturally, given the magnitude of the number of different proteins involved in cellular adhesions, our findings only represent a small piece of the vastly complex puzzle that are focal adhesions.

We are confident that the novel vinculin mutants we proposed provide the means to gather further insights on the interplay between talin and vinculin. With cell experiments by the Geiger lab (Weizmann Institute of Science, Israel) and cryo-EM efforts by the Medalia lab (University of Zürich) underway, further data on the mutants will soon be available. In terms of MD simulations, emerging enhanced sampling methods present exciting new possibilities. [132] Classical MD failed to sample the binding and contraction of tensed VBS peptide within the vinculin binding pocket, which constitutes an interesting direction for future efforts. Also coarse-grained modelling of protein and in particular protein-membrane interactions [170] are coming of age, allowing to extend simulations to larger and more complex multi-component systems such as a membrane-bound talin molecule with more than one vinculin bound to its rod domain will become accessible – eventually even on an atomistic scale. [171, 172]

The thesis highlights that simulation-generated hypothesis tested by subsequent experiments on the single-molecule and cellular scale can advance our knowledge on questions as complex as mechanosensation at cellular adhesions.

A

Appendix

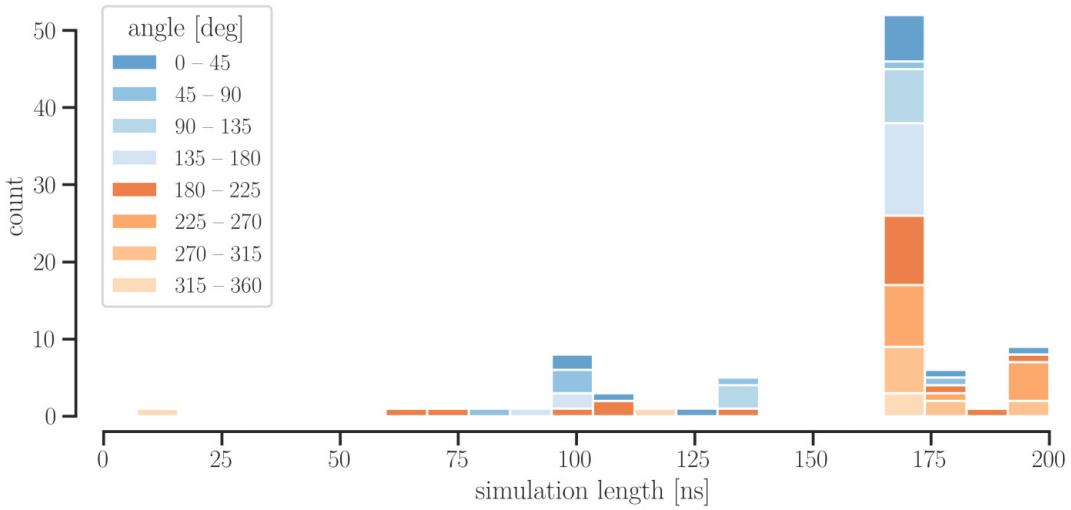

Figure A.1.: Trajectory lengths are independent from the staring position of the F0F1 domain. Due to HPC problems, a few simulations in the rotational sampling stopped before completing the planned 200 ns. This figure shows that most simulations did complete at least 170 ns and that there is no bias towards any particular orientation.

Table A.1.: One-to-many interactions of PIP2 molecules with the FERM domain. Residues or clusters of residues that are in contact with an individual PIP2. Counts refers to the number of frames in which these interaction were observed, where we consider one frame per nanosecond. Data was collected form 6 simulations with 400 ns-length each.

$n = 1$	**Counts**	$n = 2$	**Counts**	$n \geq 3$	**Counts**
K147	641	G275, K272	586	K160, L151, T144	190
K320	579	K320, K322	493	G321, K316, K320	180
D341	468	K160, T144	331	G321, K320, K322	161
M158	435	G275, K254	292	K15, R35, T16	104
S362	431	K160, M158	278	K147, K15, R35, T16	87
K160	361	L314, S362	270	D261, K272, Y270	82
K322	339	E155, M158	157	K147, K160, T144	81
M1	319	E155, T144	119	K162, L145, L151, R74	75
Y270	311	D154, E155	114	E155, K160, T144	71
R35	243	K162, M158	81	K160, L151, M158, T144	66
D154	229	K272, Y270	79	D148, E155, K147, R146, T144	63
L314	228	K316, S362	72	G321, K320, K322, M319	58
E155	218	L151, T144	68	L145, L151, R74	42
L145	218	K15, T16	66	K157, K160, M158	39
R74	214	G321, K320	64	K316, S362, S379	37
T144	196	L151, R74	62	K316, N323, S362, S379	37
K272	184	K318, K320	58	L314, N323, S362	30
K316	158	D341, K322	55	K160, K162, M158	28
K162	122	G321, K316	47	L151, M158, T144	24
G275	115	K15, R35	47	K160, L161, M158	23
K7	82	K160, L161	47	E155, K162, L145, L151, R74	22
K254	70	D261, Y270	39	K316, K318, K320	22
L266	55	K322, L314	37	G321, K320, M319	21
K318	48	L145, L151	36	E155, K162, L145, L151, L161, R74	20
G321	47	D261, K272	35	L145, L151, T144	18
D261	27	K316, K318	30	E155, K147, R146, T144	18
E136	21	M1, V2	28	G321, K316, K318, K320	17
K15	19	D148, K147	28	L314, Q381, S362	17
L151	13	E155, K147	28	G321, K316, K320, S362	17
V271	10	D341, Y270	27	K147, K15, T16	17
L325	7	K160, K162	24	K316, N323, S362	16
T16	6	G321, K322	22	E159, K160, L161, M158	15
Q18	4	K316, K320	22	K318, K320, M319	14
V326	3	L266, Y270	20	L314, S362, S379	14
M319	3	D261, K160	19	G321, K316, K320, M319	11
K256	3	K7, T16	17	N323, S362, S379	11
N75	3	K320, M319	16	G321, K316, S362	11
N323	2	D148, E155	14	K15, K7, T16	10
R146	2	S362, S379	14	K316, L314, N323, S362, S379	10
K164	2	D341, K320	13	K316, L314, S362, S379	10
Q381	2	D261, L266	12	K162, L151, R74	10
L161	1	G321, S362	11	D154, L145, L151	9
K156	1	K254, Q253	11	E155, L151, M158	9
E20	1	L314, N323	11	E155, L151, R74	8
V2	1	K322, N323	10	E155, L152, T144	7
N12	1	K157, M158	10	G321, K316, S362, S379	7
A3	1	K147, L145	10	L314, N323, S362, S379	7
V14	1	D341, V271	9	K15, K7, T16, V14	7
P37	1	K272, V271	8	D148, E155, K147, L152, R146, T144	7
F312	1	K147, R146	8	E269, L266, Y270	6
H255	1	E136, M158	8	G321, K322, N323	6

Table A.2.: One-to-many interactions of PIP2 molecules with the crystal structure (pdb: 6MFS, [57]) of the talin FERM domain. Residues or clusters of residues that are in contact with an individual PIP2. Counts refers to the number of frames in which these interaction were observed, where we consider one frame per nanosecond. Data was collected form 8 simulations with 1 µs-length each. Starting point was the PIP2-bound crystal structure of Chinthalapudi et al. [57]

$n = 1$	Counts	$n = 2$	Counts	$n \geq 3$	Counts
K320	2449	G275, K272	2605	G321, K320, K322	1098
S362	2354	K320, K322	1981	K322, L314, N323	482
K322	1525	I356, N355	994	G321, K316, K318, M319	335
Y270	1167	K98, R118	972	K316, K318, M319	294
I356	920	L314, S362	648	D261, K272, Y270	284
G275	802	K15, R35	477	K316, K318, K320	212
K318	755	G321, K322	387	K322, L314, N323, S362	172
L266	672	A360, S362	254	A282, G275, K254	150
R74	643	D261, Y270	230	L314, N323, S362	148
L314	556	K316, K318	219	G321, K320, K322, M319	127
K272	495	L314, N323	193	A257, G275, K256	123
E252	399	G275, K254	190	K15, K7, T16	109
D341	391	K322, L314	171	A360, A361, S362	95
N355	356	G321, K320	167	E252, K254, R91	84
K7	308	K272, Y270	155	K254, K89, R91	81
K254	174	E252, K254	142	K316, P363, S362, S379	80
D261	159	A282, G275	128	G275, K254, Q253	71
K98	145	D261, K272	115	A360, P363, S362	68
K316	142	K254, R91	107	A282, G275, I279	64
G321	137	E252, G275	102	A282, E252, G275	63
K137	75	L266, Y270	91	L314, Q381, S362	58
K15	62	K15, T16	91	E252, H255, K254, R91	49
W359	51	E276, G275	86	A360, P363, S362, S379	44
R118	44	K316, S362	83	G321, K316, K318, K320, M319	43
A257	44	D341, K322	79	K322, N323, S362	43
T16	41	K318, K320	77	D375, K316, K318, K320	41
Q253	37	G321, K316	63	K15, R35, V13	40
M319	26	D375, I356	59	G321, K316, S362	39
A360	25	K316, K320	54	G321, K316, K318	38
A282	23	E252, R91	47	K316, S362, S379	37
K89	18	K254, K89	40	D375, K316, K318	36
N75	18	K318, M319	40	K254, R91, V97	34
A361	18	K320, M319	34	G321, K316, K320	33
F259	18	P363, S362	33	H188, K254, K89, R91	32
N323	16	R358, W359	29	A282, G275, Q253	28
T96	16	E269, Y270	27	P363, S362, S379	27
N251	15	D341, K272	27	L314, S362, S379	27
M1	13	E252, Q253	24	A282, G275, I279, K254	26
R91	12	A257, G275	23	K15, R35, T16	23
D375	9	K7, T16	23	G275, K272, Y270	22
E276	9	G275, I279	21	K316, P363, S362	22
Q18	9	G275, K256	21	A360, A361, P363, S362	21
Q381	8	D341, V271	20	D261, F259, K272, Y270	21
L262	7	N323, S362	20	L314, N323, S379	20
R358	6	S362, S379	19	G275, K272, K274	19
S379	6	A361, S362	18	K254, K89, R91, V97	19
T122	5	G321, S362	18	D369, I356, N355	19
G76	4	D341, L325	16	H188, K254, K89	18
V14	4	D375, K318	16	K320, K322, N323	18
D54	4	Q381, S362	15	E252, K254, K89, R91	18
K256	4	D261, L266	14	D261, E269, Y270	17

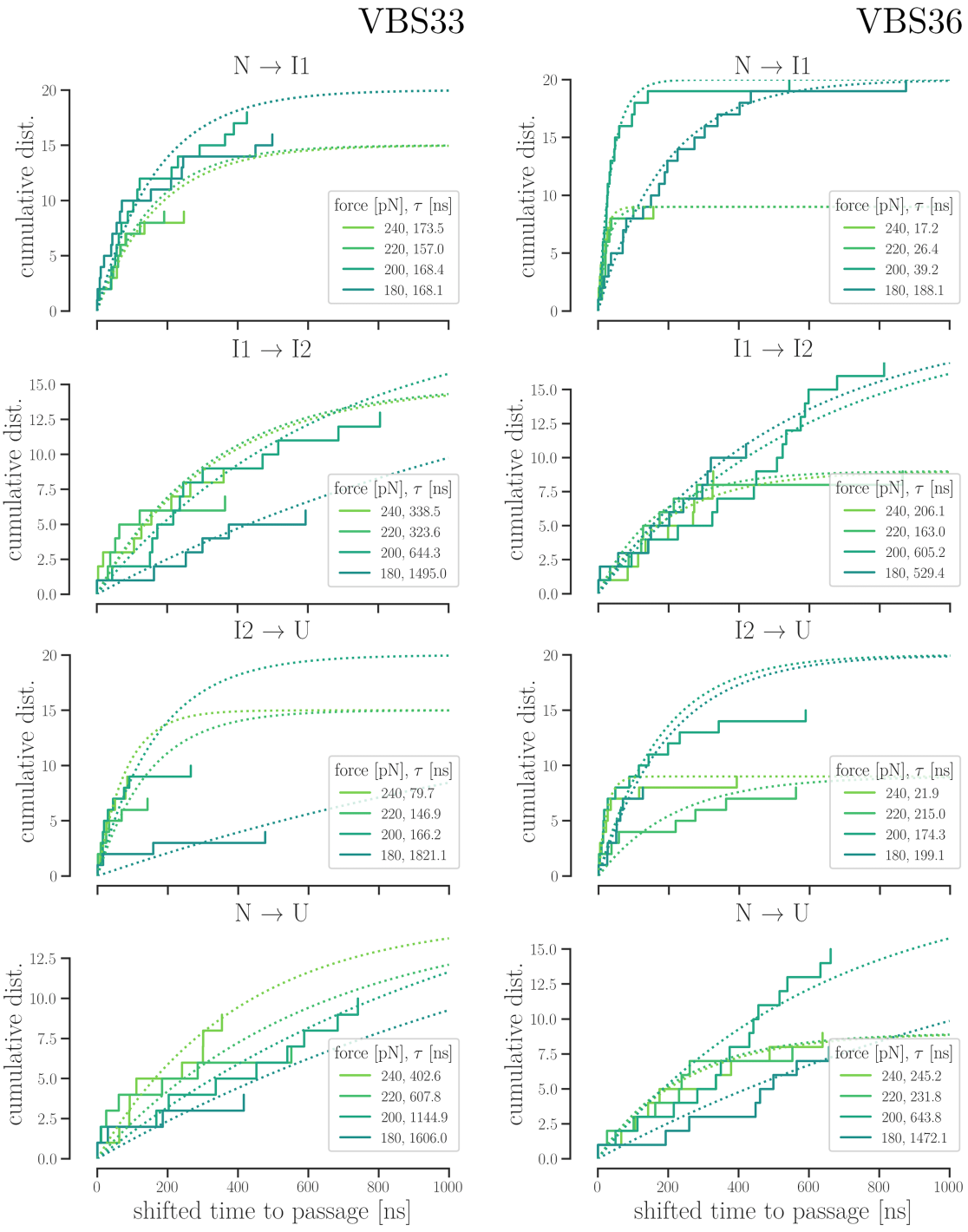

Figure A.2.: VBS33 and VBS36 unfolding. Cumulative distributions of shifted dwell times for VBS33 and VBS36 unfolding. Data was fit to $N * (1 - e^{-(x/\tau)})$ which is depicted as dotted lines. Note, that not for all force / topology combinations the full 20 trajectories were available. In these cases N is adjusted accordingly to preserve the validity of the analysis.

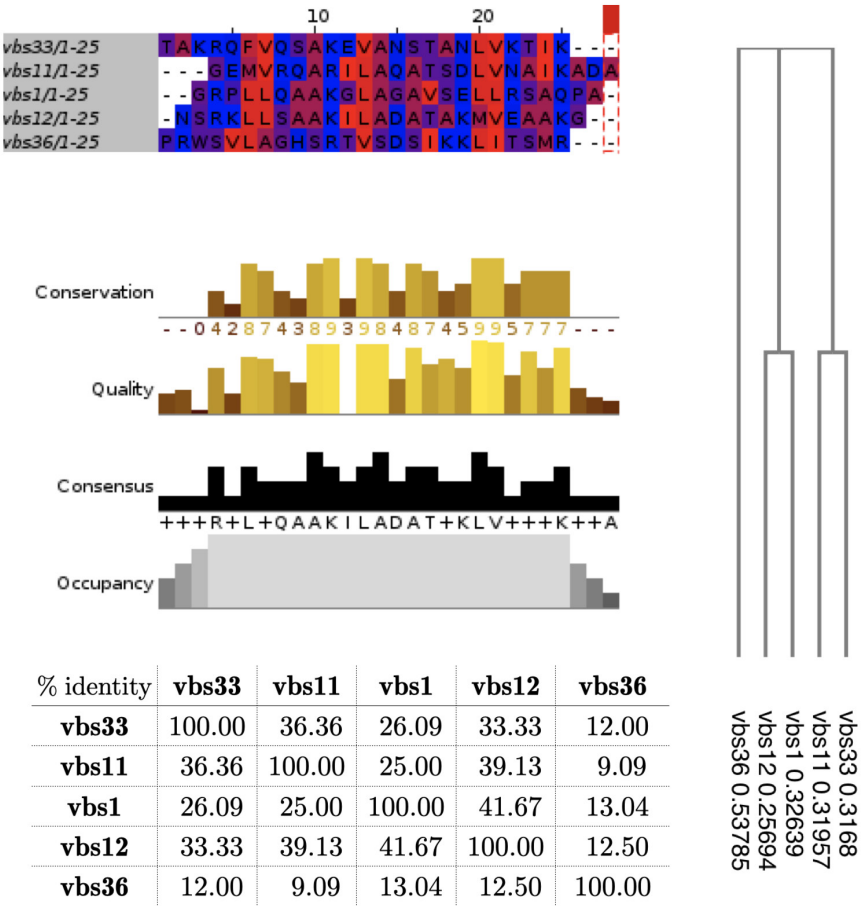

% identity	**vbs33**	**vbs11**	**vbs1**	**vbs12**	**vbs36**
vbs33	100.00	36.36	26.09	33.33	12.00
vbs11	36.36	100.00	25.00	39.13	9.09
vbs1	26.09	25.00	100.00	41.67	13.04
vbs12	33.33	39.13	41.67	100.00	12.50
vbs36	12.00	9.09	13.04	12.50	100.00

Figure A.3.: Sequence alignment of VBS1, VBS11, VBS12, VBS33, and VBS36. The figure was generated with the Clustal Omega webservice. [142]

Table A.3.: Force-induced vinculin activation. The table shows the statistics of the rupture forces observed for the different vinculin-VBS complexes as well as for the apo-state protein. The 'count' column shows the number of trajectories that were available for each class.

topology	velocity [m/s]	count	mean [pN]	std [pN]	min [pN]	25% [pN]	50% [pN]	75% [pN]	max [pN]
APO	0.01	3	550.8	18.8	532.8	541.1	549.4	559.8	570.2
	0.03	8	636.8	60.4	538.3	607.2	644.2	673.6	711.2
	0.1	30	744.9	88.3	571.5	685.9	744.7	782.2	950.3
	0.3	8	926.7	29.1	862.4	923.3	929.7	943.9	960.2
ACT	0.03	10	590.7	91.8	398.5	548.9	599.2	630.8	711.7
	0.1	20	759.9	82.9	603.6	714.0	753.0	793.9	931.6
VBS3	0.03	10	506.1	74.9	399.4	446.1	516.0	572.2	607.3
	0.1	20	644.1	97.2	456.2	567.8	652.6	713.8	809.5
VBS1	0.03	30	390.8	77.2	248.2	341.5	379.1	442.6	543.2
	0.1	60	445.6	61.9	298.4	406.9	443.0	488.6	590.1
VBS1	0.01	3	388.7	106.0	316.6	327.9	339.1	424.8	510.5
force on	0.03	3	305.4	9.4	297.9	300.1	302.3	309.1	316.0
peptide	0.1	5	367.7	27.5	337.8	354.6	366.3	368.0	411.9
	0.3	2	492.0	55.0	453.2	472.6	492.0	511.5	530.9

Table A.4.: Activation forces of the VBS1-deletion structures. The table shows the statistics of the rupture forces observed for the VBS1-deletion structure after four independent equilibration simulations. The 'count' column shows the number of data points going into the displayed statistcs.

Eq. run	velocity [m/s]	count	mean [pN]	std [pN]	min [pN]	25% [pN]	50% [pN]	75% [pN]	max [pN]
1	0.1	10	915.3	150.1	729.8	813.2	869.8	1007.5	1182.8
2	0.1	10	870.2	67.2	766.3	833.0	872.1	889.4	993.3
3	0.1	10	860.8	118.9	660.9	816.6	873.9	950.6	1004.4
4	0.1	10	862.2	90.7	640.6	850.1	888.2	918.8	936.9

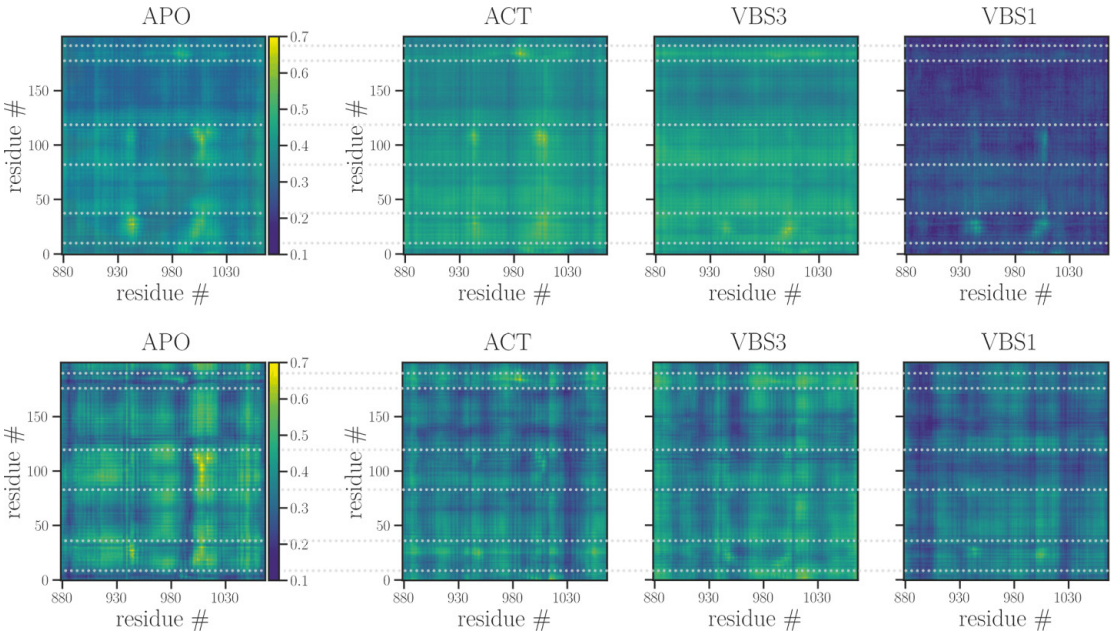

Figure A.4.: Generalized correlation maps of the D1-tail interface. As an extension to figure 5.8, the top row shows the correlations gathered from the pulling trajectories using the 5 ns leading up the the respective rupture event. The bottom row shows the correlations calculated from the last 100 ns of the unbiased equilibration simulations.

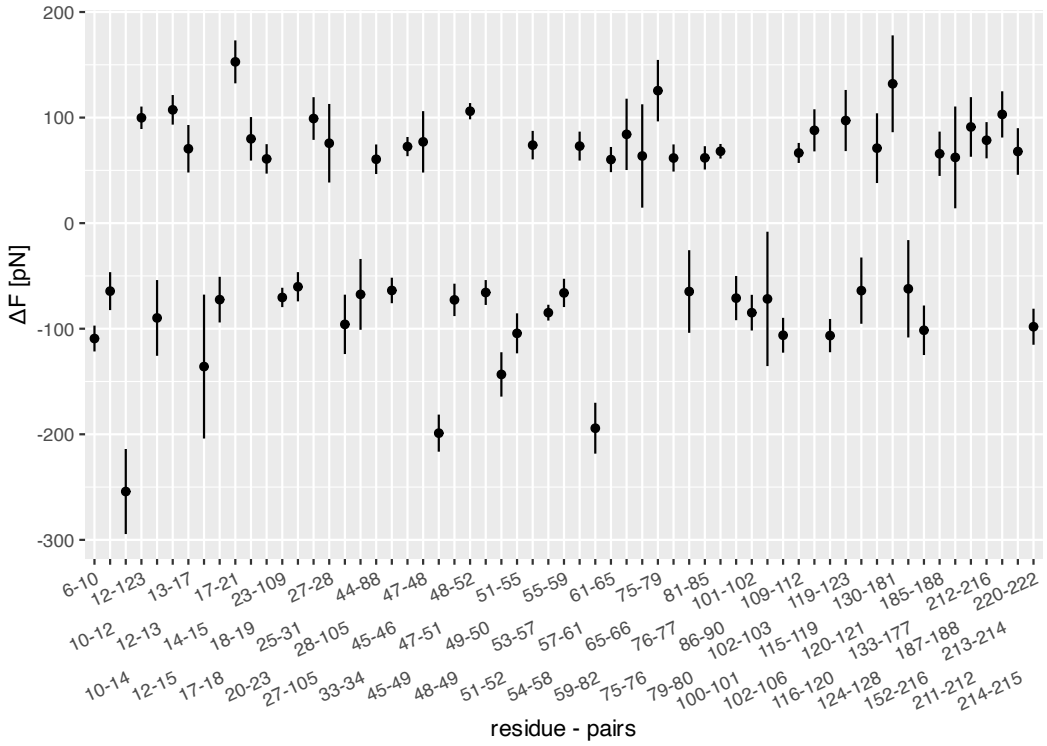

Figure A.5.: FDA raw data: D1 intradomain force differences. All residue pairs that experience a shift in experienced pair-wise force of over 60 pN within the D1 domain are shown. The error bars indicate the respective standard deviations.

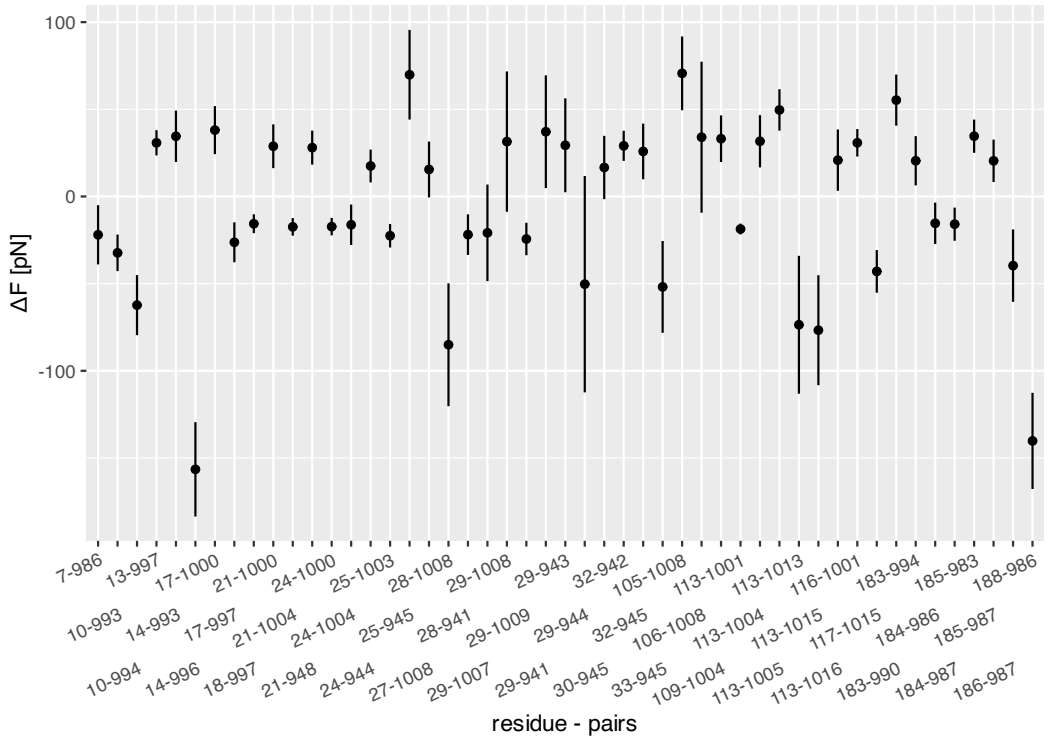

Figure A.6.: FDA raw data: D1-tail force differences. All residue pairs that experience a shift in experienced pair-wise force of over 30 pN within the D1-tail interface are shown. The error bars indicate the respective standard deviations.

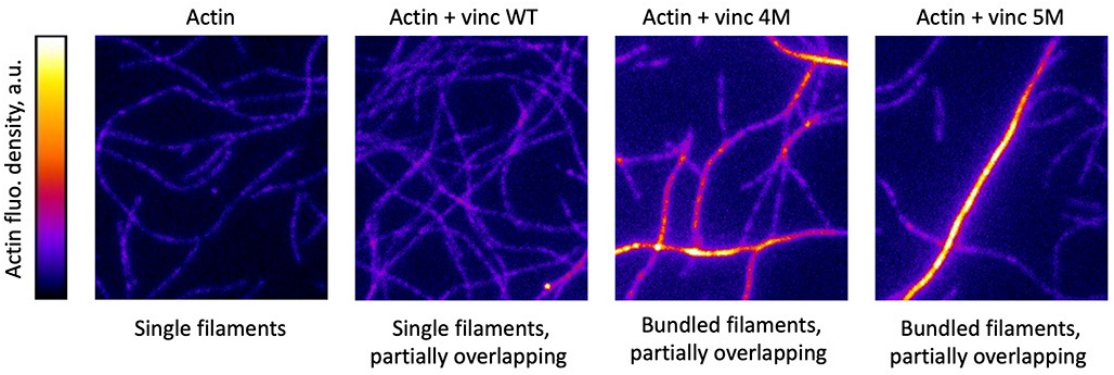

Figure A.7.: Vinculin / actin interaction in the absence of talin–VBS1. TIRFM quantification of actin bundles after 1 hour of actin assembly. Images were provided by Dr. Rajaa Boujemaa-Paterski from the Medalia lab at the University of Zürich.

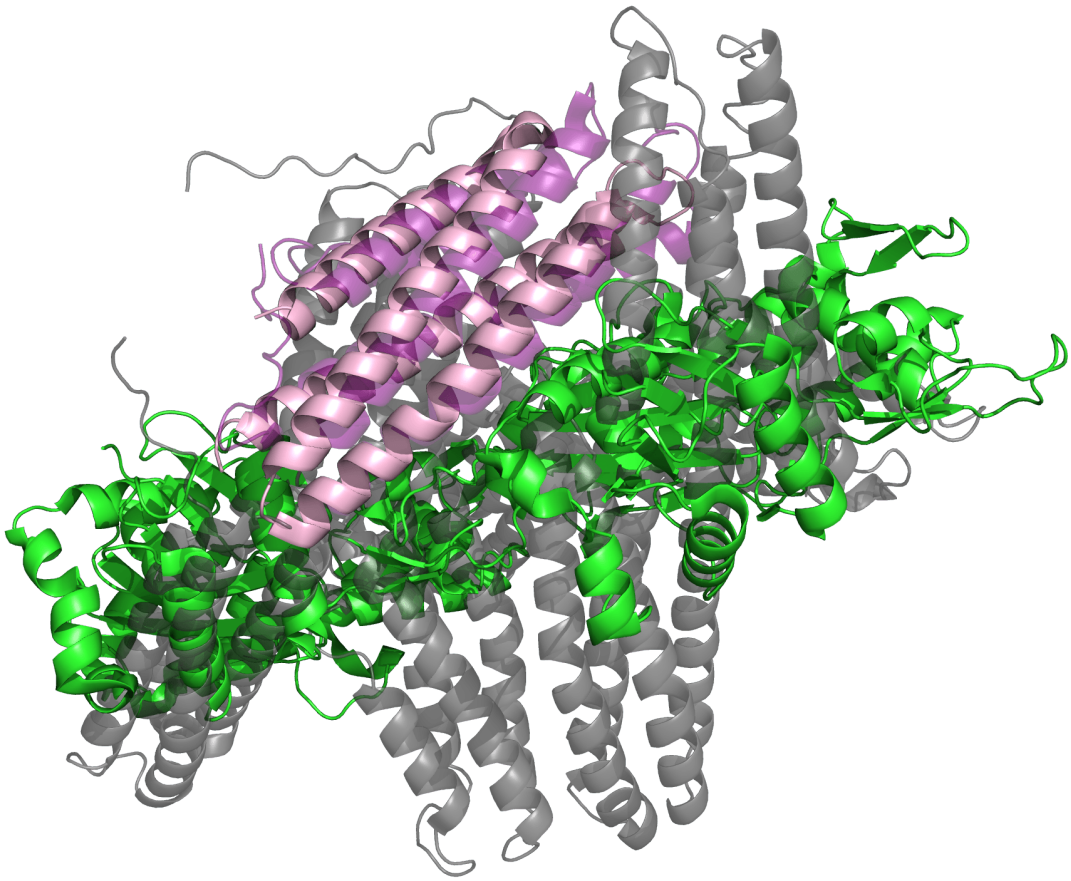

Figure A.8.: Actin binding is not possible in the closed vinculin conformation. The molecular dynamics flexible fitting model by Kim et al. [164] of the vinculin tail (purple cartoon) bound to actin (green cartoon) was aligned to the closed full-length vinculin crystal structure [160] (shown as transparent cartoon) with respect to the tail domains using pymol.

Bibliography

[1] Geiger, B.; Spatz, J. P.; Bershadsky, A. D. Environmental Sensing through Focal Adhesions. *Nature Reviews Molecular Cell Biology* **2009**, *10*, 21–33.

[2] Fernàndez-Busquets, X.; Burger, M. M. Cell Adhesion and Histocompatibility in Sponges. *Microscopy Research and Technique* **1999**, *44*, 204–218.

[3] Geiger, B.; Yamada, K. M. Molecular Architecture and Function of Matrix Adhesions. *Cold Spring Harbor Perspectives in Biology* **2011**, *3*, a005033.

[4] Smith, L.; Cho, S.; Discher, D. E. Mechanosensing of Matrix by Stem Cells: From Matrix Heterogeneity, Contractility, and the Nucleus in Pore-Migration to Cardiogenesis and Muscle Stem Cells in Vivo. *Seminars in Cell & Developmental Biology* **2017**, *71*, 84–98.

[5] Martino, F.; Perestrelo, A. R.; Vinarský, V.; Pagliari, S.; Forte, G. Cellular Mechanotransduction: From Tension to Function. *Frontiers in Physiology* **2018**, *0*.

[6] Budday, S.; Nay, R.; de Rooij, R.; Steinmann, P.; Wyrobek, T.; Ovaert, T. C.; Kuhl, E. Mechanical Properties of Gray and White Matter Brain Tissue by Indentation. *Journal of the mechanical behavior of biomedical materials* **2015**, *46*, 318–330.

[7] Rho, J. Y.; Ashman, R. B.; Turner, C. H. Young's Modulus of Trabecular and Cortical Bone Material: Ultrasonic and Microtensile Measurements. *Journal of Biomechanics* **1993**, *26*, 111–119.

[8] del Rio, A.; Perez-Jimenez, R.; Liu, R.; Roca-Cusachs, P.; Fernandez, J. M.; Sheetz, M. P. Stretching Single Talin Rod Molecules Activates Vinculin Binding. *Science* **2009**, *323*, 638–641.

[9] Bertocchi, C.; Vaman Rao, M.; Zaidel-Bar, R. Regulation of Adherens Junction Dynamics by Phosphorylation Switches. *Journal of Signal Transduction* **2012**, *2012*, 125295.

[10] Golji, J.; Wendorff, T.; Mofrad, M. R. K. Phosphorylation Primes Vinculin for Activation. *Biophysical Journal* **2012**, *102*, 2022–2030.

[11] Dupont, S.; Morsut, L.; Aragona, M.; Enzo, E.; Giulitti, S.; Cordenonsi, M.; Zanconato, F.; Le Digabel, J.; Forcato, M.; Bicciato, S.; Elvassore, N.; Piccolo, S. Role of YAP/TAZ in Mechanotransduction. *Nature* **2011**, *474*, 179–183.

[12] Klapholz, B.; Brown, N. H. Talin - the Master of Integrin Adhesions. *Journal of Cell Science* **2017**, *130*, 2435–2446.

[13] Martinac, B.; Nomura, T.; Chi, G.; Petrov, E.; Rohde, P. R.; Battle, A. R.; Foo, A.; Constantine, M.; Rothnagel, R.; Carne, S.; Deplazes, E.; Cornell, B.; Cranfield, C. G.; Hankamer, B.; Landsberg, M. J. Bacterial Mechanosensitive Channels: Models for Studying Mechanosensory Transduction. *Antioxidants & Redox Signaling* **2014**, *20*, 952–969.

[14] Alonso, J. L.; Goldmann, W. H.; Alonso, J. L.; Goldmann, W. H. Cellular Mechanotransduction. *AIMS Biophysics* **2016**, *3*, 50–62.

[15] Zaidel-Bar, R.; Itzkovitz, S.; Ma'ayan, A.; Iyengar, R.; Geiger, B. Functional Atlas of the Integrin Adhesome. *Nature Cell Biology* **2007**, *9*, 858–867.

[16] Horton, E. R.; Byron, A.; Askari, J. A.; Ng, D. H. J.; Millon-Frémillon, A.; Robertson, J.; Koper, E. J.; Paul, N. R.; Warwood, S.; Knight, D.; Humphries, J. D.; Humphries, M. J. Definition of a Consensus Integrin Adhesome and Its Dynamics during Adhesion Complex Assembly and Disassembly. *Nature Cell Biology* **2015**, *17*, 1577–1587.

[17] Horton, E. R.; Humphries, J. D.; James, J.; Jones, M. C.; Askari, J. A.; Humphries, M. J. The Integrin Adhesome Network at a Glance. *Journal of Cell Science* **2016**, *129*, 4159–4163.

[18] Discher, D. E.; Janmey, P.; Wang, Y.-l. Tissue Cells Feel and Respond to the Stiffness of Their Substrate. *Science* **2005**, *310*, 1139–1143.

[19] Nobes, C. D.; Hall, A. Rho, Rac, and Cdc42 GTPases Regulate the Assembly of Multimolecular Focal Complexes Associated with Actin Stress Fibers, Lamellipodia, and Filopodia. *Cell* **1995**, *81*, 53–62.

[20] Choi, C. K.; Vicente-Manzanares, M.; Zareno, J.; Whitmore, L. A.; Mogilner, A.; Horwitz, A. R. Actin and α-Actinin Orchestrate the Assembly and Maturation of Nascent Adhesions in a Myosin II Motor-Independent Manner. *Nature Cell Biology* **2008**, *10*, 1039–1050.

[21] Zaidel-Bar, R.; Ballestrem, C.; Kam, Z.; Geiger, B. Early Molecular Events in the Assembly of Matrix Adhesions at the Leading Edge of Migrating Cells. *Journal of Cell Science* **2003**, *116*, 4605–4613.

[22] Humphries, J. D.; Wang, P.; Streuli, C.; Geiger, B.; Humphries, M. J.; Ballestrem, C. Vinculin Controls Focal Adhesion Formation by Direct Interactions with Talin and Actin. *The Journal of Cell Biology* **2007**, *179*, 1043–1057.

[23] Galbraith, C. G.; Yamada, K. M.; Sheetz, M. P. The Relationship between Force and Focal Complex Development. *The Journal of Cell Biology* **2002**, *159*, 695–705.

[24] Janssen, M. E. W.; Kim, E.; Liu, H.; Fujimoto, L. M.; Bobkov, A.; Volkmann, N.; Hanein, D. Three-Dimensional Structure of Vinculin Bound to Actin Filaments. *Molecular cell* **2006**, *21*, 271–281.

[25] Golji, J.; Mofrad, M. R. K. The Interaction of Vinculin with Actin. *PLOS Computational Biology* **2013**, *9*, e1002995.

[26] Thompson, P. M.; Tolbert, C. E.; Shen, K.; Kota, P.; Palmer, S. M.; Plevock, K. M.; Orlova, A.; Galkin, V. E.; Burridge, K.; Egelman, E. H.; Dokholyan, N. V.; Superfine, R.; Campbell, S. L. Identification of an Actin Binding Surface on Vinculin That Mediates Mechanical Cell and Focal Adhesion Properties. *Structure* **2014**, *22*, 697–706.

[27] Carisey, A.; Tsang, R.; Greiner, A. M.; Nijenhuis, N.; Heath, N.; Nazgiewicz, A.; Kemkemer, R.; Derby, B.; Spatz, J.; Ballestrem, C. Vinculin Regulates the Recruitment and Release of Core Focal Adhesion Proteins in a Force-Dependent Manner. *Current biology: CB* **2013**, *23*, 271–281.

[28] Kanchanawong, P.; Shtengel, G.; Pasapera, A. M.; Ramko, E. B.; Davidson, M. W.; Hess, H. F.; Waterman, C. M. Nanoscale Architecture of Integrin-Based Cell Adhesions. *Nature* **2010**, *468*, 580–584.

[29] Case, L. B.; Baird, M. A.; Shtengel, G.; Campbell, S. L.; Hess, H. F.; Davidson, M. W.; Waterman, C. M. Molecular Mechanism of Vinculin Activation and Nanoscale Spatial Organization in Focal Adhesions. *Nature Cell Biology* **2015**, *17*, 880–892.

[30] Tong, X.; James Jiang,; Zhu, D.; Yang, F. Hydrogels with Dual Gradients of Mechanical and Biochemical Cues for Deciphering Cell-Niche Interactions. *ACS Biomaterials Science & Engineering* **2016**, *2*, 845–852.

[31] Stutchbury, B.; Atherton, P.; Tsang, R.; Wang, D.-Y.; Ballestrem, C. Distinct Focal Adhesion Protein Modules Control Different Aspects of Mechanotransduction. *Journal of Cell Science* **2017**, *130*, 1612–1624.

[32] Wolfenson, H.; Lubelski, A.; Regev, T.; Klafter, J.; Henis, Y. I.; Geiger, B. A Role for the Juxtamembrane Cytoplasm in the Molecular Dynamics of Focal Adhesions. *PLOS ONE* **2009**, *4*, e4304.

[33] Lombard, J. Once upon a Time the Cell Membranes: 175 Years of Cell Boundary Research. *Biology Direct* **2014**, *9*, 32.

[34] Quehenberger, O.; Dennis, E. A. The Human Plasma Lipidome. *The New England journal of medicine* **2011**, *365*, 1812–1823.

[35] Yin, H. L.; Janmey, P. A. Phosphoinositide Regulation of the Actin Cytoskeleton. *Annual Review of Physiology* **2003**, *65*, 761–789.

[36] Chong, L. D.; Traynor-Kaplan, A.; Bokoch, G. M.; Schwartz, M. A. The Small GTP-Binding Protein Rho Regulates a Phosphatidylinositol 4-Phosphate 5-Kinase in Mammalian Cells. *Cell* **1994**, *79*, 507–513.

[37] Lassing, I.; Lindberg, U. Specific Interaction between Phosphatidylinositol 4,5-Bisphosphate and Profilactin. *Nature* **1985**, *314*, 472–474.

[38] Moore, D. T.; Nygren, P.; Jo, H.; Boesze-Battaglia, K.; Bennett, J. S.; DeGrado, W. F. Affinity of Talin-1 for the *B*3-Integrin Cytosolic Domain Is Modulated by Its Phospholipid Bilayer Environment. *Proceedings of the National Academy of Sciences* **2012**, *109*, 793–798.

[39] Wiseman, P. W.; Brown, C. M.; Webb, D. J.; Hebert, B.; Johnson, N. L.; Squier, J. A.; Ellisman, M. H.; Horwitz, A. F. Spatial Mapping of Integrin Interactions and Dynamics during Cell Migration by Image Correlation Microscopy. *Journal of Cell Science* **2004**, *117*, 5521–5534.

[40] Grashoff, C.; Hoffman, B. D.; Brenner, M. D.; Zhou, R.; Parsons, M.; Yang, M. T.; McLean, M. A.; Sligar, S. G.; Chen, C. S.; Ha, T.; Schwartz, M. A. Measuring Mechanical Tension across Vinculin Reveals Regulation of Focal Adhesion Dynamics. *Nature* **2010**, *466*, 263–266.

[41] Kumar, A.; Ouyang, M.; Van den Dries, K.; McGhee, E. J.; Tanaka, K.; Anderson, M. D.; Groisman, A.; Goult, B. T.; Anderson, K. I.; Schwartz, M. A. Talin Tension Sensor Reveals Novel Features of Focal Adhesion Force Transmission and Mechanosensitivity. *The Journal of Cell Biology* **2016**, *213*, 371–383.

[42] Kelley, C. F.; Litschel, T.; Schumacher, S.; Dedden, D.; Schwille, P.; Mizuno, N. Phosphoinositides Regulate Force-Independent Interactions between Talin, Vinculin, and Actin. *eLife* **2020**, *9*, e56110.

[43] Yao, M.; Goult, B. T.; Chen, H.; Cong, P.; Sheetz, M. P.; Yan, J. Mechanical Activation of Vinculin Binding to Talin Locks Talin in an Unfolded Conformation. *Scientific Reports* **2014**, *4*, 4610.

[44] Izard, T.; Evans, G.; Borgon, R. A.; Rush, C. L.; Bricogne, G.; Bois, P. R. J. Vinculin Activation by Talin through Helical Bundle Conversion. *Nature* **2004**, *427*, 171–175.

[45] Chen, H.; Choudhury, D. M.; Craig, S. W. Coincidence of Actin Filaments and Talin Is Required to Activate Vinculin. *The Journal of Biological Chemistry* **2006**, *281*, 40389–40398.

[46] Golji, J.; Lam, J.; Mofrad, M. R. K. Vinculin Activation Is Necessary for Complete Talin Binding. *Biophysical Journal* **2011**, *100*, 332–340.

[47] Bois, P. R. J.; O'Hara, B. P.; Nietlispach, D.; Kirkpatrick, J.; Izard, T. The Vinculin Binding Sites of Talin and α-Actinin Are Sufficient to Activate Vinculin *. *Journal of Biological Chemistry* **2006**, *281*, 7228–7236.

[48] Braga, V. The Crossroads between Cell–Cell Adhesion and Motility. *Nature Cell Biology* **2000**, *2*, E182–E183.

[49] Ridley, A. J. Life at the Leading Edge. *Cell* **2011**, *145*, 1012–1022.

[50] Lo, C. M.; Wang, H. B.; Dembo, M.; Wang, Y. L. Cell Movement Is Guided by the Rigidity of the Substrate. *Biophysical Journal* **2000**, *79*, 144–152.

[51] Plotnikov, S. V.; Pasapera, A. M.; Waterman, C. M. Force Fluctuations within Focal Adhesions Mediate ECM-Rigidity Sensing to Guide Directed Cell Migration. *Cell* **2012**, *151*, 1513–1527.

[52] Wozniak, M. A.; Chen, C. S. Mechanotransduction in Development: A Growing Role for Contractility. *Nature Reviews Molecular Cell Biology* **2009**, *10*, 34–43.

[53] Engler, A. J.; Sen, S.; Sweeney, H. L.; Discher, D. E. Matrix Elasticity Directs Stem Cell Lineage Specification. *Cell* **2006**, *126*, 677–689.

[54] Holle, A. W.; Tang, X.; Vijayraghavan, D.; Vincent, L. G.; Fuhrmann, A.; Choi, Y. S.; del Álamo, J. C.; Engler, A. J. In Situ Mechanotransduction via Vinculin Regulates Stem Cell Differentiation. *Stem cells (Dayton, Ohio)* **2013**, *31*, 10.1002/stem.1490.

[55] Goksoy, E.; Ma, Y.-Q.; Wang, X.; Kong, X.; Perera, D.; Plow, E. F.; Qin, J. Structural Basis for the Autoinhibition of Talin in Regulating Integrin Activation. *Molecular cell* **2008**, *31*, 124–133.

[56] Dedden, D.; Schumacher, S.; Kelley, C. F.; Zacharias, M.; Biertümpfel, C.; Fässler, R.; Mizuno, N. The Architecture of Talin1 Reveals an Autoinhibition Mechanism. *Cell* **2019**, *179*, 120–131.e13.

[57] Chinthalapudi, K.; Rangarajan, E. S.; Izard, T. The Interaction of Talin with the Cell Membrane Is Essential for Integrin Activation and Focal Adhesion Formation. *Proceedings of the National Academy of Sciences* **2018**, *115*, 10339–10344.

[58] Gingras, A. R.; Ziegler, W. H.; Frank, R.; Barsukov, I. L.; Roberts, G. C. K.; Critchley, D. R.; Emsley, J. Mapping and Consensus Sequence Identification for Multiple Vinculin Binding Sites within the Talin Rod *. *Journal of Biological Chemistry* **2005**, *280*, 37217–37224.

[59] Tapia-Rojo, R.; Alonso-Caballero, A.; Fernandez, J. M. Direct Observation of a Coil-to-Helix Contraction Triggered by Vinculin Binding to Talin. *Science Advances* **2020**, *6*, eaaz4707.

[60] Alder, B. J.; Wainwright, T. E. Studies in Molecular Dynamics. I. General Method. *The Journal of Chemical Physics* **1959**, *31*, 459–466.

[61] Rahman, A. Correlations in the Motion of Atoms in Liquid Argon. *Physical Review* **1964**, *136*, A405–A411.

[62] Lindorff-Larsen, K.; Piana, S.; Palmo, K.; Maragakis, P.; Klepeis, J. L.; Dror, R. O.; Shaw, D. E. Improved Side-Chain Torsion Potentials for the Amber ff99SB Protein Force Field. *Proteins* **2010**, *78*, 1950–1958.

[63] Best, R. B.; Zhu, X.; Shim, J.; Lopes, P. E. M.; Mittal, J.; Feig, M.; MacKerell, A. D. Optimization of the Additive CHARMM All-Atom Protein Force Field Targeting Improved Sampling of the Backbone ϕ, ψ and Side-Chain $X1$ and $X2$ Dihedral Angles. *Journal of Chemical Theory and Computation* **2012**, *8*, 3257–3273.

[64] Franz, Florian, The Stability of Lipid Bilayers upon Mechanical Indentation. Master Thesis, University of Heidelberg, 2017.

[65] Verlet, L. Computer "Experiments" on Classical Fluids. I. Thermodynamical Properties of Lennard-Jones Molecules. *Physical Review* **1967**, *159*, 98–103.

[66] Hess, B.; Bekker, H.; Berendsen, H. J. C.; Fraaije, J. G. E. M. LINCS: A Linear Constraint Solver for Molecular Simulations. *Journal of Computational Chemistry* **1997**, *18*, 1463–1472.

[67] Ryckaert, J.-P.; Ciccotti, G.; Berendsen, H. J. C. Numerical Integration of the Cartesian Equations of Motion of a System with Constraints: Molecular Dynamics of n-Alkanes. *Journal of Computational Physics* **1977**, *23*, 327–341.

[68] Clausius, R. XVI. On a Mechanical Theorem Applicable to Heat. *The London, Edinburgh, and Dublin Philosophical Magazine and Journal of Science* **1870**, *40*, 122–127.

[69] Berendsen, H. J. C.; Postma, J. P. M.; van Gunsteren, W. F.; DiNola, A.; Haak, J. R. Molecular Dynamics with Coupling to an External Bath. *The Journal of Chemical Physics* **1984**, *81*, 3684–3690.

[70] Parrinello, M.; Rahman, A. Polymorphic Transitions in Single Crystals: A New Molecular Dynamics Method. *Journal of Applied Physics* **1981**, *52*, 7182–7190.

[71] Harvey, S. C.; Tan, R. K.-Z.; Cheatham, T. E. The Flying Ice Cube: Velocity Rescaling in Molecular Dynamics Leads to Violation of Energy Equipartition. *Journal of Computational Chemistry* **1998**, *19*, 726–740.

[72] Bussi, G.; Donadio, D.; Parrinello, M. Canonical Sampling through Velocity Rescaling. *The Journal of Chemical Physics* **2007**, *126*, 014101.

[73] Franz, F.; Daday, C.; Gräter, F. Advances in Molecular Simulations of Protein Mechanical Properties and Function. *Current Opinion in Structural Biology* **2020**, *61*, 132–138.

[74] Bauer, M. S.; Baumann, F.; Daday, C.; Redondo, P.; Durner, E.; Jobst, M. A.; Milles, L. F.; Mercadante, D.; Pippig, D. A.; Gaub, H. E.; Gräter, F.; Lietha, D. Structural and Mechanistic Insights into Mechanoactivation of Focal Adhesion Kinase. *Proceedings of the National Academy of Sciences* **2019**, *116*, 6766–6774.

[75] Arrhenius, S. Über Die Reaktionsgeschwindigkeit Bei Der Inversion von Rohrzucker Durch Säuren. *Zeitschrift für Physikalische Chemie* **1889**,

[76] Evans, M. G.; Polanyi, M. Some Applications of the Transition State Method to the Calculation of Reaction Velocities, Especially in Solution. *Transactions of the Faraday Society* **1935**, *31*, 875–894.

[77] Kästner, J. Umbrella Sampling. *WIREs Computational Molecular Science* **2011**, *1*, 932–942.

[78] Torrie, G. M.; Valleau, J. P. Monte Carlo Free Energy Estimates Using Non-Boltzmann Sampling: Application to the Sub-Critical Lennard-Jones Fluid. *Chemical Physics Letters* **1974**, *28*, 578–581.

[79] Torrie, G. M.; Valleau, J. P. Nonphysical Sampling Distributions in Monte Carlo Free-Energy Estimation: Umbrella Sampling. *Journal of Computational Physics* **1977**, *23*, 187–199.

[80] Kumar, S.; Rosenberg, J. M.; Bouzida, D.; Swendsen, R. H.; Kollman, P. A. THE Weighted Histogram Analysis Method for Free-Energy Calculations on Biomolecules. I. The Method. *Journal of Computational Chemistry* **1992**, *13*, 1011–1021.

[81] Souaille, M.; Roux, B. Extension to the Weighted Histogram Analysis Method: Combining Umbrella Sampling with Free Energy Calculations. *Computer Physics Communications* **2001**, *135*, 40–57.

[82] Rico, F.; Russek, A.; González, L.; Grubmüller, H.; Scheuring, S. Heterogeneous and Rate-Dependent Streptavidin-Biotin Unbinding Revealed by High-Speed Force Spectroscopy and Atomistic Simulations. *Proceedings of the National Academy of Sciences* **2019**, *116*, 6594–6601.

[83] Goktas, M.; Luo, C.; Sullan, R. M. A.; Bergues-Pupo, A. E.; Lipowsky, R.; Verde, A. V.; Blank, K. G. Molecular Mechanics of Coiled Coils Loaded in the Shear Geometry. *Chemical Science* **2018**, *9*, 4610–4621.

[84] Sheridan, S.; Gräter, F.; Daday, C. How Fast Is Too Fast in Force-Probe Molecular Dynamics Simulations? *The Journal of Physical Chemistry B* **2019**, *123*, 3658–3664.

[85] Litvinov, R. I.; Kononova, O.; Zhmurov, A.; Marx, K. A.; Barsegov, V.; Thirumalai, D.; Weisel, J. W. Regulatory Element in Fibrin Triggers Tension-Activated Transition from Catch to Slip Bonds. *Proceedings of the National Academy of Sciences* **2018**, *115*, 8575–8580.

[86] Barrick, S.; Li, J.; Kong, X.; Ray, A.; Tajkhorshid, E.; Leckband, D. Salt Bridges Gate α-Catenin Activation at Intercellular Junctions. *Molecular Biology of the Cell* **2018**, *29*, 111–122.

[87] Jahed, Z.; Hao, H.; Thakkar, V.; Vu, U. T.; Valdez, V. A.; Rathish, A.; Tolentino, C.; Kim, S. C. J.; Fadavi, D.; Starr, D. A.; Mofrad, M. R. K. Role of KASH Domain Lengths in the Regulation of LINC Complexes. *Molecular Biology of the Cell* **2019**, *30*, 2076–2086.

[88] De-la-Torre, P.; Choudhary, D.; Araya-Secchi, R.; Narui, Y.; Sotomayor, M. A Mechanically Weak Extracellular Membrane-Adjacent Domain Induces Dimerization of Protocadherin-15. *Biophysical Journal* **2018**, *115*, 2368–2385.

[89] Araya-Secchi, R.; Neel, B. L.; Sotomayor, M. An Elastic Element in the Protocadherin-15 Tip Link of the Inner Ear. *Nature Communications* **2016**, *7*, 13458.

[90] Choudhary, D.; Narui, Y.; Neel, B. L.; Wimalasena, L. N.; Klanseck, C. F.; De-la-Torre, P.; Chen, C.; Araya-Secchi, R.; Tamilselvan, E.; Sotomayor, M. Structural Determinants of Protocadherin-15 Mechanics and Function in Hearing and Balance Perception. *Proceedings of the National Academy of Sciences* **2020**, *117*, 24837–24848.

[91] Ettig, R.; Kepper, N.; Stehr, R.; Wedemann, G.; Rippe, K. Dissecting DNA-Histone Interactions in the Nucleosome by Molecular Dynamics Simulations of DNA Unwrapping. *Biophysical Journal* **2011**, *101*, 1999–2008.

[92] Daday, C.; Kolšek, K.; Gräter, F. The Mechano-Sensing Role of the Unique SH3 Insertion in Plakin Domains Revealed by Molecular Dynamics Simulations. *Scientific Reports* **2017**, *7*, 11669.

[93] Grubmüller, H.; Heymann, B.; Tavan, P. Ligand Binding: Molecular Mechanics Calculation of the Streptavidin-Biotin Rupture Force. *Science* **1996**, *271*, 997–999.

[94] Lu, H.; Isralewitz, B.; Krammer, A.; Vogel, V.; Schulten, K. Unfolding of Titin Immunoglobulin Domains by Steered Molecular Dynamics Simulation. *Biophysical Journal* **1998**, *75*, 662–671.

[95] Lee, E. H.; Hsin, J.; Sotomayor, M.; Comellas, G.; Schulten, K. Discovery through the Computational Microscope. *Structure* **2009**, *17*, 1295–1306.

[96] Perez, A.; Morrone, J. A.; Simmerling, C.; Dill, K. A. Advances in Free-Energy-Based Simulations of Protein Folding and Ligand Binding. *Current Opinion in Structural Biology* **2016**, *36*, 25–31.

[97] Bell, G. I. Models for the Specific Adhesion of Cells to Cells. *Science* **1978**, *200*, 618–627.

[98] Bullerjahn, J. T.; Sturm, S.; Kroy, K. Theory of Rapid Force Spectroscopy. *Nature Communications* **2014**, *5*, 4463.

[99] Dudko, O. K.; Hummer, G.; Szabo, A. Theory, Analysis, and Interpretation of Single-Molecule Force Spectroscopy Experiments. *Proceedings of the National Academy of Sciences* **2008**, *105*, 15755–15760.

[100] Pierse, C. A.; Dudko, O. K. Distinguishing Signatures of Multipathway Conformational Transitions. *Physical Review Letters* **2017**, *118*, 088101.

[101] Heymann, B.; Grubmüller, H. AN02/DNP-Hapten Unbinding Forces Studied by Molecular Dynamics Atomic Force Microscopy Simulations. *Chemical Physics Letters* **1999**, *303*, 1–9.

[102] Popa, I.; Rivas-Pardo, J. A.; Eckels, E. C.; Echelman, D. J.; Badilla, C. L.; Valle-Orero, J.; Fernández, J. M. A HaloTag Anchored Ruler for Week-Long Studies of Protein Dynamics. *Journal of the American Chemical Society* **2016**, *138*, 10546–10553.

[103] Tapia-Rojo, R.; Eckels, E. C.; Fernández, J. M. Ephemeral States in Protein Folding under Force Captured with a Magnetic Tweezers Design. *Proceedings of the National Academy of Sciences* **2019**, *116*, 7873–7878.

[104] Karlqvist, O. *Calculation of the Magnetic Field in the Ferromagnetic Layer of a Magnetic Drum.*; Transactions of the Royal Institute of Technology: Stockholm, 1954.

[105] Ichiye, T.; Karplus, M. Collective Motions in Proteins: A Covariance Analysis of Atomic Fluctuations in Molecular Dynamics and Normal Mode Simulations. *Proteins* **1991**, *11*, 205–217.

[106] Hünenberger, P. H.; Mark, A. E.; van Gunsteren, W. F. Fluctuation and Cross-Correlation Analysis of Protein Motions Observed in Nanosecond Molecular Dynamics Simulations. *Journal of Molecular Biology* **1995**, *252*, 492–503.

[107] Lange, O. F.; Grubmüller, H. Generalized Correlation for Biomolecular Dynamics. *Proteins* **2006**, *62*, 1053–1061.

[108] Cover, T. M.; Thomas, J. A. *Elements of Information Theory*; Wiley, 2006.

[109] Costescu, B. I.; Gräter, F. Time-Resolved Force Distribution Analysis. *BMC Biophysics* **2013**, *6*, 5.

[110] Abraham, M. J.; Murtola, T.; Schulz, R.; Páll, S.; Smith, J. C.; Hess, B.; Lindahl, E. GROMACS: High Performance Molecular Simulations through Multi-Level Parallelism from Laptops to Supercomputers. *SoftwareX* **2015**, *1-2*, 19–25.

[111] Senior, A. W. et al. Improved Protein Structure Prediction Using Potentials from Deep Learning. *Nature* **2020**, *577*, 706–710.

[112] Mercadante, D.; Gräter, F.; Daday, C. CONAN: A Tool to Decode Dynamical Information from Molecular Interaction Maps. *Biophysical Journal* **2018**, *114*, 1267–1273.

[113] Calderwood, D. Talin Controls Integrin Activation. *Biochemical Society Transactions* **2004**, *32*, 434–437.

[114] Gough, R. E.; Goult, B. T. The Tale of Two Talins – Two Isoforms to Fine-Tune Integrin Signalling. *FEBS Letters* **2018**, *592*, 2108–2125.

[115] Giannone, G.; Jiang, G.; Sutton, D. H.; Critchley, D. R.; Sheetz, M. P. Talin1 Is Critical for Force-Dependent Reinforcement of Initial Integrin-Cytoskeleton Bonds but Not Tyrosine Kinase Activation. *The Journal of Cell Biology* **2003**, *163*, 409–419.

[116] Frame, M. C.; Patel, H.; Serrels, B.; Lietha, D.; Eck, M. J. The FERM Domain: Organizing the Structure and Function of FAK. *Nature Reviews Molecular Cell Biology* **2010**, *11*, 802–814.

[117] Hamada, K.; Shimizu, T.; Matsui, T.; Tsukita, S.; Tsukita, S.; Hakoshima, T. Structural Basis of the Membrane-Targeting and Unmasking Mechanisms of the Radixin FERM Domain. *The EMBO Journal* **2000**, *19*, 4449–4462.

[118] Chishti, A. H. et al. The FERM Domain: A Unique Module Involved in the Linkage of Cytoplasmic Proteins to the Membrane. *Trends in Biochemical Sciences* **1998**, *23*, 281–282.

[119] Elliott, P. R.; Goult, B. T.; Kopp, P. M.; Bate, N.; Grossmann, J. G.; Roberts, G. C. K.; Critchley, D. R.; Barsukov, I. L. The Structure of the Talin Head Reveals a Novel Extended Conformation of the FERM Domain. *Structure* **2010**, *18*, 1289–1299.

[120] Anthis, N. J.; Wegener, K. L.; Ye, F.; Kim, C.; Goult, B. T.; Lowe, E. D.; Vakonakis, I.; Bate, N.; Critchley, D. R.; Ginsberg, M. H.; Campbell, I. D. The Structure of an Integrin/Talin Complex Reveals the Basis of inside-out Signal Transduction. *The EMBO Journal* **2009**, *28*, 3623–3632.

[121] Saltel, F.; Mortier, E.; Hytönen, V. P.; Jacquier, M.-C.; Zimmermann, P.; Vogel, V.; Liu, W.; Wehrle-Haller, B. New PI(4,5)P2- and Membrane Proximal Integrin–Binding Motifs in the Talin Head Control *B*3-Integrin Clustering. *Journal of Cell Biology* **2009**, *187*, 715–731.

[122] Goult, B. T.; Bouaouina, M.; Elliott, P. R.; Bate, N.; Patel, B.; Gingras, A. R.; Grossmann, J. G.; Roberts, G. C. K.; Calderwood, D. A.; Critchley, D. R.; Barsukov, I. L. Structure of a Double Ubiquitin-like Domain in the Talin Head: A Role in Integrin Activation. *The EMBO Journal* **2010**, *29*, 1069–1080.

[123] Bromberger, T.; Zhu, L.; Klapproth, S.; Qin, J.; Moser, M. Rap1 and Membrane Lipids Cooperatively Recruit Talin to Trigger Integrin Activation. *Journal of Cell Science* **2019**, *132*.

[124] Song, X.; Yang, J.; Hirbawi, J.; Ye, S.; Perera, H. D.; Goksoy, E.; Dwivedi, P.; Plow, E. F.; Zhang, R.; Qin, J. A Novel Membrane-Dependent on/off Switch Mechanism of Talin FERM Domain at Sites of Cell Adhesion. *Cell Research* **2012**, *22*, 1533–1545.

[125] Martí-Renom, M. A.; Stuart, A. C.; Fiser, A.; Sánchez, R.; Melo, F.; Šali, A. Comparative Protein Structure Modeling of Genes and Genomes. *Annual Review of Biophysics and Biomolecular Structure* **2000**, *29*, 291–325.

[126] Fiser, A.; Do, R. K.; Sali, A. Modeling of Loops in Protein Structures. *Protein Science* **2000**, *9*, 1753–1773.

[127] Webb, B.; Sali, A. Comparative Protein Structure Modeling Using MODELLER. *Current Protocols in Bioinformatics* **2016**, *54*, 5.6.1–5.6.37.

[128] Pettersen, E. F.; Goddard, T. D.; Huang, C. C.; Couch, G. S.; Greenblatt, D. M.; Meng, E. C.; Ferrin, T. E. UCSF Chimera—A Visualization System for Exploratory Research and Analysis. *Journal of Computational Chemistry* **2004**, *25*, 1605–1612.

[129] Jo, S.; Kim, T.; Iyer, V. G.; Im, W. CHARMM-GUI: A Web-Based Graphical User Interface for CHARMM. *Journal of Computational Chemistry* **2008**, *29*, 1859–1865.

[130] Hoover, W. G. Canonical Dynamics: Equilibrium Phase-Space Distributions. *Physical Review A* **1985**, *31*, 1695–1697.

[131] Nosé, S. A Unified Formulation of the Constant Temperature Molecular Dynamics Methods. *The Journal of Chemical Physics* **1984**, *81*, 511–519.

[132] Yang, Y. I.; Shao, Q.; Zhang, J.; Yang, L.; Gao, Y. Q. Enhanced Sampling in Molecular Dynamics. *The Journal of Chemical Physics* **2019**, *151*, 070902.

[133] Ratnikov, B.; Ptak, C.; Han, J.; Shabanowitz, J.; Hunt, D. F.; Ginsberg, M. H. Talin Phosphorylation Sites Mapped by Mass Spectrometry. *Journal of Cell Science* **2005**, *118*, 4921–4923.

[134] Pelaseyed, T.; Viswanatha, R.; Sauvanet, C.; Filter, J. J.; Goldberg, M. L.; Bretscher, A. Ezrin Activation by LOK Phosphorylation Involves a PIP2-Dependent Wedge Mechanism. *eLife* **2017**, *6*, e22759.

[135] Zhang, P.; Azizi, L.; Kukkurainen, S.; Gao, T.; Baikoghli, M.; Jacquier, M.-C.; Sun, Y.; Määttä, J. A. E.; Cheng, R. H.; Wehrle-Haller, B.; Hytönen, V. P.; Wu, J. Crystal Structure of the FERM-Folded Talin Head Reveals the Determinants for Integrin Binding. *Proceedings of the National Academy of Sciences* **2020**, *117*, 32402–32412.

[136] Wang, X.; Ha, T. Defining Single Molecular Forces Required to Activate Integrin and Notch Signaling. *Science* **2013**, *340*, 991–994.

[137] Wang, X.; Sun, J.; Xu, Q.; Chowdhury, F.; Roein-Peikar, M.; Wang, Y.; Ha, T. Integrin Molecular Tension within Motile Focal Adhesions. *Biophysical Journal* **2015**, *109*, 2259–2267.

[138] Liu, J.; Wang, Y.; Goh, W. I.; Goh, H.; Baird, M. A.; Ruehland, S.; Teo, S.; Bate, N.; Critchley, D. R.; Davidson, M. W.; Kanchanawong, P. Talin Determines the Nanoscale Architecture of Focal Adhesions. *Proceedings of the National Academy of Sciences* **2015**, *112*, E4864–E4873.

[139] Rossier, O.; Octeau, V.; Sibarita, J.-B.; Leduc, C.; Tessier, B.; Nair, D.; Gatterdam, V.; Destaing, O.; Albigès-Rizo, C.; Tampé, R.; Cognet, L.; Choquet, D.; Lounis, B.; Giannone, G. Integrins $\beta 1$ and $\beta 3$ Exhibit Distinct Dynamic Nanoscale Organizations inside Focal Adhesions. *Nature Cell Biology* **2012**, *14*, 1057–1067.

[140] Goult, B. T.; Yan, J.; Schwartz, M. A. Talin as a Mechanosensitive Signaling Hub. *The Journal of Cell Biology* **2018**, *217*, 3776–3784.

[141] Yogesha, S. D.; Sharff, A.; Bricogne, G.; Izard, T. Intermolecular versus Intramolecular Interactions of the Vinculin Binding Site 33 of Talin. *Protein Science* **2011**, *20*, 1471–1476.

[142] Sievers, F.; Wilm, A.; Dineen, D.; Gibson, T. J.; Karplus, K.; Li, W.; Lopez, R.; McWilliam, H.; Remmert, M.; Söding, J.; Thompson, J. D.; Higgins, D. G. Fast, Scalable Generation of High-Quality Protein Multiple Sequence Alignments Using Clustal Omega. *Molecular Systems Biology* **2011**, *7*, 539.

[143] Joung, I. S.; Cheatham, T. E. Determination of Alkali and Halide Monovalent Ion Parameters for Use in Explicitly Solvated Biomolecular Simulations. *The Journal of Physical Chemistry B* **2008**, *112*, 9020–9041.

[144] Papagrigoriou, E.; Gingras, A. R.; Barsukov, I. L.; Bate, N.; Fillingham, I. J.; Patel, B.; Frank, R.; Ziegler, W. H.; Roberts, G. C.; Critchley, D. R.; Emsley, J. Activation of a Vinculin-Binding Site in the Talin Rod Involves Rearrangement of a Five-Helix Bundle. *The EMBO Journal* **2004**, *23*, 2942–2951.

[145] Feenstra, K. A.; Hess, B.; Berendsen, H. J. C. Improving Efficiency of Large Time-Scale Molecular Dynamics Simulations of Hydrogen-Rich Systems. *Journal of Computational Chemistry* **1999**, *20*, 786–798.

[146] Kabsch, W.; Sander, C. Dictionary of Protein Secondary Structure: Pattern Recognition of Hydrogen-Bonded and Geometrical Features. *Biopolymers* **1983**, *22*, 2577–2637.

[147] Gingras, A. R.; Vogel, K.-P.; Steinhoff, H.-J.; Ziegler, W. H.; Patel, B.; Emsley, J.; Critchley, D. R.; Roberts, G. C. K.; Barsukov, I. L. Structural and Dynamic Characterization of a Vinculin Binding Site in the Talin Rod. *Biochemistry* **2006**, *45*, 1805–1817.

[148] Wang, Y.; Yao, M.; Baker, K. B.; Gough, R. E.; Le, S.; Goult, B. T.; Yan, J. Force-Dependent Interactions between Talin and Full-Length Vinculin. *bioRxiv* **2021**, 2021.04.26.441533.

[149] Haining, A. W. M.; von Essen, M.; Attwood, S. J.; Hytönen, V. P.; Del Río Hernández, A. All Subdomains of the Talin Rod Are Mechanically Vulnerable and May Contribute To Cellular Mechanosensing. *ACS nano* **2016**, *10*, 6648–6658.

[150] Pasapera, A. M.; Schneider, I. C.; Rericha, E.; Schlaepfer, D. D.; Waterman, C. M. Myosin II Activity Regulates Vinculin Recruitment to Focal Adhesions through FAK-Mediated Paxillin Phosphorylation. *Journal of Cell Biology* **2010**, *188*, 877–890.

[151] Oakes, P. W.; Gardel, M. L. Stressing the Limits of Focal Adhesion Mechanosensitivity. *Current Opinion in Cell Biology* **2014**, *30*, 68–73.

[152] Austen, K.; Ringer, P.; Mehlich, A.; Chrostek-Grashoff, A.; Kluger, C.; Klingner, C.; Sabass, B.; Zent, R.; Rief, M.; Grashoff, C. Extracellular Rigidity Sensing by Talin Isoform–Specific Mechanical Linkages. *Nature Cell Biology* **2015**, *17*, 1597–1606.

[153] Geiger, B. A 130K Protein from Chicken Gizzard: Its Localization at the Termini of Microfilament Bundles in Cultured Chicken Cells. *Cell* **1979**, *18*, 193–205.

[154] Nolz, J. C.; Medeiros, R. B.; Mitchell, J. S.; Zhu, P.; Freedman, B. D.; Shimizu, Y.; Billadeau, D. D. WAVE2 Regulates High-Affinity Integrin Binding by Recruiting Vinculin and Talin to the Immunological Synapse. *Molecular and Cellular Biology* **2007**, *27*, 5986–6000.

[155] Weiss, E. E.; Kroemker, M.; Rüdiger, A.-H.; Jockusch, B. M.; Rüdiger, M. Vinculin Is Part of the Cadherin–Catenin Junctional Complex: Complex Formation between α-Catenin and Vinculin. *Journal of Cell Biology* **1998**, *141*, 755–764.

[156] Seddiki, R.; Narayana, G. H. N. S.; Strale, P.-O.; Balcioglu, H. E.; Peyret, G.; Yao, M.; Le, A. P.; Teck Lim, C.; Yan, J.; Ladoux, B.; Mège, R. M. Force-Dependent Binding of Vinculin to α-Catenin Regulates Cell-Cell Contact Stability and Collective Cell Behavior. *Molecular Biology of the Cell* **2018**, *29*, 380–388.

[157] Goldmann, W. H.; Auernheimer, V.; Thievessen, I.; Fabry, B. Vinculin, Cell Mechanics and Tumour Cell Invasion. *Cell Biology International* **2013**, *37*, 397–405.

[158] Cohen, D. M.; Chen, H.; Johnson, R. P.; Choudhury, B.; Craig, S. W. Two Distinct Head-Tail Interfaces Cooperate to Suppress Activation of Vinculin by Talin *. *Journal of Biological Chemistry* **2005**, *280*, 17109–17117.

[159] Jorgensen, W. L.; Chandrasekhar, J.; Madura, J. D.; Impey, R. W.; Klein, M. L. Comparison of Simple Potential Functions for Simulating Liquid Water. *The Journal of Chemical Physics* **1983**, *79*, 926–935.

[160] Borgon, R. A.; Vonrhein, C.; Bricogne, G.; Bois, P. R. J.; Izard, T. Crystal Structure of Human Vinculin. *Structure* **2004**, *12*, 1189–1197.

[161] Golji, J.; Mofrad, M. R. K. A Molecular Dynamics Investigation of Vinculin Activation. *Biophysical Journal* **2010**, *99*, 1073–1081.

[162] Erijman, A.; Dantes, A.; Bernheim, R.; Shifman, J. M.; Peleg, Y. Transfer-PCR (TPCR): A Highway for DNA Cloning and Protein Engineering. *Journal of Structural Biology* **2011**, *175*, 171–177.

[163] Boujemaa-Paterski, R.; Martins, B.; Eibauer, M.; Beales, C. T.; Geiger, B.; Medalia, O. Talin-Activated Vinculin Interacts with Branched Actin Networks to Initiate Bundles. *eLife* **2020**, *9*, e53990.

[164] Kim, L. Y.; Thompson, P. M.; Lee, H. T.; Pershad, M.; Campbell, S. L.; Alushin, G. M. The Structural Basis of Actin Organization by Vinculin and Metavinculin. *Journal of Molecular Biology* **2016**, *428*, 10–25.

[165] Kossiakoff, A. A. *Methods in Enzymology*; Enzyme Structure Part L; Academic Press, 1986; Vol. 131; pp 433–447.

[166] Fujisaki, H.; Moritsugu, K.; Matsunaga, Y. Exploring Configuration Space and Path Space of Biomolecules Using Enhanced Sampling Techniques—Searching for Mechanism and Kinetics of Biomolecular Functions. *International Journal of Molecular Sciences* **2018**, *19*, 3177.

[167] Omachi, T.; Ichikawa, T.; Kimura, Y.; Ueda, K.; Kioka, N. Vinculin Association with Actin Cytoskeleton Is Necessary for Stiffness-Dependent Regulation of Vinculin Behavior. *PLoS ONE* **2017**, *12*, e0175324.

[168] Chorev, D. S.; Volberg, T.; Livne, A.; Eisenstein, M.; Martins, B.; Kam, Z.; Jockusch, B. M.; Medalia, O.; Sharon, M.; Geiger, B. Conformational States during Vinculin Unlocking Differentially Regulate Focal Adhesion Properties. *Scientific Reports* **2018**, *8*, 2693.

[169] Tojkander, S.; Gateva, G.; Lappalainen, P. Actin Stress Fibers–Assembly, Dynamics and Biological Roles. *Journal of Cell Science* **2012**, *125*, 1855–1864.

[170] Souza, P. C. T. et al. Martini 3: A General Purpose Force Field for Coarse-Grained Molecular Dynamics. *Nature Methods* **2021**, *18*, 382–388.

[171] Jung, J.; Nishima, W.; Daniels, M.; Bascom, G.; Kobayashi, C.; Adedoyin, A.; Wall, M.; Lappala, A.; Phillips, D.; Fischer, W.; Tung, C.-S.; Schlick, T.; Sugita, Y.; Sanbonmatsu, K. Y. Scaling Molecular Dynamics beyond 100,000 Processor Cores for Large-Scale Biophysical Simulations. *Journal of Computational Chemistry* **2019**, *40*, 1919–1930.

[172] Jung, J.; Kobayashi, C.; Kasahara, K.; Tan, C.; Kuroda, A.; Minami, K.; Ishiduki, S.; Nishiki, T.; Inoue, H.; Ishikawa, Y.; Feig, M.; Sugita, Y. New Parallel Computing Algorithm of Molecular Dynamics for Extremely Huge Scale Biological Systems. *Journal of Computational Chemistry* **2021**, *42*, 231–241.